A New Determination of the Charged Pion Mass and Muon Neutrino Mass Upper Limit from Exotic Atom X-ray Spectroscopy

Thesis submitted for the degree of
Doctor of Philosophy
at the University of Leicester

by

Nicholas Nelms BSc (Salford)
Department of Physics and Astronomy
University of Leicester

October 2002

ProQuest LLC
789 East Eisenhower Parkway
P.O. Box 1346
Ann Arbor, MI 48106-1346

Declaration

I hereby declare that no part of this thesis has been previously submitted to this or any other University as part of the requirements for a higher degree. Work described here was conducted by the undersigned except for the contribution of colleagues as indicated in the text.

Nicholas Nelms

October 2002

Dedication

This thesis is dedicated to my wife, Frances, our daughters Ruby and Josephine and to Mum and Dad. Without your support and encouragement this work would never have been completed. Just saying thanks does not do justice to my appreciation but anyway, thanks to all of you.

Acknowledgements

There are three people without whom this work would not have been possible and I extend my thanks to them. Firstly, my supervisor Alan Wells who gave me the chance to take on this project in the first place and has supported me all the way through. Secondly, Detlev Gotta whose patience and assistance have been unstinting throughout the whole duration of the project. (Thanks also for all the beers and I look forward to many more). Thirdly, Leopold Simons whose advice and help has been invaluable and always available.

Any work such as this depends upon a number of people working together with a common aim. I consider myself very fortunate to have worked in a small, international collaboration of friends. Thank you to all of you and thanks especially to Maik Hennebach, Bruno Leoni, Dimitris Anagnostopoulos, Paul Indelicato, and Oleg Ayranov for all your help.

Support from friends and colleagues in the Space Research Centre has, and still is unsurpassed. Thanks to Derek for discussions over several thousand cups of coffee, to Johnnie for all the cables and even more cups of tea, to Adam and Ian for your much appreciated time and support during the beam run, to Andrew for oodles of CCD advice, to Nigel for explaining the obscurities of Excel, to Dave for all those runner beans and to Gillian for suffering a proof-reading. Thanks to Chris C for his help in the early stages of this work. Thanks to everybody in the SRC for your friendship.

I also take this opportunity to acknowledge the support of PPARC towards the costs of the CCD camera and for funding my travel.

Publications list

The following publications contain work that has been done as part of this thesis.

1. Nelms, N., Anagnostopoulos, D.F., Ayranov, O., Borchert, G., Egger, J-P., Gotta, D., Hennebach, M., Indelicato, P., Leoni, B., Liu, Y.W., Manil, B., Simons, L.M., Wells, A., "A large area CCD X-ray detector for exotic atom spectroscopy", Nucl. Inst. Meth. **A484**, 419, 2002.

2. Nelms, N. Anagnostopoulos, D., Augsburger, M., Borchert, G., Chatellard, D., Daum, M., Egger, J-P., Gotta, D., Hauser, P., Indelicato, P., Jeannet, E., Kirch, K., Schult, O.W.B., Siems, T., Simons, L.M., Wells, A., "Precision determination of the charged pion mass using X-ray CCD spectroscopy", Nucl. Inst. Meth. **A477**, 461, 2002.

3. Anagnostopoulos, D.F., Augsburger, M., Borchert, G., Chatellard, D., El-Khoury, P., Egger, J-P., Gorke, H., Gotta, D., Hauser, P., Hennebach, M., Indelicato, P., Kirch, K., Lenz, S., Liu, Y.W., Manil, B., Nelms, N., Siems, Th., Simons, L., "Charged pion mass determination and energy-calibration standards based on pionic X-ray transitions", "The Hydrogen Atom: Precision Physics of Simple Atomic Systems", Springer, 500, 2000.

4. Anagnostopoulos, D., Augsburger, M., Borchert, G., Castelli, C., Chatellard, D., El-Khoury, P., Egger, J-P., Gotta, D., Hauser, P., Indelicato, P., Jeannet, E., Kirch, K., Nelms, N., Schult, O.W.B., Siems, T., Simons, L.M., Wells, A., "Precision determination of the pion mass using X-ray CCD spectroscopy", Proc. SPIE **3443**, 32, 1998.

Abstract

This thesis describes an experiment that has made a new determination of the charged pion mass and from which a new upper limit of the muon neutrino mass has been calculated. The experimental approach uses a high-intensity negative pion beam injected into a cyclotron trap and stopped inside a nitrogen/oxygen mix gas-filled target cell where highly excited pionic and muonic atoms are formed. The energy of photons emitted during de-excitation is directly proportional to the reduced mass of the system, from which the mass of the orbiting particle can be determined. X-ray spectra from pionic nitrogen and muonic oxygen are measured using a high-resolution Bragg crystal spectrometer arranged in Johann geometry. A new large area detector comprising six, high quantum efficiency charge coupled devices is positioned at the focus to measure the reflections from the spectrometer. By using muonic oxygen X-rays as calibration for the pionic nitrogen line the negative pion mass has been determined as 139.57176 $\pm$ 0.000259 MeV/c^2, a precision of 1.85 ppm. Although more precise, this value is approximately 11 ppm higher than the current world average. Consequently, the muon neutrino mass upper limit has been calculated as 0.33 MeV/c^2 (90% confidence level) which offers no new information over the current value of 0.17 MeV/c^2. Investigations are underway to determine the validity of the 11 ppm discrepancy.

1 Introduction

1.1 A new determination of the charged pion mass

X-ray spectroscopy of exotic atoms, especially pionic and muonic atoms, has been used for more than thirty years in the investigation of particle properties. However, in the last decade a new generation of high-resolution experiments has become possible, for a number of reasons. These include the following:

i) higher intensity pion beams.

ii) The development of a cyclotron trap, which increases the stop density by two orders of magnitude for pions, that allows the use of low-pressure gas targets.

iii) The evolution of curved crystal spectrometers to use crystals with an area of ~100 cm^2.

iv) The use of CCD detectors to provide high detection efficiencies and good spatial resolution together with excellent background rejection capabilities.

This thesis deals with an experiment from this category to make a new, more precise determination of the charged pion mass.

An improved measurement of the pion mass offers a number of benefits, besides the obvious determination of the mass of the particle itself. These are:

i) an improved determination of the upper limit of the muon neutrino mass by combining the pion mass value with the muon mass value and the muon momentum from pion decay. Although much lower qualitative values are coming from the neutrino oscillation experiments this method still provides the firmest quantitative value.

ii) Pion-nucleon scattering length experiments using pionic hydrogen have a systematic error contribution of ~25% due to the uncertainty in the pion mass value. An improvement in knowledge of the pion mass would allow a significant reduction in systematic errors.

iii) Improved knowledge of the transition energies of completely ionised pionic atoms will allow them to be used as narrow-width calibration standards for X-ray energies.

1.2 Experimental method

The experimental apparatus is shown in figure 7-1 and comprises the cyclotron trap, a curved crystal spectrometer and the CCD detector array. Pions are extracted from a low

momentum pion beam and injected into a cyclotron trap with a high magnetic field, where they are slowed and travel in a spiral path into a gas filled target cell at the centre. Inside the target cell (filled with nitrogen/oxygen in a 90/10% mix at ~1 bar), pionic and muonic atoms form. Both the target chamber and the detector array are positioned on the Rowland circle of the curved crystal spectrometer, which is using Johann geometry. As the exotic atoms de-excite, characteristic X-rays are emitted and the X-rays from the 5-4 transitions of pionic nitrogen and muonic oxygen are focused by the curved crystal onto the CCD detector array. Since the energy of the X-rays is proportional to the reduced mass of the exotic atom system, an accurate measurement of the X-ray energy leads to a value for the mass of the orbiting particle.

In March 2000, the apparatus was assembled in the πE5 area of the 590 MeV proton cyclotron at the Paul Scherrer Institute (PSI) in Switzerland. Over the next nine weeks, a successful beam run resulted in the collection of experimental data from pionic nitrogen and muonic oxygen 5-4 transitions and various calibration sources. The theory behind the experiment, the experimental program and the analysis of the data collected are presented in detail in this thesis, organised as described in the following section.

1.3 Thesis organisation

Chapter 2 introduces the concept of exotic atoms and discusses their formation and de-excitation. Current areas of scientific investigation using exotic atoms and a general method of exotic atom spectroscopy are also presented.

The next three chapters describe the main instrumentation used in high-resolution exotic atom spectroscopy. In chapter 3, crystal diffraction of X-rays and Bragg reflection are discussed, with special attention to the use of curved crystal spectrometers. A detailed description of the Johann spectrometer is followed by its optimisation for exotic atom spectroscopy. Chapters 4 and 5 cover the topic of X-ray CCD detectors in detail. The structure of CCDs and the detection of X-rays are presented in chapter 4. The detailed operation of CCDs is described in chapter 5, along with a discussion of output signal processing and noise reduction. The laboratory evaluation of the CCD22 device, the CCD used for experimental work in this thesis, completes this chapter.

Chapter 6 is dedicated almost exclusively to the pion, the main subject of this thesis. A brief history of its prediction and discovery is followed by methods of pion production. A

detailed review of pion mass measurements up to the present time is given. Finally, muon production and the determination of the muon-neutrino mass are discussed.

The experimental arrangement used to take measurements for the determination of the pion mass is presented in chapter 7. The combination of a cyclotron trap, Johann spectrometer and CCD array is described with the operation of the CCD detector system covered in detail. Optimisation procedures and measurements are described along with their implementation. Results from spectrometer and detector stability measurements taken over the beam run are also presented.

The results from a nine-week beam run using the experimental procedure described in chapter 7 are given in chapter 8. The analysis of the CCD data is undertaken along with a detailed interpretation of the experimental correction factors. The systematic errors are explained and calculated, leading towards the determination of the charged pion mass and an upper limit of the muon neutrino mass. Conclusions are given in chapter 9 along with a discussion of further possible work.

2 Exotic atoms

This chapter introduces the concept of exotic atoms, their formation and subsequent de-excitation. The use of exotic atoms as sensitive tools in different areas of physics is presented along with a discussion of current areas of activity in exotic atom research. Finally, a general method of high resolution X-ray spectroscopy of exotic atoms is described.

2.1 Introduction

Exotic atoms are atoms in which one or more of the orbital electrons has been replaced by an alternative negatively charged particle, typically a pion, muon, kaon or antiproton. The idea of exotic atoms can be traced back to cosmic radiation studies in the late 1930s and 40s [1, 2], culminating in papers describing the capture of negative mesons in matter, i.e. the formation of exotic atoms [3, 4, 5]. Since then the applications of exotic atom physics have been numerous [6] and are still providing methods for fundamental parameter analysis and particle property determination.

2.2 Formation of exotic atoms

The most common method of creating exotic atoms is by stopping a beam of negatively charged particles (such as pions or muons) in either a solid, liquid or gas target. The particle beams are usually obtained at medium energy (0.5 – 10 GeV) proton accelerators. An exotic atom is typically formed in the following stages.

i) The incoming particles slow down from relativistic velocities to the velocity of atomic electrons by losing energy in ionising collisions with target atoms. In terms of energy, this is a reduction from ~100 MeV to ~2 keV. This process typically occurs in 10^{-9} or 10^{-10} s in solid or liquid targets, up to 1000 times longer in gaseous ones [6].

ii) Below 2 keV, the particle velocity is lower than that of the valence electrons of the stopping material and the particle can be considered as moving inside a degenerate electron gas. Further slowing from electron interaction occurs from 2 keV to ~10 eV at which point capture into the Coulomb field of a target atom occurs. This stage takes between 10^{-13} and 10^{-14} s and is well described in [5]. Assuming the decelerated particle lives sufficiently long, the newly formed exotic atom will be in a highly excited state with a principal quantum number of order

$$n = n_e \sqrt{\frac{m}{m_e}}\,, \qquad 2\text{-}1$$

where m is the mass of the incoming particle, n_e is the outmost filled electron shell when capture occurs and m_e is the mass of the electron. During capture of the particle, the electron shell is left in a state of ionisation that depends upon the atomic number of the target atom and the probability of electron shell refilling. The latter is particularly sensitive to the matter state of the target material, with electron refilling in gases taking much longer than in solids [7].

2.3 Atomic cascade within exotic atoms

De-excitation begins via the Auger process. When Auger ejection of electrons is complete the X-ray transitions dominate and the captured particle rapidly moves to the $(l = n - 1)$ orbits because this method of de-excitation prefers the largest Δn possible. From here, fulfilling the selection rules $\Delta l = \pm 1$ and $\Delta m = 0, \pm 1$, only circular transitions $(n, l = n - 1) \rightarrow (n - 1, l = n - 2)$ can be made [8]. Figure 2-1 shows the level scheme for a muonic atom [6].

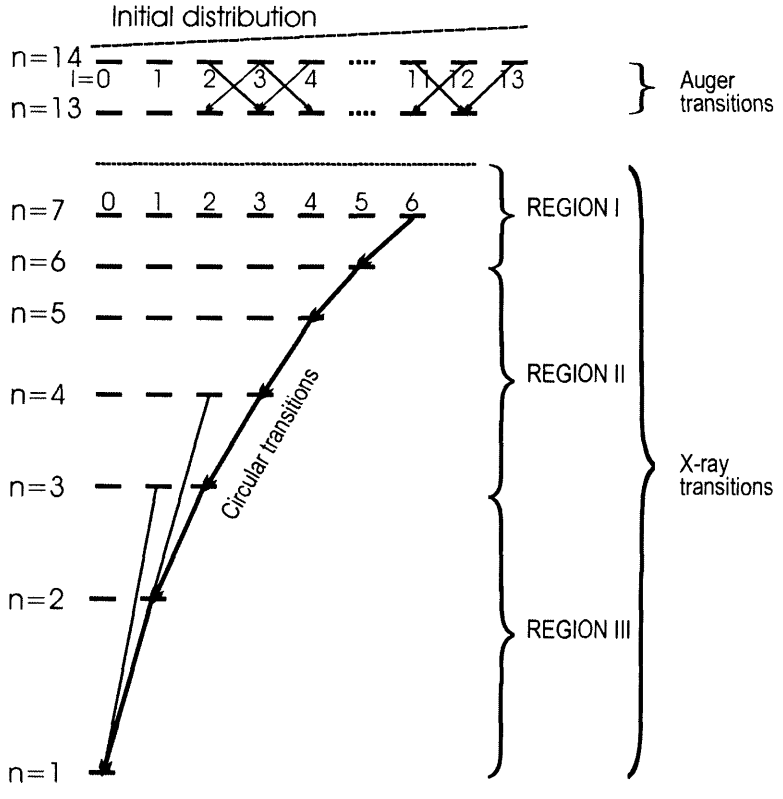

Figure 2-1. Principal level scheme of a muonic atom [6], showing the regions where different effects occur during de-excitation.

In Region I, the upper level of the X-ray transition region, the electronic shell influences the energy levels if any atomic electrons remain or the orbits have been refilled. Nuclear effects dominate region III, where the particle wave function begins to overlap with that of the nucleus. For this thesis, Region II is the most important where the energy levels are influenced by neither the electron shell nor the nucleus and determination of the properties of the captured particle become possible. As mentioned previously, electron re-filling is dependent upon the matter state of the target and exotic atoms formed in low-pressure gas targets reach a high or even complete state of ionisation during de-excitation. When a muonic atom reaches the ground state, the muon either undergoes nuclear capture (since its wave function now overlaps greatly with the nuclear wave function) or it may decay by electron emission (weak interaction). In hadronic atoms, strong interaction effects ensure that nuclear capture occurs. Consequently, the muon lifetime is between 70 ns and 2 μs depending upon the atomic number of the nucleus. The level scheme for hadronic atoms is similar to that for muonic atoms except for when the particle reaches Region III or the inner angular momentum states (l = 0, 1) and pion absorption will occur. This part of the scheme differs greatly due to strong interaction effects between the particle and the nucleons. Nuclear capture for low Z atoms mainly occurs from the s-levels, causing a shifting and broadening of these states. Hence, for hadrons the lifetime is given by the duration of the atomic cascade and is of order 10^{-12} s.

2.4 Exotic atom science

The observable quantities in exotic atom experiments are typically the energies and intensities of X-rays emitted during de-excitation. If properly understood, exotic atoms provide sensitive, precision tools for a number of fundamental tests and determination of particle properties. A search of the World Wide Web reveals numerous annual conferences with one or more sessions dedicated to exotic atoms, a topical indicator that they still play a significant role in modern physics. However, as a precursor to exploiting exotic atoms, observation of the early stages of de-excitation provides invaluable information about the formation of the exotic atom and ionisation status of the electron shell. Accurate models of the electromagnetic cascade [9, 10] are essential in experiments where it is necessary to know the level of electron screening in an exotic atom. In particular, low-pressure gas targets ($Z<18$) are now often used, where complete ionisation has been established for pionic and muonic atoms [11, 12]. The following sections summarise some of the current research in the field. The list is by no means exhaustive but demonstrates the main areas of activity.

2.4.1 Quantum electrodynamics

Ever since quantum electrodynamic theory, or QED, was first developed, experimentalists have been devising new ways to test its predictions. Exotic atoms have played a significant part in this testing and still do so today. In electronic atoms, QED effects are very small and tests in electronic hydrogen-like ions have provided Lamb shift values to a precision of no better than a few percent. Exotic atoms however, formed with particles much heavier than the electron, provide a unique opportunity to study the complementary contributions to the shift [13]. In particular, vacuum polarisation (typically a small contribution to the Lamb shift in electronic atoms) is readily accessible via muonic and pionic atoms with a level of 900 ppm being achieved [14]. Even now, a new experiment has been suggested which could provide a determination of the vacuum polarisation in these exotic atoms with another order of magnitude increase in precision [15]. Similarly, an experiment currently in progress [16] is making use of muonic hydrogen to determine the proton charge radius to the level of 1 part in 10^3.

2.4.2 Particle physics

The energy levels of an exotic atom are very sensitive to the properties of the captured particle. Consequently, exotic atoms can be used for making precise measurements of certain aspects of such a particle and system. These include the following:

i) particle mass

The reduced mass of the exotic atom system is proportional to the energy of the X-rays emitted during de-excitation as given by

$$E = m_r F\left(n, l, j\right) \qquad 2\text{-}2$$

where m_r is the reduced mass of the particle-nucleus system, F represents the Dirac equation for muonic atoms or the Klein-Gordon equation for hadronic atoms, n is the principal quantum number, l is the angular momentum quantum number and j is the total angular momentum quantum number. Particles with their most precise mass value determined by exotic atom X-ray measurement are the pion (π-), kaon (K-) and sigma (Σ-). The antiproton was also on this list until fairly recently but owing to its stability is now more precisely measured using the Penning-trap method [17].

ii) Strong interaction shift

Several programs to measure the strong interaction shift in exotic atoms are underway. These include experiments using pionic hydrogen [18] and kaonic hydrogen [19] atoms. Pion- and kaon-nucleon scattering lengths can be determined from the measurement of the strong interaction shift and width of pionic hydrogen in the ground state. A measurement of both properties to the 1% level is enough to provide a test of the methods of chiral perturbation theory and allows determination of the pion-nucleon coupling constant.

2.4.3 X-ray calibration standards

Energy calibration and response function measurements of crystal spectrometers is a particular problem in the few keV region. Lines available by fluorescence from X-ray tubes have natural line widths that exceed the typical resolution of a spectrometer by factors of 3 or 4. Also, they tend to have complex line shapes due to satellite transitions from multiple ionisations. This problem can sometimes be resolved by the use of narrow transitions from completely ionised exotic atoms. Pionic atoms are the most promising, since they tend to have the highest count rates making practical measurement possible. This method has already been successfully demonstrated where the π^{14}N(5g-4f) transition has been used to determine the value of the Sc Kα_1 transition to one order of magnitude more accurately than that in the published tables [20].

2.5 High resolution X-ray spectroscopy of exotic atoms

The formation of exotic atoms is inevitable whenever negatively charged particles are stopped in matter. However, the state of the matter in which the exotic atoms are formed is of great importance when it comes to interpreting the characteristic X-rays emitted during their de-excitation. If solid or liquid matter is used then electron re-filling of the ionised shell typically occurs within the lifetime of the exotic atom. This leads to ambiguity in the level of electron screening and consequently a broadening in the transition energy.

Use of low-pressure gas targets avoids this problem but introduces more difficulties. The stop-rate in a gas is severely reduced compared to that in a solid target and so either the X-ray production rate is restrictively low or the target volume is impossibly large.

A relatively new technique can be used, which employs a cyclotron trap to essentially 'wind up' the long stopping distance normally required. This method is described in detail in chapter 6.

Once an acceptable level of X-ray production is achieved, a high energy-resolution method of spectroscopy is required. In the few keV range this has to be performed with a Bragg crystal spectrometer.

3 X-ray crystal spectroscopy

This chapter describes the use of crystals for the diffraction of X-rays and the application of the Bragg law. Crystal properties in relation to X-ray diffraction are discussed. The concept of a curved crystal spectrometer is introduced and Johann geometry is described in detail. Finally, optimisation of a Johann spectrometer for exotic atom spectroscopy is covered.

3.1 Introduction

The diffraction of X-rays by crystals was discovered by von Laue and his collaborators in 1912 [21]. This discovery resulted in the development of two complementary areas of research, the study of crystal structure using X-rays and the means of studying X-ray spectra to high precision using crystals. An estimation of the wavelength of X-rays already existed and von Laue calculated that the atomic spacing in a solid was of a comparable dimension. Von Laue considered that a crystal may act like a diffraction grating and consequently, he and his collaborators tried passing a narrow beam of X-rays through a crystal of zinc blende. They produced a, now well-known, pattern of diffraction spots on a photographic plate. This pattern was exactly what would be expected from a three-dimensional grating.

It was Bragg [22] who offered a simple interpretation of the diffraction patterns produced by von Laue. He suggested that each of the spots surrounding the central image could be a reflection of the X-ray beam from an internal plane, within the crystal, that contained many atoms. One such plane should be parallel to the cleavage line of a crystal and Bragg tried reflecting an X-ray beam from such a surface of a mica crystal and, using a photographic plate, he recorded a spot at the angle of reflection.

3.2 Bragg reflection

Bragg reflection can be explained by considering the crystal structure as a regular array of identical planes of atoms, separated by a distance d, known as the 'd-spacing'. An X-ray beam incident upon this crystal (figure 3-1) will be scattered by electrons of the regularly spaced atoms in the crystal lattice. From the diagram, we can see that the reflection path length difference between adjacent layers is equal to AB + BC, where AB = BC = $d \sin\theta_B$. Constructive interference from reflections from different planes of atoms will only occur when the path length difference is equal to an integral number of wavelengths of the incident X-ray beam. This is known as Bragg's law and can be stated as

$$n\lambda = 2d \sin\theta_B , \qquad 3\text{-}1$$

where n is the order of diffraction, d is the crystal d-spacing and θ_B is the angle of reflection, or Bragg angle.

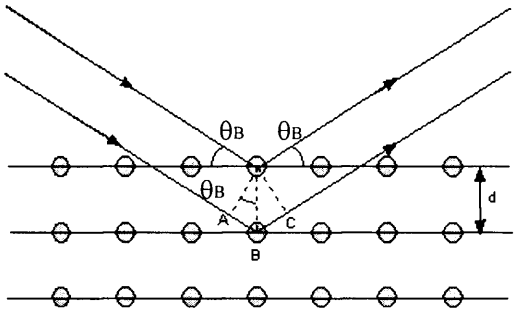

Figure 3-1. Bragg reflection from a crystal.

The crystal d-spacing is temperature dependent and varies from d (in leading order) at known temperature t (typically 18 °C) by [23]

$$d_T = d_{18}\left(1 + \alpha(T - t)\right) , \qquad 3\text{-}2$$

where α is the linear expansion coefficient and T is temperature.

Differentiation of the Bragg Law leads to an equation for the crystal dispersion

$$\frac{d\theta_B}{d\lambda} = \frac{n}{2d\cos\theta_B} . \qquad 3\text{-}3$$

Combining eqs. 3-1 and 3-3, we obtain an expression for change of wavelength with Bragg angle,

$$\frac{d\lambda}{\lambda} = \frac{1}{\tan\theta_B} d\theta_B . \qquad 3\text{-}4$$

If we replace $d\theta_B$ by the intrinsic resolution, ω, of the crystal, we obtain an equation for the crystal resolving power,

$$\frac{\lambda}{d\lambda} = \frac{\tan\theta_B}{\omega} . \qquad 3\text{-}5$$

From eq. 3-4, we can see that at higher Bragg angles the wavelength is less sensitive to variations in Bragg angle.

The Bragg law, as stated in eq. 3-1, is not exact, due to refraction of the X-rays as they enter the crystal. The refractive index is less than 1 [24] and so the X-ray path is bent away from the normal (figure 3-2). This alters the extra distance travelled by X-rays reflected from each 'lower' plane of atoms and consequently changes the necessary path difference for the Bragg condition to occur.

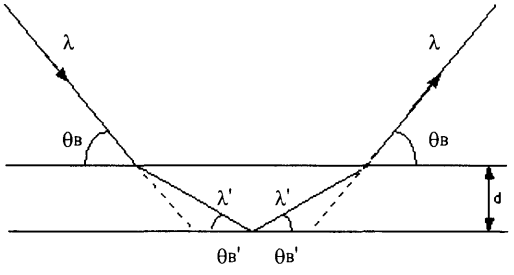

Figure 3-2. Bragg correction due to refraction.

Inside the crystal the X-ray wavelength changes from λ to λ', the angle for Bragg reflection becomes θ_B' and the Bragg law becomes

$$n\lambda' = 2d \sin\theta_B' \ . \qquad 3\text{-}6$$

Neglecting absorption, the unit decrement of index of refraction, δ, is defined by the relation [25]

$$\mu = 1 - \delta = \frac{\lambda}{\lambda'} = \frac{\cos\theta}{\cos\theta'} \ . \qquad 3\text{-}7$$

Eliminating the refractive index, μ and primed variables from eqs. 3-6 and 3-7 (see Appendix A1) leads to

$$n\lambda = 2d \sin\theta_B \left(1 - \frac{2\delta - \delta^2}{\sin^2\theta_B}\right)^{\frac{1}{2}} \ . \qquad 3\text{-}8$$

Since δ is of order 10^{-6}, we can ignore δ^2, expand the bracket and, again ignoring powers of δ higher than 1, we get

$$n\lambda = 2d\sin\theta\left(1-\frac{4d^2}{n^2}\frac{\delta}{\lambda^2}\right), \qquad 3\text{-}9$$

where $\sin^2\theta$ has been substituted by the rearranged Bragg Law. This equation is known as the modified Bragg Law.

The correction factor in brackets (eq. 3-9) varies with order of reflection, becoming less significant as the order increases. The measured (experimental) Bragg angle differs from the uncorrected Bragg angle by an amount $\Delta\theta_{ind}$ and is given by

$$\theta_{\exp} = \theta_B + \Delta\theta_{ind}\ , \qquad 3\text{-}10$$

3.2.1 Intrinsic crystal properties

Using dynamical crystal theory [26], the intrinsic properties of single crystals can be determined to within a few percent. The most significant properties, in terms of the response, are the crystal rocking curve width, ω, the peak reflectivity, P and the integrated reflectivity, R_I. The rocking curve width describes the divergence of a parallel, mono-energetic beam of radiation after Bragg reflection by the crystal. The peak reflectivity represents the maximum reflected intensity in the diffraction profile (as a percentage of a loss less reflection) and takes into account incoherent factors such as photo-absorption. The integrated reflectivity is a measure of the intensity of the reflected radiation and is related to ω and P (for a nominally rectangular diffraction profile) by

$$R_I \approx \frac{4}{3}P\omega \qquad 3\text{-}11$$

where R_I and ω are in radians. From eq. 3-11 we can see that as the resolution increases (ω decreases), the integrated reflectivity, or count rate, decreases. So, for a crystal with infinitely good resolution, there would be zero count rate, as one would expect.

Bragg reflection, when used for energy analysis of X-ray lines, relies upon extreme angular sensitivity and crystals with an intrinsic resolution of $\omega = 10^{-4}$ radians are typical for the

few keV range. For flat crystals with this order of resolution, only a small part of the crystal surface meets the Bragg condition. For a source/detector-crystal distance of, say, 2 m, a region only slightly more than 1 mm wide would provide a usable reflection at any particular wavelength. Subsequently, the reflected X-ray flux can be very low indeed for high-resolution experiments.

3.3 Curved crystal spectrometers

Typical experiments involving exotic atom X-ray spectra require high-resolution measurements from an extended source with very low count rates. This is true even with the advent of high intensity beams produced at 'meson factories'. The low count rate effectively excludes the use of a double-flat crystal monochromator and other spectrometer types requiring an entrance slit. The Johann spectrometer (figure 3-3), however, with a curved focusing crystal, slit-less operation and extended wavelength range is much closer to the ideal.

3.3.1 Johann geometry

A focusing X-ray spectrometer using a curved crystal must meet two requirements. Firstly, specular reflection, for which the detector must lie upon the Rowland circle (an imaginary circle with radius r, tangential to a point on the surface). Secondly, the Bragg reflection condition must be met over the entire surface of the crystal, for suitable wavelength X-rays emitted from a fixed point. This requires the crystal to be bent with a radius of curvature equal to twice that of the Rowland circle. Consequently, it is not possible to meet these two requirements simultaneously except at the point where the Rowland circle and the crystal are tangential. The effect is to produce a geometrical aberration. Because of this broadening, an X-ray focusing spectrometer using a curved crystal was not demonstrated until 1931 [27], by Johann, although the concept had been described some twenty years earlier.

The Johann spectrometer is normally used with a diffuse X-ray source and has the advantage over other types that the full crystal area can be used to simultaneously diffract a range of wavelengths. The crystal is bent to a radius, R_C, (figure 3-3) and positioned tangential to the Rowland circle (radius = $R_C/2$) at the crystal pole. X-rays, of wavelength λ_1, from a source placed on (or near) the Rowland circle, will be reflected according to Bragg's law from the full crystal area and focused to a point on the opposite side of the Rowland circle. Correspondingly, a second wavelength, λ_2, from a different position within the same source, will be focused to a different point. It can be seen that, with this

arrangement, no entrance slit is necessary for the spectrometer but a position sensitive detector is required to measure the dispersed spectrum. The reflection of a single wavelength from the whole crystal surface can provide a large increase in sensitivity (compared with the single line reflection of a flat crystal), necessary when the input flux is low and high resolution is required. The dominant, inherent aberration (Johann broadening) of the spectrometer, which can be thought of as due to the finite horizontal size of the crystal, can be tolerated, as long the line broadening is less than that due to the intrinsic resolution of the crystal. For small crystals or with a large radius of curvature, this is typically the case.

Referring to figure 3-3, we can define a number of relationships inherent to the Johann geometry. The source-crystal (or detector-crystal) distance is given by

$$SC = DC = R_C \sin\theta_B \ , \qquad 3\text{-}12$$

where θ_B is the Bragg angle and R_C is the radius of curvature of the crystal. The source or detector distance to the origin of the Rowland circle, O is given by

$$SO = DO = R_C \cos\theta_B \ , \qquad 3\text{-}13$$

from which we then obtain

$$DS = L = 2R_C \sin\theta_B \cos\theta_B \ , \qquad 3\text{-}14$$

for the distance between the detector and the source.

It must be stated that all expressions in this chapter are calculated on the basis of symmetrically cut crystals, i.e. the reflecting crystal planes are parallel to the surface of the crystal.

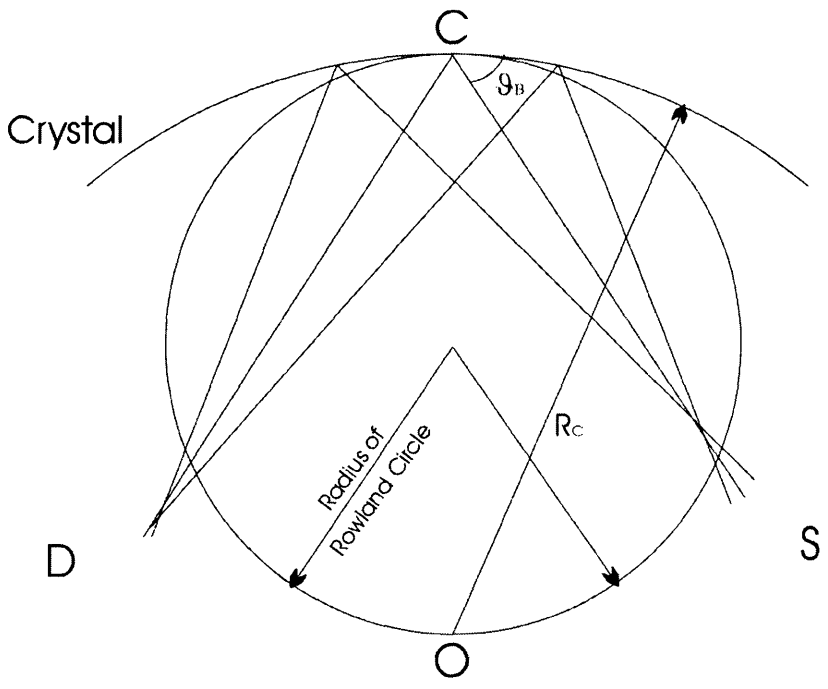

Figure 3-3. Geometry of the Johann spectrometer. S and D indicate the position of source and detector respectively. C is the crystal pole. The crystal has a radius of curvature R_C, which is equal to the diameter of the Rowland circle, about O. The different focal points for reflections from different areas of the crystal are apparent.

3.3.2 Waveband and dispersion

The waveband of a Johann spectrometer is determined by the spatial extent of the (diffuse) X-ray source. The horizontal dimension of the source subtends an angle with the crystal pole, which defines a range of Bragg angles, $\Delta\theta_B$. Substituting this into the dispersion relation defined in eq. 3-3, we obtain an expression for the wavelength range accepted by the spectrometer,

$$n\Delta\lambda = 2d\cos\theta_B\Delta\theta_B \ , \qquad 3\text{-}15$$

centered upon the wavelength defined by the mean Bragg angle and ignoring higher order reflections and refractive index effects.

If we now define the direction of dispersion x, at the (flat) detector, as perpendicular to the direction of DC, then, from figure 3-3 and eq. 3-12, a small change in Bragg angle of $\delta\theta_B$ will give a corresponding change in x of

$$\delta x = R_C \sin\theta_B\delta\theta_B \ . \qquad 3\text{-}16$$

Combining this equation with the dispersion relation of eq. 3-4 we get

$$\frac{dE}{E} = \frac{d\lambda}{\lambda} = \frac{1}{\tan\theta_B R_C \sin\theta_B} dx, \qquad 3\text{-}17$$

where E is the energy of the incident X-ray. This leads immediately to an expression for the dispersion of the crystal,

$$\frac{dx}{dE} = \frac{R_C}{E} \sin\theta_B \tan\theta_B \ . \qquad 3\text{-}18$$

A similar expression can obviously be written for dispersion in terms of wavelength instead of energy.

$$\frac{dx}{d\lambda} = \frac{R_C}{\lambda} \sin\theta_B \tan\theta_B \ . \qquad 3\text{-}19$$

From eq. 3-18, it is obvious that the larger the radius of curvature of the crystal (and consequently, from the Johann geometry, the larger the Rowland circle radius), the greater the dispersion for any particular energy change.

The spectrometer as described by Johann is based upon a cylindrically bent crystal. In this case, the focused line height at the detector is given by

$$h_L = 2h_C + h_S \ , \qquad 3\text{-}20$$

where h_c is the height of the crystal and h_s is the height of the source. For a source diameter of, say 60 mm and a crystal height of 100 mm, the focused image will be 260 mm high. This dimension can put severe demands upon a position sensitive detector in low flux applications, where detection of as many photons as possible is the aim. Fortunately this situation can be improved by combining the vertical focusing of the von Hamos geometry [28] with the horizontal focusing of the Johann geometry, as described by Eggs and Ulmer [29]. It is possible to bend the crystal in the vertical direction such that two dimensional focusing can be achieved but only for a single Bragg angle. In this case, the image of a point source at the detector will be focused to a single point. However, this usually results

in a difficult ellipsoidal curvature and so the vertical radius of curvature, R_V is usually chosen as

$$R_V = R_C = 2r \ , \qquad 3\text{-}21$$

where R_C is the horizontal radius of curvature and r is the Rowland circle radius. This results in a loss of focusing, i.e. the image of a point source is a curved line but of reduced height (compared to the cylindrical geometry of the Johann spectrometer), not a spot. The curvature of the line can be compensated for when post-processing the data from a two-dimensional, position-sensitive detector.

3.3.3 Sensitivity

The sensitivity of a Johann instrument is affected by a number of factors, including the source activity, Bragg crystal reflectivity and detector efficiency. It may be expressed as a count-rate at a particular X-ray energy as follows:

$$n_x = A_x E_x \eta \ , \qquad 3\text{-}22$$

where A_x is the activity of the source, E_x is the detector efficiency and η is the crystal efficiency. It is the quantity η which is of interest here (A_x and E_x are discussed in the chapter upon experimental arrangement) and may be expressed as

$$\eta = \frac{\Delta\Omega}{4\pi}\frac{\Delta S}{S}P \ , \qquad 3\text{-}23$$

where $\Delta\Omega/4\pi$ is the solid angle fraction of the crystal seen from the source, P is the peak reflectivity and $\Delta S/S$ is the fraction of the source area from which X-rays are emitted which meet the Bragg condition for reflection. For sources which are small compared to the Rowland circle radius, the usable fraction of source area for a uniformly radiating disk, is given by

$$\frac{\Delta S}{S} = \frac{\omega R_I \sin\theta_B 2r_S}{\pi r_S^2} = \frac{2R_I \sin\theta_B}{\pi r_S}\omega \ , \qquad 3\text{-}24$$

where R_I is the integrated reflectivity (eq. 3-11), θ_B is the Bragg angle and ω is the rocking curve width of the crystal.

3.3.4 Spectrometer resolution

The resolution of a Johann spectrometer is influenced mainly by the intrinsic rocking curve width of the crystal, ω, and the dimensions of the crystal and the source. If we define the horizontal and vertical angles subtended by the crystal from point O (fig. 3-4) as 2σ and 2ε respectively (σ and ε are equal to $b/2R_c$, where b is the height and width of the crystal and R_c is the radius of curvature of the crystal), then the change in angle caused by the width of the crystal is given by [29]

$$\Delta\theta = \frac{\sigma^2 \cot\theta_B}{2} \quad . \qquad 3\text{-}25$$

The angular change caused by the height of the crystal may be obtained from

$$\Delta\theta_h = \frac{-\cot^3\theta_B \varepsilon^4}{4} \quad , \qquad 3\text{-}26$$

and may be ignored. If z is the vertical dimension of the source, then the opening angle of the source as seen from the crystal, is given by

$$\varsigma = \frac{z}{R_c} \quad , \qquad 3\text{-}27$$

where R_c is the radius of curvature of the crystal. From this, we can obtain an expression for the change in angle caused by the finite extension of the source in the vertical direction,

$$\Delta\theta = \frac{\varsigma^2}{\sin 2\theta_B} \quad . \qquad 3\text{-}28$$

Using the relationships between Bragg angle and local change of wavelength (eqs. 3-4 and 3-5), we can now define expressions for the relative energy resolution introduced by each of the angular variations detailed above. For the intrinsic width of the crystal, we have

$$\frac{\Delta E}{E} = \cot\theta_B \omega \quad . \qquad 3\text{-}29$$

The energy shift due to the width of the crystal is given by

$$\frac{\Delta E}{E} = \frac{\sigma^2 \cot^2 \theta_B}{2} \qquad 3\text{-}30$$

and for the height of the source, by

$$\frac{\Delta E}{E} = \frac{\varsigma^2}{2\sin^2 \theta_B} \,. \qquad 3\text{-}31$$

Avoiding small Bragg angles is obviously preferred, to maintain the minimum degradation in resolution.

3.3.5 Johann broadening

The nature of the Johann spectrometer introduces an asymmetric broadening of the response function due simply to the geometry, with an extended tail towards the shorter wavelength side. This function can be suitably approximated to a right-angled triangle [29]. In the case of a cylindrically bent crystal, the maximum change in Bragg angle (for any particular X-ray) is given by

$$\Delta\theta_J = \frac{1}{2}\left[\frac{\left(\frac{b/2}{R_C}\right)^2}{\tan^2 \theta_B}\right], \qquad 3\text{-}32$$

where b is the crystal width and R_C is the radius of curvature of the crystal.

3.3.6 Crystal lattice deformation

For spectrometers used in Johann geometry (and other curved crystal spectrometers), the curvature of the crystal causes a deformation of the lattice constant, d, increasing the separation towards the rear of the crystal and decreasing it towards the front. The middle layer (defined as the neutral layer) of the crystal will retain the original d spacing. The relative change in the lattice constant is given by [30]

$$\frac{\Delta d}{d} = -\frac{2\nu}{1-\nu}\frac{Z-\delta}{R_C}, \qquad 3\text{-}33$$

where ν is Poisson's number for the crystal material, Z is the extinction length at the energy of interest, δ is the distance from the neutral layer to the surface of the crystal and R_C is the radius of curvature of the crystal.

3.4 Exotic atom spectroscopy using a Johann spectrometer

Experiments involving measurement of X-rays from light exotic atoms are typically characterised by very low count rates, the need for high resolution and operation at X-ray energies in the 1-10 keV range. These factors have to be considered and a compromise reached, since they are not mutually exclusive, when optimising a Johann spectrometer.

The physical size of the crystal should be as large as possible to give the largest solid angle to the source and maximise count rate. Crystal wafers of some materials are now available up to 100 mm diameter. The crystal bend should be limited to the point where the Johann broadening due to the radius of curvature (see eq. 3-33) is not larger than the intrinsic rocking curve width of the crystal. In the few keV range, the choice of crystal is typically limited to silicon, quartz or germanium for high resolution. Germanium has a slightly lower resolution whilst quartz has a lower intensity than silicon. In addition, silicon is more readily available and less expensive. Practical Bragg angles are typically limited to between 30° and 70° due to the physical layout of the spectrometer but from eqs. 3-32 and 3-33 we can see that the angle should be greater than 45° to maintain resolution and again minimise the impact of Johann broadening. Keeping the Bragg angle above 45° is instrumental in the selection of crystal material and the plane of reflection.

3.5 Johansson spectrometer

It is worth mentioning the spectrometer proposed by Johansson [31] (figure 3-4). This has a similar geometry to the Johann spectrometer, with a crystal bent to a radius of curvature, $R = 2r$. However, in the case of the Johansson spectrometer, the crystal surface should be ground to a radius of curvature equal to the radius of the Rowland circle. In this way, the reflecting planes still lie on a cylinder of radius 2r but the crystal surface is tangential to the Rowland circle. This reduces aberrations compared with Johann geometry due to the size of the crystal (section 3.3.2). However, the practical implications of machining such a crystal make this a very difficult instrument to manufacture.

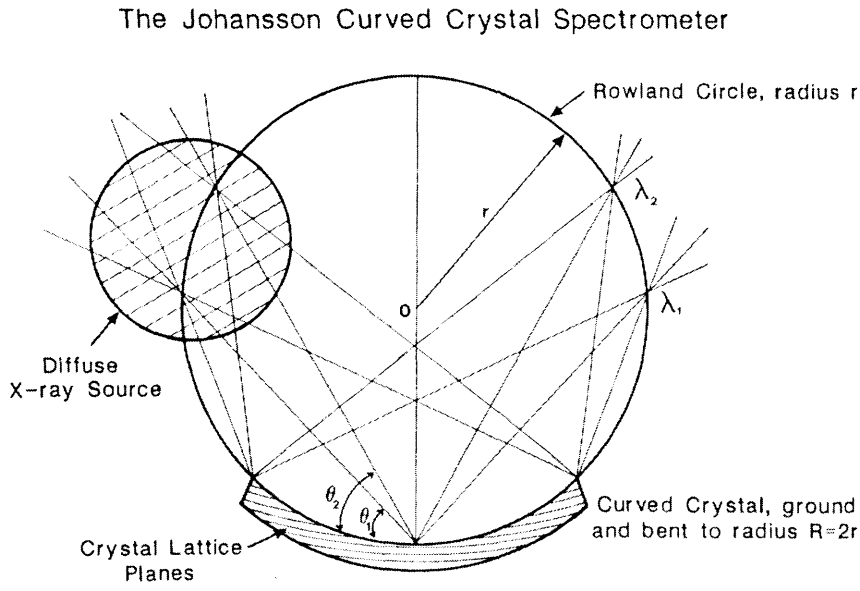

Figure 3-4. Johansson spectrometer (after Dunn [23]).

4 CCD X-ray detectors

This chapter discusses the operation of the charge-coupled device (CCD) and its application as an X-ray detector. Performance of the CCD is discussed in terms of noise sources and detection efficiency. Finally, the construction and performance of the CCD22, designed specifically for X-ray spectroscopy in the 1 to 10 keV range, is described.

4.1 Introduction

The history of CCD development from the first production devices at Bell Laboratories in 1970 [32] has been well documented in many references, including [33, 34]. Although not originally developed as such, their use as imaging detectors was realised very early on [35] and application to X-ray detection soon followed [36]. At the University of Leicester a comprehensive research programme, begun in the early 1980s has investigated the use of CCDs as X-ray detectors [37, 38, 39, 40, 41, 42] for X-ray astronomy missions, resulting in the development of custom devices for the JET-X [43] and XMM-Newton [44] satellite instruments. Devices from the XMM-Newton programme have been used to construct the CCD detector array for use in the experimental measurements described in this thesis.

4.2 CCD design

4.2.1 Introduction

A charge-coupled device is a semiconductor photon detector, usually fabricated from p-type silicon. It comprises an array (either 1- or 2-dimensional) of elements or pixels capable of storing local, photon generated charge. A typical 2-dimensional CCD will have a store section, an image section and a line readout section (figure 4-1), whilst a 1-dimensional device is essentially just a line readout section.

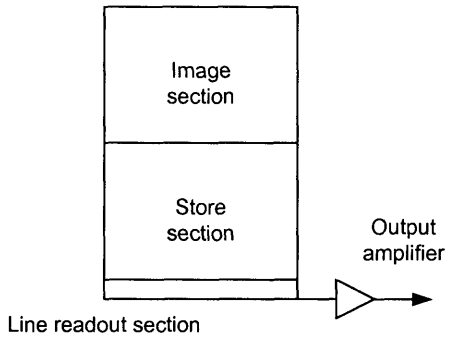

Figure 4-1. Typical CCD schematic

The charge in the image region can be quickly shifted (frame transfer) into the store section. The stored charge is then shifted one row at a time into the line readout section and each pixel is moved sequentially towards an output node and measured. In this way, a charge-map or image, of the whole CCD can be constructed. Chapter 5 describes the method of charge transfer in detail.

4.2.2 Charge generation from X-rays

Absorption of an X-ray photon (<100 keV), in the silicon lattice of a CCD, results most probably (~92% [45]) in the ejection of a photoelectron from the K-shell of a silicon atom. The photoelectron is created with energy E, as given by

$$E = E_x - E_b, \qquad 4\text{-}1$$

where E_x is the energy of the incident X-ray photon and E_b is the silicon K-shell binding energy, 1.85 keV. This reaction will only occur if the incident photon has energy greater than the K-shell binding energy. Lower energy photons will interact with the L-shell, M-shell etc. The excited silicon atom may de-excite either by the Auger process or by fluorescent emission of a photon. In the case of photon emission, the photon will have an energy equal to the K-shell binding energy less the L-shell binding energy, or 1.85 – 0.1 = 1.75 keV. (*With an absorption length in silicon of ~10 μm, this photon has only a small probability of escaping the charge collection area (pixel) completely. In this case it will appear as an escape peak line at 1.75 keV*). Secondary ionisation by the photoelectron and re-absorption of the fluorescent photon can then occur until there is insufficient energy remaining to promote electrons from the valence band into the conduction band. The whole process results in the creation of N electron-hole pairs as given by

$$N = \frac{E_x}{\omega}, \qquad 4\text{-}2$$

where E_x is the energy of the interacting photon and ω is the mean ionisation energy. Since some of the ionisation energy is lost to the crystal lattice (phonons), ω is somewhat larger than the bandgap energy of silicon, 1.1 eV, and found by experiment to be ~3.65 eV. N is a statistical quantity but, since the creation of electron-hole pairs is not mutually exclusive, the variation is less than that given by purely random statistics. The usual Poissonian variance is modified by an empirical quantity known as the Fano factor, F [45] (~0.15 for silicon [46]) and for N is given by

$$\sigma_N^2 = FN . \qquad 4\text{-}3$$

Although ω has a weak dependence on temperature, varying from ~3.62 eV at room temperature to 3.70 eV near absolute zero [47], both ω and F have traditionally been treated as constants when investigating the performance of silicon detectors. However, recent theoretical work [48], confirmed by experiment [49], has shown that the ionisation energy and the Fano factor are both energy dependent.

4.2.3 CCD structure and charge storage

The storage elements of a CCD are essentially an array of metal-oxide-semiconductor (MOS) capacitors. The capacitors comprise a conducting electrode deposited onto the silicon substrate with a thin insulating layer of silicon dioxide between. Each pixel actually contains a coupled number of MOS capacitors, commonly three (figure 4-2) as in the CCD22 device used for the experimental work described in this thesis. Hence, the CCD22 is a 3-phase device.

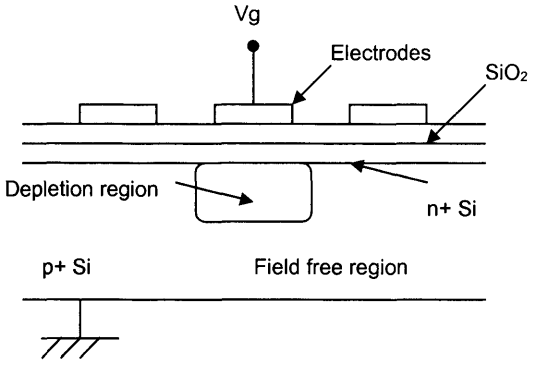

Figure 4-2. Simplified buried channel CCD pixel structure

Application of a positive voltage to one of the conducting electrodes or gates, will create a region depleted of holes beneath the electrode. The n+ silicon layer modifies the shape of the electrostatic potential profile of this depletion region, creating a 'buried channel', which allows charge collection away from the surface, where trapping sites would reduce the charge collection and transfer efficiency. The electrostatic potential profile, in terms of variation of electric field with depth in the silicon, can be derived using Poisson's equation

$$\frac{d^2V}{dx^2} = \frac{e(N_d^+(x) - N_a^-(x) - n(x) + p(x))}{\varepsilon_{si}\varepsilon_0} \qquad 4\text{-}4$$

where e is electronic charge, N_d^+ is the donor concentration in the p+ silicon, N_a^- is the acceptor concentration in the n+ silicon, n and p are the number of thermally generated electrons and holes and ε_{si} and ε_0 are the permittivities of silicon and free space. This equation can be solved numerically and figure 4-3 shows a potential profile for a buried channel CCD using typical dopant concentrations.

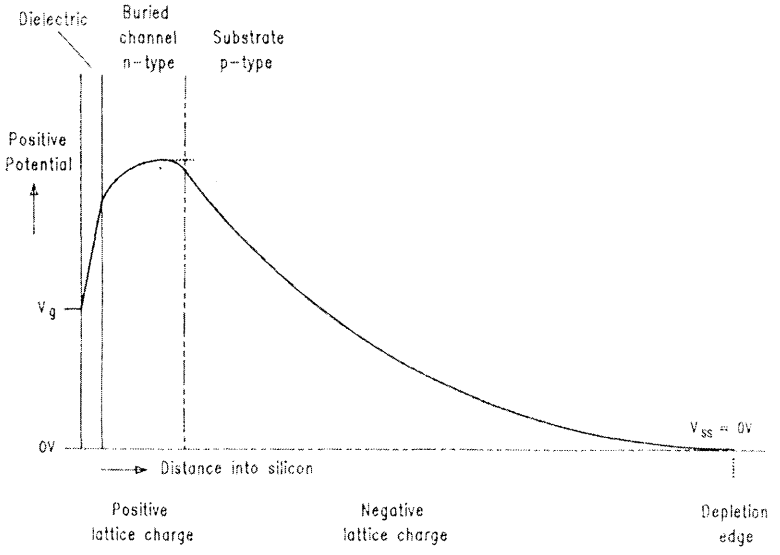

Figure 4-3. Typical potential profile for a buried channel CCD

In a 3-phase device the three electrodes are actually common to one whole row of CCD pixels. In the horizontal direction it is the potential applied to the gate of one of the electrodes which holds the charge in position whilst in the vertical direction 'channel stops' are implanted to prevent migration of the electrons (figure 4-4). The channel stops are heavily doped, electrically inactive, p-type regions. The dimensions of the electrode groups and the spacing between the channel stops define the size of a pixel, typically between 10 and 40 μm square. This array of pixels collectively makes up the imaging area of the CCD.

4.2.4 Charge measurement

Charge generation and storage is usually allowed to continue for a certain 'integration' time after which it is desired to measure the charge stored in each pixel. During integration, generated charge is held in the potential well of each pixel by maintaining the voltage on the gate of one electrode. If the voltage on this electrode is reduced to zero and

simultaneously the voltage on an adjacent electrode is raised, the potential-well and consequently the charge stored in it is transferred, or coupled, from beneath the first electrode to the second.

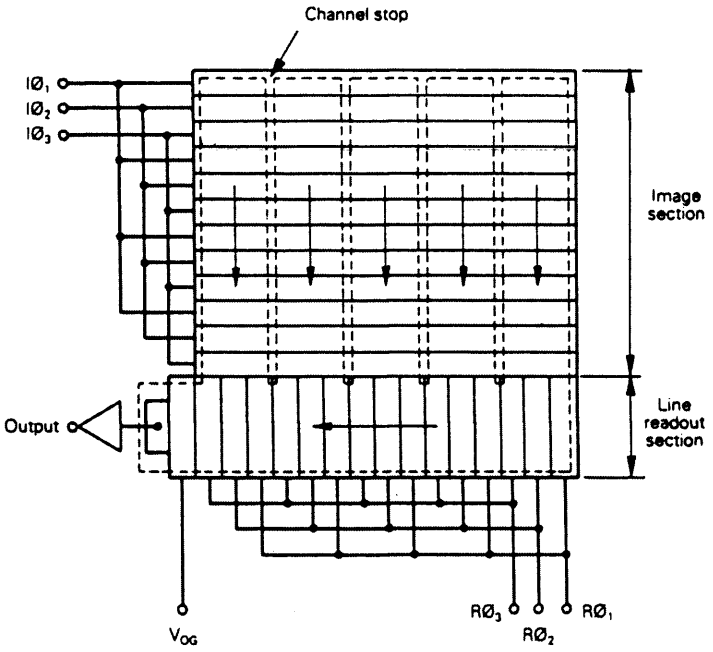

Figure 4-4. Typical CCD array schematic (*from EEV Imaging III*)

If the groups of three electrodes for each row of CCD pixels are arranged consecutively as in figure 4-4 with common electrical connections as shown, and the potential of electrode 3 is lowered as electrode 1 is raised the charge is transferred from one CCD row to the next. This procedure can be repeated as many times as is necessary to move the charge to the end of the CCD array, where a series of pixels couple the charge in a perpendicular direction in an area known as the line readout section.

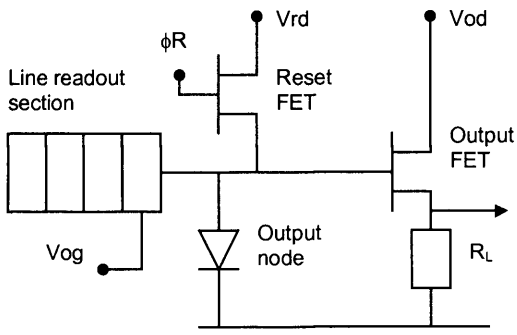

Figure 4-5. Typical CCD output amplifier

Each pixel of the readout register is aligned with a single column of the imaging area and allows a single row of CCD pixel charges to be transferred consecutively towards a charge-sensitive amplifier at the end of the line readout register. Figure 4-5 shows a typical on-chip output charge amplifier and comprises three sections, the output node, which is essentially a diffused diode, a reset FET and an output FET. The output node has an associated capacitance onto which the pixel charge is transferred from the line readout section. This provides a change in voltage on the gate of the output FET of

$$\Delta V_g = \frac{Q}{C_O}, \qquad 4\text{-}5$$

where Q is the charge transferred and C_O is the output node capacitance. The load resistor, R_L in figure 4-5, is external to the CCD and is used to bias the output FET in the linear region of operation. With a typical node capacitance of <0.1 pF and an output FET gain of ~0.7, the CCD will have an output responsivity of ~ 1 μV/electron. The reset FET is used to restore the dc level on the gate of the output FET once the pixel charge has been measured. The bias and operation of the output transistor is discussed in detail in chapter 5, CCD detector operation.

4.3 CCD noise

Noise sources in a CCD are either signal related (shot noise, dark current) or device related (charge transfer losses, reset noise, output amplifier noise).

4.3.1 Signal shot noise

Signal shot noise is the statistical variation of charges produced when an X-ray photon is absorbed in the silicon of the CCD. This process is described in detail in section 4.2.2 and results in the generation of N electron-hole pairs (Eq. 4-2) with a variance given by

$$\sigma_N^2 = \frac{FE_x}{\omega}, \qquad 4\text{-}6$$

where F is the Fano factor, E_x is the energy of the incoming photon and ω is the mean ionisation energy in silicon.

4.3.2 Dark current

Thermal generation of charge, occurring without photo-ionisation (hence the name dark current), occurs when thermal excitation of the silicon lattice provides enough energy

(greater than the bandgap of silicon, ~1.1 eV) to lift an electron from the valence band to the conduction band. At room temperature this can result in ~20000 electrons per pixel per second for a typical CCD with 22 μm square pixels. With a full-well capacity of a few hundred thousand electrons, dark current will quickly saturate the device if it is not cleared. Dark current generation is a poissononian process with the rms noise contribution equal to the square-root of the number of thermal charges. With this level of dark current the noise is substantial, of order 140 electrons rms for the number of charges generated in one second. Dark current generation in a buried channel CCD occurs in three areas, the depletion region, the field-free region and the silicon – silicon oxide interface [50], and can be written

$$I_d = \frac{en_i x_d}{2\tau} + \frac{eD_n n_i^2}{L_n N_a} + \frac{esn_i}{2}, \qquad 4\text{-}7$$

where n_i is the intrinsic carrier concentration, x_d is the depletion depth, τ is the effective lifetime of the minority carriers in the depletion region, D_n is the diffusion constant, L_n is the diffusion length for electrons, s is the surface recombination velocity and N_a is the dopant concentration. In eq. 4-7 the first term is the contribution from the depletion region, the second term is from the field-free region whilst the third term is due to the thermal generation of charges at the silicon-silicon oxide interface. It is the third term which dominates dark current generation in MAT (Marconi Applied Technologies, formerly EEV Ltd) devices [51] and it has a temperature dependence of the form

$$\exp\left(-\frac{E_g}{kT}\right), \qquad 4\text{-}8$$

where E_g is the bandgap energy of silicon (~1.1 eV), k is Boltzmann's constant and T is absolute temperature. Reducing the temperature of the CCD, therefore, will reduce the level of dark current generation. Operating at –100 °C, a typical operating temperature for scientific work, dark current will be of the order of 10 electrons per pixel per hour, and makes no significant contribution to the overall noise performance of the CCD.

4.3.3 Charge transfer losses

In an ideal CCD transfer of electrons or charge from one electrode to the next would be a loss free process i.e. if n electrons are stored under the first electrode, after the transfer is complete there would be n electrons under the second electrode. In a real CCD, however,

this is not the case but buried channel devices come very close to achieving this ideal. Charge transfer efficiency (CTE) is usually of the order 99.9995% for a single transfer. If the charge loss per transfer is small, the total charge lost per pixel, Q_l, can be approximated by

$$Q_l \approx N(1-CTE)n, \qquad 4\text{-}9$$

where N is the number of transfers and n is the number of electrons in the charge packet. The charge loss is Poissonian and the rms noise associated with a pixel is given by

$$\sigma_{CT} = \sqrt{Q_l}\,. \qquad 4\text{-}10$$

4.3.4 Reset noise

Resetting the output diode to the reference potential (section 4.2.4) is subject to thermal variation, with rms noise in volts given by

$$\sigma_{reset} = \sqrt{\frac{kT}{C_o}}, \qquad 4\text{-}11$$

where k is Boltzmann's constant, T is absolute temperature and C_o is the output node capacitance. At –100 °C, with a typical output node capacitance of 0.1 pF, this is equivalent to ~100 electrons rms. This source is one of the largest contributions to overall CCD read noise. X-ray spectroscopic performance, where signal charges are of order 1500 electrons, would be very poor with this level of noise. Fortunately, the reset noise can be effectively cancelled using a technique known as correlated double sampling, where the reset level is sampled and subtracted from the measured charge level in each pixel. This operation is discussed in more detail in Chapter 5.

4.3.5 Transistor noise

The output FET has two main noise components, flicker or 1/f noise and Johnson noise. The 1/f noise, so called because it is inversely proportional to frequency, is thought to be due to trapping and release of signal charge carriers in the conduction channel. The Johnson noise component arises from the random thermal motion of the electrons and has a flat band response. Due to its temperature dependence it is also known as thermal noise.

Post-processing of the CCD output signal is usually employed to reduce the impact of both 1/f and white noise from the transistor (Chapter 5).

4.4 CCD X-ray performance

4.4.1 Resolution

The energy resolution of a CCD is dependent upon the noise sources described in section 4.3 and can be expressed as

$$\Delta E(FWHM) = 2.355\omega\left(\frac{FE_x}{\omega} + \sigma_T^2\right)^{\frac{1}{2}}, \qquad 4\text{-}12$$

where the first term in the brackets is the Fano modified signal shot noise and σ_T is the total rms read noise of the CCD in electrons. Ultimate resolution is achieved by minimising the noise terms associated with σ_T and in this case the detector performance is termed Fano limited. For a typical read noise of 5 electrons rms a FWHM of <150 eV can be achieved at ^{55}Fe (5898 eV).

4.4.2 CCD characteristics and quantum efficiency

A standard front illuminated CCD is typically manufactured using low-resistivity (50 Ω.cm) 25 μm epitaxial silicon, on a 550 μm p+ silicon substrate (figure 4-6). The epitaxial silicon surface is passivated, first with a 0.1 μm layer of silicon dioxide and then with a similar thickness of silicon nitride. On top of the passivation layers are the three electrodes, constructed by depositing n-type polycrystalline silicon (polysilicon), with an insulating layer of silicon dioxide between electrodes. The electrodes overlap in the manner shown but are nominally the same width (~1/3 pixel width), providing a similar depletion capability underneath each one. Finally, a vapour deposition of silicon dioxide (VAPOX) is applied to protect and passivate the CCD surface. When the gate potential is applied to the electrode, a typical depletion depth of 5 μm is achieved with a corresponding field-free region of 25 μm.

Quantum efficiency (QE) is defined as the ratio of number of X-rays detected to number of incident X-rays and is expressed either as a value between 0 and 1 or as a percentage. For an X-ray to be detected by the CCD it must interact in the epitaxial silicon and this process is affected by two areas of CCD design, (a) the electrode structure and (b) the epitaxial thickness.

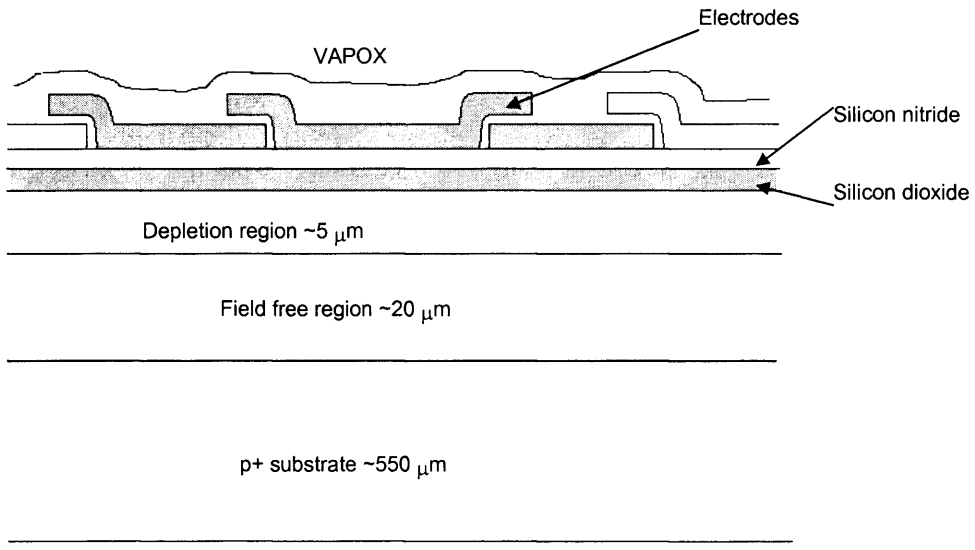

Figure 4-6. Standard 3-phase CCD structure

Charge generated in the electrode structure is not collected and essentially forms a dead layer ~1.5 μm thick on the surface of the CCD. Absorption of X-rays in this layer determines the low energy response of the CCD. Charge collected in the p+ substrate diffuses and is lost, effectively reducing the high-energy response.

The epitaxial region comprises the depletion (or field) layer and the field-free layer (figure 4-6) and detailed modeling of the X-ray response within this region has been performed [52]. Charge generated in the depletion region is usually contained within the pixel where the X-ray interaction occurred. These events are termed isolated events. However, charge generated in the field-free region tends to diffuse further where some may be lost due to recombination and the rest is eventually collected in several pixels. Although this 'spread-event' charge may be summed, once read-out has occurred, to recover (or reconstruct) the charge level of the original event, the best X-ray spectroscopic performance is achieved when only isolated events are used. The thin epitaxial layer and low-resistivity (and hence depletion depth) of a standard CCD determine the high energy response of the CCD. The QE for a standard CCD over the 0.1 – 10 keV range, is shown in figure 4-9. The rapid fall off in response above ~3 keV and below 0.7 keV is apparent.

4.5 CCD22

The European Photon Imaging Camera (EPIC) on board the XMM-Newton X-ray telescope is an instrument with good X-ray QE over the 0.1–10 keV range. The focal plane of the telescope is constructed from seven CCDs, of type CCD22 [53], developed jointly by the University of Leicester and MAT Ltd specifically for the XMM-Newton mission. As

already discussed in section 4.4, a standard CCD is sensitive to X-rays in this energy range, but has very poor QE at low energies (due to absorption in the electrode structure) and at high energies (due to limited depletion depth). The CCD22 has been designed to overcome these limitations. All experimental data described in this thesis were taken with CCD22 devices.

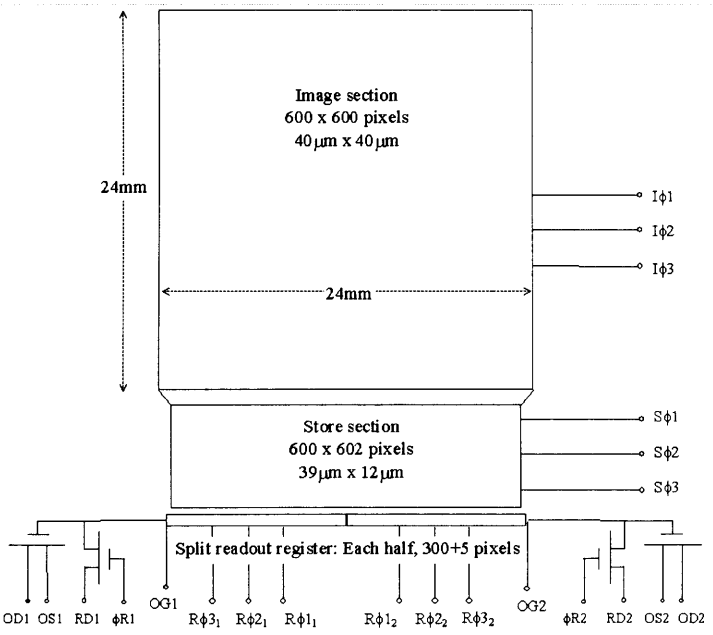

Figure 4-7. CCD22 schematic

4.5.1 CCD22 architecture

The CCD22 is a 3-phase, frame-transfer device with 600 x 600, 40 μm square pixels in the image region. The store region has 600 x 602 pixels, but these are not square and allow the store section to be reduced in size, making a more compact CCD. The serial register is split, with a read-out node at either end. Charge can be clocked out of either node or both nodes simultaneously, depending upon clocking operation. Figure 4-7 shows a simplified schematic of the CCD22.

To maximise the high energy QE, the CCD22 is manufactured using 80 μm epitaxial, high-resistivity silicon (4000 Ω.cm). With the gate potential applied, a depletion depth of 30-40 μm is achieved with a corresponding field free depth of 40-50 μm. In a standard CCD, it is the electrode structure which limits the low energy QE of the device. In the case of the CCD22, a novel 'open-electrode' structure was created. This is illustrated in figure 4-8.

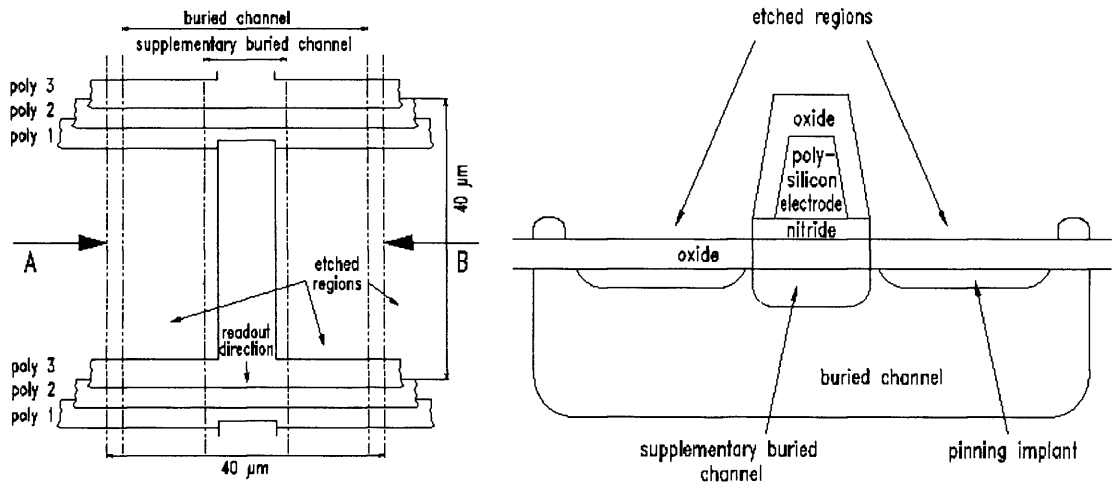

Figure 4-8. CCD22 electrode structure with cross section A-B expanded.

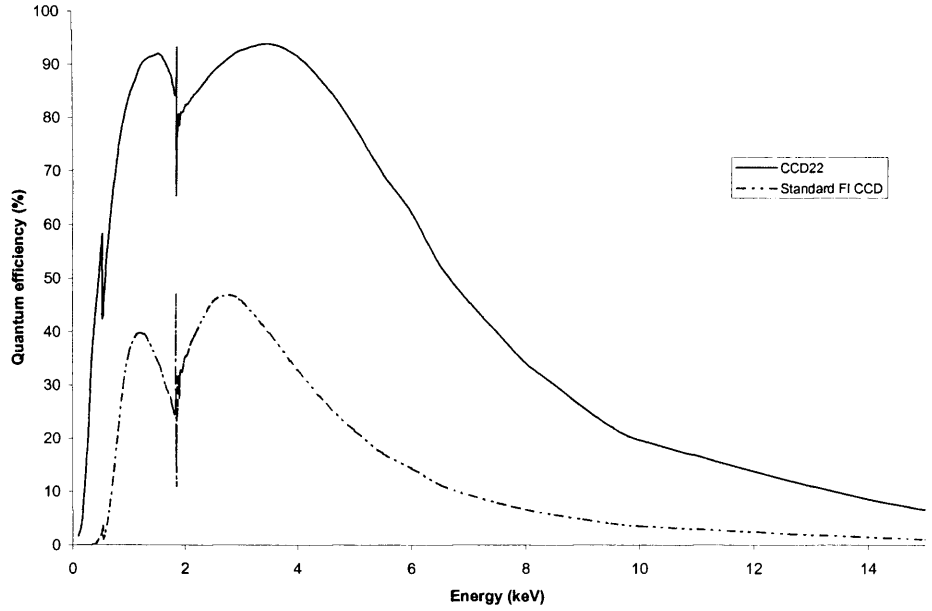

Figure 4-9. QE curves for standard front-illuminated CCD and the open-electrode CCD22.

In a standard CCD, the three electrodes are nominally the same width, approximately 1/3 of the pixel size. In this case the electrode structure covers the whole of the pixel surface and provides a barrier to low energy X-rays, reducing the detection efficiency. In the CCD22, the width of electrodes 1 and 2 are reduced substantially, whilst electrode 3, although much wider, is etched away, leaving a tapered T-shape structure (figure 4-8). Each pixel now has an open area of ~40%, etched away to the silicon dioxide level. Absorption of low-energy X-rays in the open-electrode area is greatly reduced, giving a substantial increase in QE at low energies (figure 4-9).

5 CCD detector operation

This chapter describes the operation methods of CCDs. Clock and bias operating requirements are explained and different methods of CCD signal processing are discussed. Finally, the evaluation of the experimental CCD22 devices is presented.

5.1 Introduction

The operation of CCDs, in contrast with many other (X-ray) detectors, requires a large number of control signals. These include clock signals for the various sections of the device and a number of different voltage sources for correct biasing of the detector. Use in X-ray photon counting applications in addition requires low noise operation (chapter 4), which in turn requires low noise electronics to drive the CCD and the application of signal processing techniques to remove inherent detector noise. The noise contribution from thermally generated 'dark current' has already been discussed in chapter 4 and can be an order of magnitude higher than the noise of the X-ray measurement [54]. By cooling the detector to temperatures of order –90 °C, it is possible to reduce the dark current noise to negligible levels [55] and this is now a standard technique in scientific CCD detector operation. The remainder of this chapter assumes cooled CCD conditions as the starting point for achieving low noise operation.

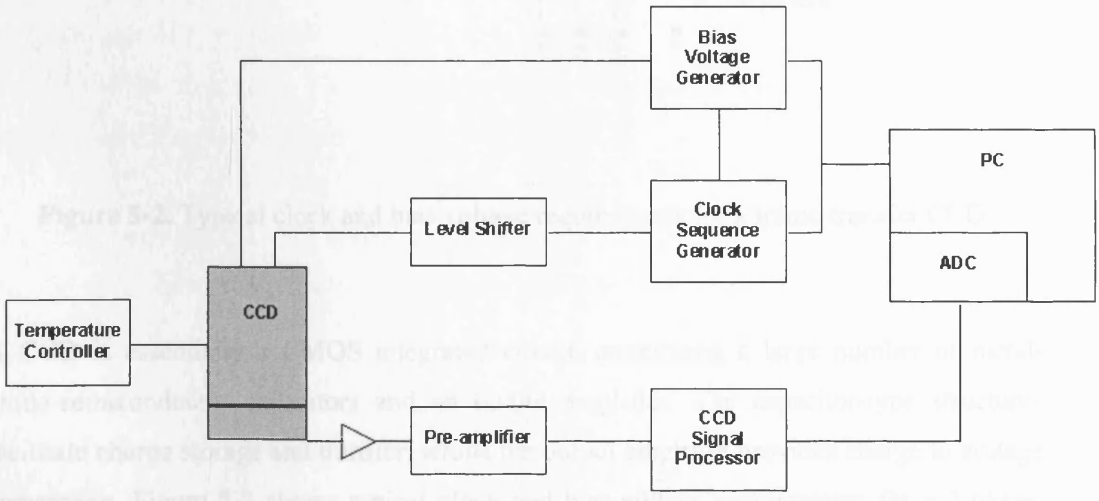

Figure 5-1. Typical arrangement for low-noise operation cooled CCD.

5.2 Detector operation overview

Figure 5-1 shows a typical arrangement used for low-noise operation of a cooled CCD. Electronic circuits provide the bias voltages and a clock-sequencing device generates the clocking signals. The clock signals are then level-shifted to adjust the amplitude necessary

for charge transfer (chapter 4). The CCD output is amplified and passed through a signal processor, usually employing a method of correlated double sampling (CDS), for noise reduction. Finally, the output signal from the CDS processor is digitised, using an analogue to digital converter (ADC) and stored on a computer. The following sections describe each of these requirements in detail. Specific CCD descriptions are based upon a typical Marconi Applied Technologies (MAT - formerly EEV) 3-phase, frame-transfer CCD. CCDs are also available as full-frame devices, or with 2- or 4-phase operation. Although not discussed here, the basic principles are the same and it is a relatively simple matter to understand the operation of these devices from an understanding of 3-phase operation.

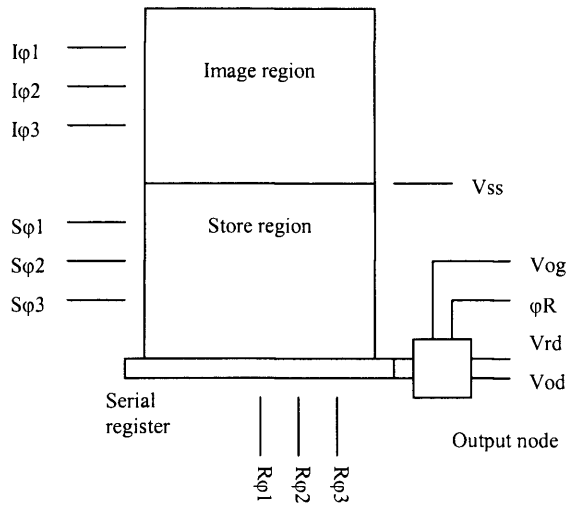

Figure 5-2. Typical clock and bias voltage requirements for a frame-transfer CCD.

A CCD is essentially a CMOS integrated circuit, comprising a large number of metal-oxide-semiconductor capacitors and an output amplifier. The capacitor-type structures facilitate charge storage and transfer, whilst the output amplifier provides charge to voltage conversion. Figure 5-2 shows typical clock and bias-voltage requirements for a 3-phase, frame-transfer CCD.

5.3 CCD biasing

The substrate of a CCD is usually connected to ground or some potential above this. MAT CCDs typically have a substrate voltage of 3 – 6 V. All other voltages (clocks and bias) are referenced to substrate.

5.3.1 CCD output amplifier

Since the CCD substrate material is n-type, the on-chip output amplifier of an MAT CCD is typically a p-channel depletion MOSFET arranged as a source-follower (figure 5-3). R_L is either a load resistor or a constant current source and is external to the CCD.

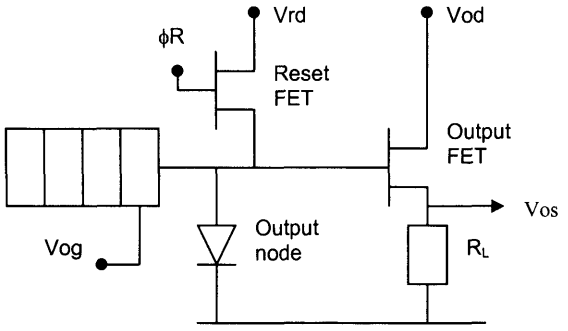

Figure 5-3. CCD output amplifier – FET source-follower.

The output transistor needs to be operated in the saturated part of its characteristic for linear operation. A low drain current allows the transistor to function in 'buried-channel' mode with current conduction taking place away from possible charge trapping sites near the silicon surface. This can result in greatly reduced low frequency noise, especially at low temperature [56]. The low drain current typically means that the transistor is operating in depletion (a depletion MOSFET is capable of operating in either depletion or enhancement parts of the characteristic). This in turn means that the output source tends to sit at a higher potential than the gate voltage.

The exact operating point of the output transistor is determined by the gate-source voltage and the drain current, i_d. These parameters are related by the transconductance, g_m, of the FET as follows,

$$i_d = g_m v_{gs} = g_m(v_g - v_s) \ . \qquad 5\text{-}1$$

In practice, the drain current and gate-source voltage are set with a combination of load resistor R_L and the reset transistor voltage, V_{rd}.

The output source voltage can be described by

$$v_S = i_d R_L \ , \qquad 5\text{-}2$$

and combining this with eq. 5-1, we obtain a relationship for the output voltage in terms of the input voltage as follows,

$$v_s = \frac{R_L g_m}{1 + R_L g_m} v_g \ . \qquad 5\text{-}3$$

With a typical load resistor value of 5000 Ohms and an FET transconductance of 500 μMho, we get $v_s \sim 0.7 v_g$, i.e. a reasonably good 'follower'.

The output gate voltage, V_{og} (confusingly, not the gate voltage of the output transistor), is used to bias the end of the serial register to prevent charge from flowing back under the final electrode. Transfer of charge Q onto the capacitive (C_O) output node causes a voltage change

$$\Delta v_g = \frac{Q}{C_O} \qquad 5\text{-}4$$

at the gate of the output transistor. The corresponding change in output source voltage, Δv_s can be calculated using eq. 5-3. Typical node capacitance is of order 0.1 pF, giving output responsivities of order 1.6 μv/electron.

5.4 CCD clock sequencing

In a CCD, the pixels are defined in horizontal direction by the electrode structures and in the vertical direction by the channel stops (figure 5-4). In a frame-transfer device this format is used to create an image region and a store region of pixels, where the pixels in any row are linked by a common electrode structure but divided by the perpendicular channel stops. At the base of the store region, a line readout section or serial register is created. The electrodes in this register are arranged at right angles to, and to coincide with, the pixel structure of the rows in the store region. A single row of pixels may be transferred from the store region into the serial register and then clocked, one pixel at a time, into the output node of the CCD. The operation of a frame-transfer CCD can be divided into three parts; image integration, frame transfer and store region read out.

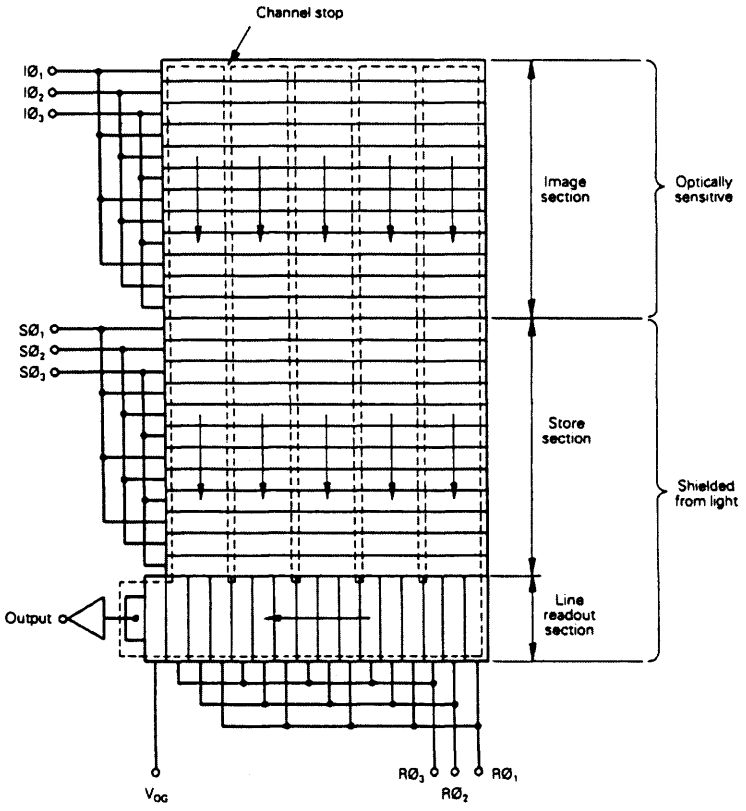

Figure 5-4. Typical 3-phase, frame-transfer CCD schematic (*EEV Imaging III*).

5.4.1 Image integration

Image integration is simply the exposure time of the image section to the source, prior to transfer of the image section charge into the store section. Integration usually occurs with a single electrode energised, typically phase 2 in a 3-phase device.

5.4.2 Frame transfer

Once the desired integration time is achieved, a frame transfer operation is performed to transfer charge from the image section to the store section. The image section and store section clocks are operated simultaneously in the order shown in figure 5-5. The crossover point typically occurs at 50% amplitude, with rise times of order 500 ns. Once this operation is complete (typically 20-30 ms) integration in the image section can begin again. Whether imaging optical or X-ray photons, it is usual for the store section of the device to be covered with an opaque material to prevent photon detection during readout smearing the image. This effectively provides an electronic shutter.

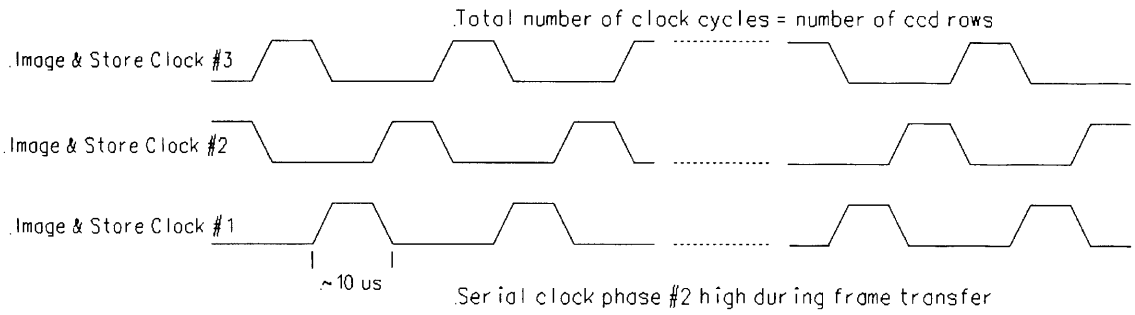

Figure 5-5. Frame transfer clock operation.

5.4.3 Store region read out

After frame transfer, the charge in the store section is transferred one row at a time into the serial register by performing a single cycle of the Store section clocks only. The charge in the serial register is then transferred one pixel at a time onto the output node of the CCD. The clock pattern to perform this operation is shown in figure 5-6.

The rise and fall times of the reset and serial clocks are typically 100 ns. The crossover point is shown at 50% but can vary with CCD type. In some cases 100% clock overlap may be required to ensure complete charge transfer.

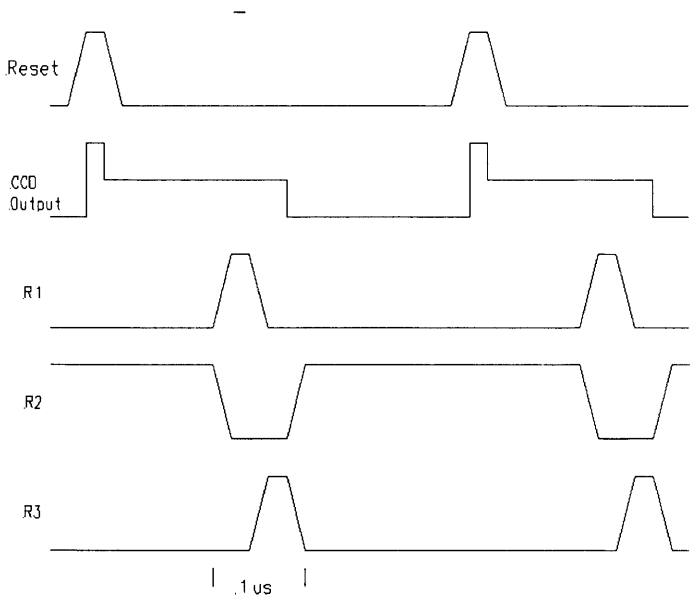

Figure 5-6. CCD output clock pattern.

The read-out of charge from a single row of the store section of the CCD proceeds as follows. A single cycle of the three store section clocks transfers the charge from the final

row of the store section into the serial register (figure 5-5). The following sequence, illustrated in figure 5-6, is then repeated for each pixel in the serial register, equivalent to the number of pixels in a single row of the CCD.

1. The output node of the CCD is reset by pulsing the Reset clock input high for typically 150 ns.

2. The CCD output reset level is then available for sampling (see section 5.5).

3. The serial register clocks are cycled. On the falling edge of R3, the charge is transferred from the end of the serial register onto the output node of the CCD.

4. The CCD output charge level is then available for sampling.

5.5 CCD signal processing

5.5.1 Pre-amplifier

Since the CCD is typically operated in a vacuum chamber (for cooled operation), it is usually located some distance from the electronics. Also the output signal of a CCD is quite small (~1 - 5 μV/electron). Consequently, a pre-amplifier is normally situated as close to the output of the CCD as possible.

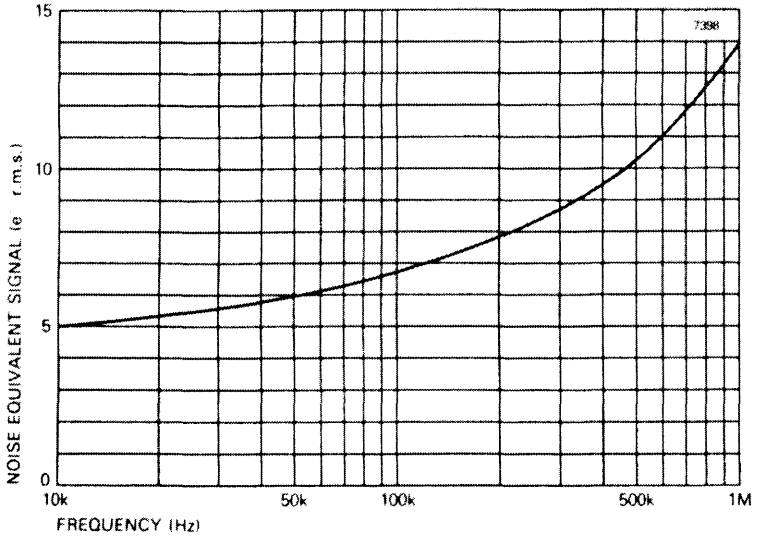

Figure 5-7. Typical CCD output transistor noise spectrum [57].

A typical CCD output transistor noise spectrum is shown in figure 5-7. At slow scan read-out rates of 20 kpixels/second, the CCD noise contribution is <5.5 electrons rms. With an output responsivity of 1.6 μV/electron this is equivalent to ~9 μV rms noise at the input of the pre-amplifier. It is important in amplifier selection and design that the CCD noise dominates at this point if low noise operation is to be achieved.

5.5.2 Correlated double sampling

In slow-scan, low noise operation, the greatest contribution to the read-noise from a cooled CCD is generated by uncertainty in the dc level achieved after resetting the output node of the device (section 5.4.3). This variation, typically a few hundred electrons, can be effectively removed by a technique known as correlated double sampling (CDS) [58, 59]. This method involves sampling the output of the CCD twice for each pixel. First, the CCD output node is reset, allowed to settle and then sampled. This value (the reset level) is stored. The pixel charge is then clocked onto the output node, allowed to settle again and then sampled. This new level is equal to the charge level + reset level. If the previously stored reset level is now subtracted from (correlated with) the new level, a value for the pixel charge alone is obtained, independent of the variation in the previous reset level. This technique can be performed in various ways, either in the analogue or the digital domain. Three common methods are described below.

5.5.3 Clamp and sample

The basic circuit is illustrated in figure 5-8.

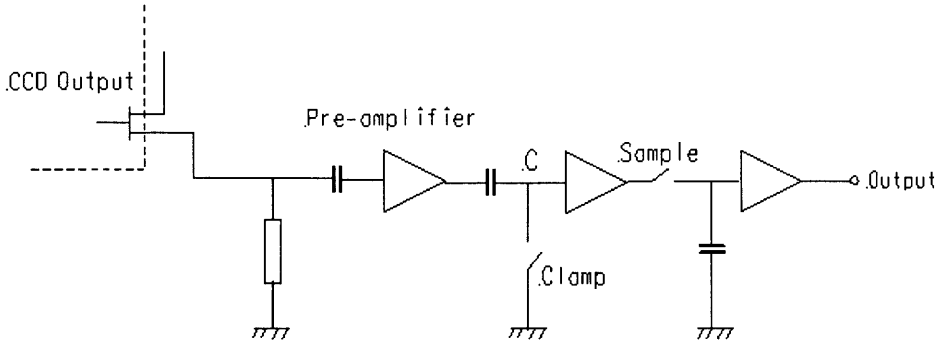

Figure 5-8. Basic clamp and sample circuit.

The simplest way to understand the operation of the circuit is to study signal waveforms at different points. These are illustrated in figure 5-9. The CCD output waveform is as described in section 5.4.3 and figure 5-9 can be correlated with figure 5-6 to link the

sequences together. Once the reset level has settled, the clamp switch is momentarily closed (clamp signal) which clamps the voltage at point C to ground. The clamp is then released and the pixel charge clocked onto the CCD output. The change in voltage is transferred across the capacitor and the voltage at point C now represents the pixel charge signal only, since the variation due to the reset level has been removed. The sample switch is closed and the charge level stored on the final capacitor.

The noise performance of the clamp and sample technique is limited by the need to low-pass filter the CCD output, otherwise the clamped signal will be influenced by high frequency noise. Since the filtering slows the rise and fall times of the CCD signal the minimum time between clamp (reset) and sample operations is limited reducing the ability to discriminate against low frequency noise.

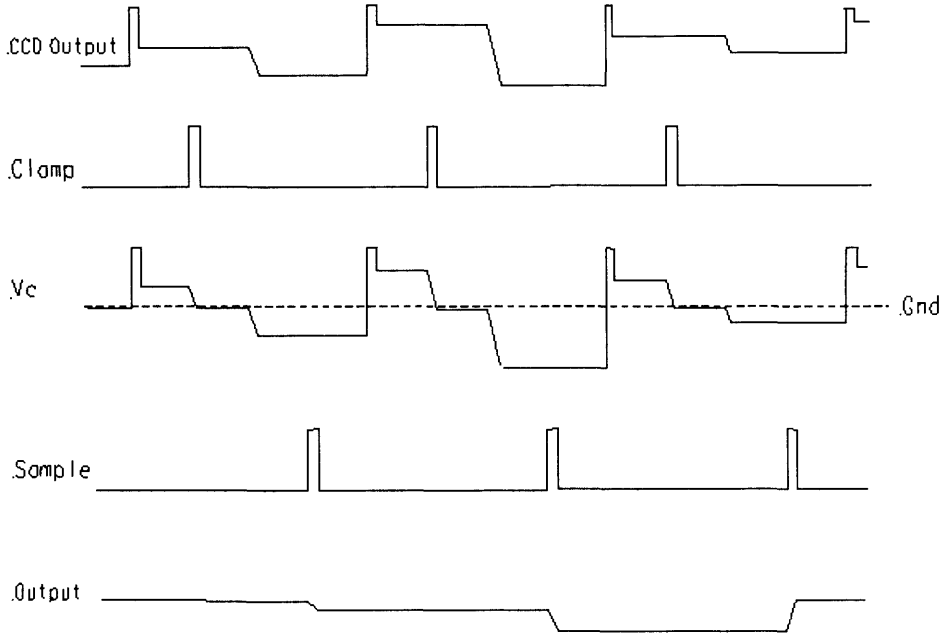

Figure 5-9. Clamp and sample circuit waveforms.

5.5.4 Dual-slope integration

There are various schemes using dual-slope integration. A typical arrangement is shown in figure 5-10.

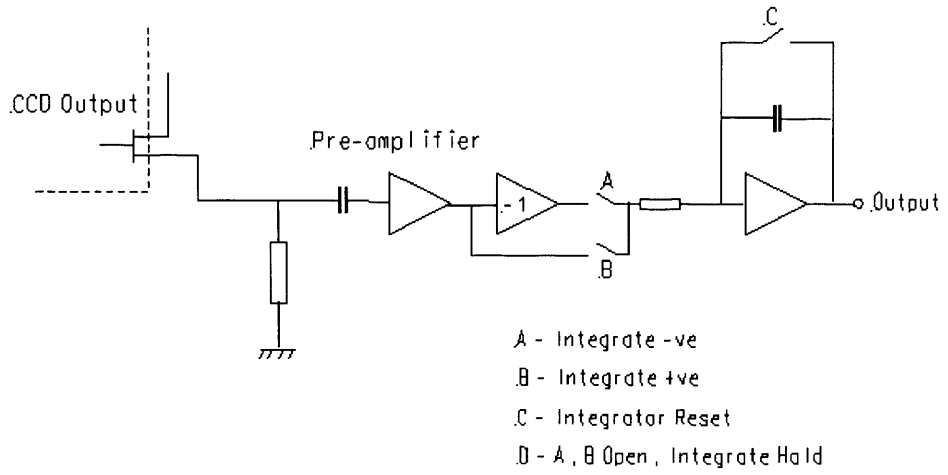

Figure 5-10. Dual-slope integrator CDS circuit.

Again, the operation of the circuit is best illustrated by studying the output waveform, illustrated in figure 5-11.

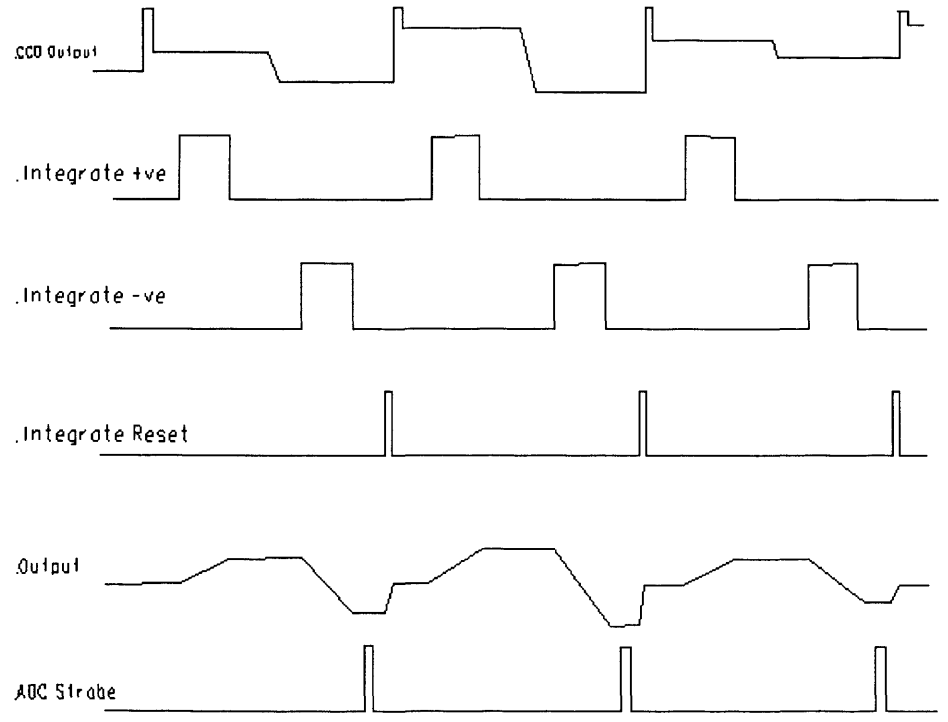

Figure 5-11. Dual-slope integrator output waveform.

After allowing the reset level to settle, switch A is closed for a time period, t. During this period, the reset level signal is integrated onto the feedback capacitor of the integrator. Integrator hold is then selected, by opening switch A (switch B is already open) and the pixel charge clocked onto the output node. Switch B is now closed, the output of which has

a reverse polarity to the output of switch A, and this 'negative' signal integrated with the previously held reset level, for the same period, t. The reversal of polarity between reset and charge level integrations produces the necessary subtraction of the variable reset level. Integrator hold is selected again while the output value is digitised (ADC Strobe) and then switch C is closed to reset the integrator ready for the next pixel.

The dual-slope integrator generally produces the best noise performance of the CDS circuits discussed here. The main reason for this is the inherent low-pass filtering of the CCD signal during the integration phases, which essentially averages the input level over the integration period, t (typically 5 - 20 μs). The noise spectrum for a dual-slope integrator with an integration period of 10 μs is shown in figure 5-12.

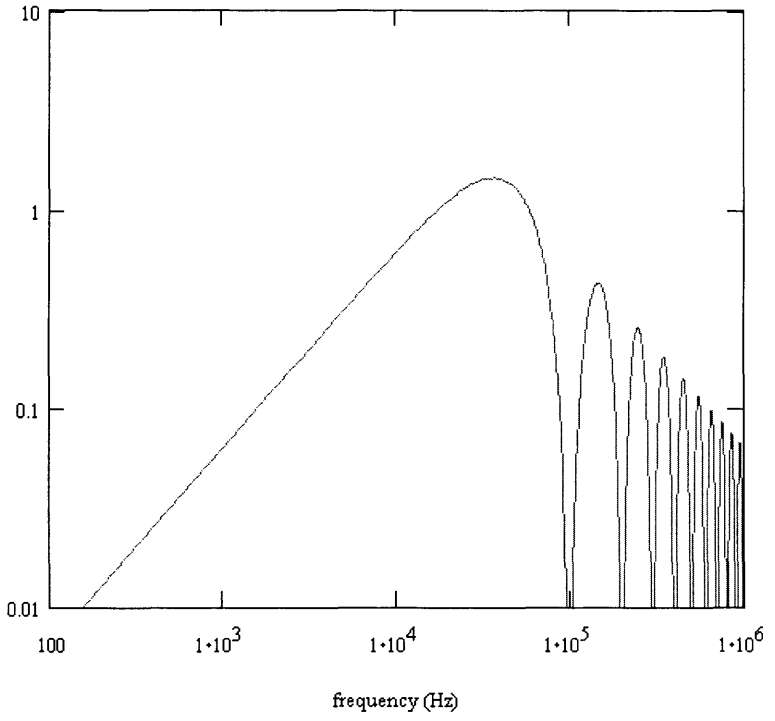

Figure 5-12. Noise spectrum of dual-slope integrator (t = 10 μs).

If we now correlate this curve with the noise spectrum of the CCD output transistor (figure 5-5), a noise spectrum of the sampled CCD signal is obtained, figure 5-13. Not only is reset noise eliminated but also the noise contribution from the CCD output transistor is greatly reduced especially at lower frequencies. Noise levels of <10 μV r.m.s. are achievable, equivalent to ~6 electrons r.m.s with a typical node capacitance of 0.1 pF.

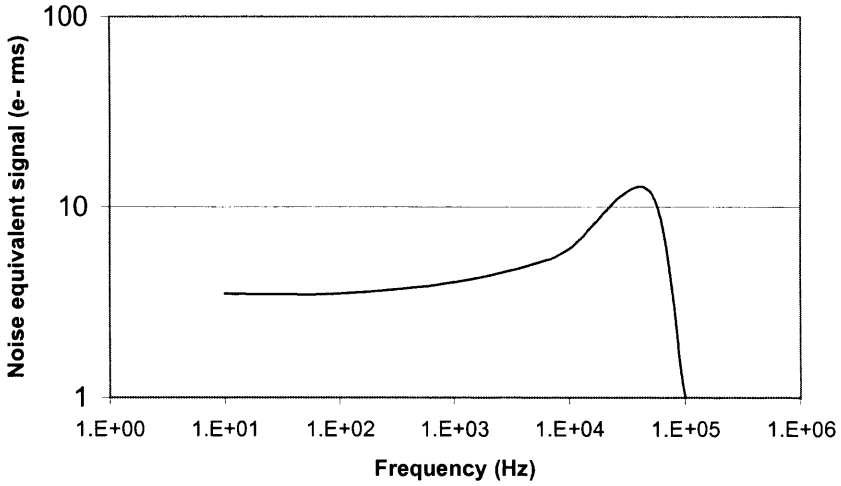

Figure 5-13. Noise spectrum of CCD signal after dual-slope integration (τ = 10 μs).

5.5.5 Digital double sampling

In this method, the subtraction is performed in the digital domain. Amplification and some form of low-pass filtering are usually applied to the CCD output signal. The reset level is digitised and then the pixel charge clocked onto the CCD output node. This new level, representing the variable reset level plus the pixel charge level, is also digitised and the two values correlated. This method can be combined with a variation of the dual-slope integration process, where the reset and charge levels are integrated and stored (in the analogue domain) separately and then digitised and subtracted in the digital domain.

5.6 CCD22 evaluation

Eight CCD22 devices were ordered from EEV (now E2V Technologies), six grade 1 and two set-up grade CCDs. The CCD packages (see section 7.5) were designed at Leicester University, originally for use on the EPIC cameras on board the XMM-Newton X-ray telescope. Eight new packages were assembled and tested and supplied to EEV for application of the CCD. The CCDs were evaluated for cosmetic appearance, charge-transfer efficiency and read-noise. These tests were performed in a laboratory cryostat with the experimental electronics (see chapter 7 for a full description) using a Dual Slope Integrator CDS amplifier (section 5.5.4). Each CCD was tested individually, under vacuum at –100 °C. Optimum operating voltages and timing parameters were also investigated. This is an important test since each column of CCDs is operated by a single set of bias

voltages and clocks, with the exception of the output drain voltage, which is controlled separately.

Using the typical operating voltages supplied by EEV, CCD images were acquired for an initial appraisal of the cosmetic appearance. As expected, only the two set-up grade devices exhibited any cosmetic defects. These were in the form of bright columns (only two per set-up grade CCD), created by the charge generated in a 'hot' pixel, which floods the column during frame-transfer or read-out. Since the detector is not used for imaging, the only degradation due to bright columns is a small loss in collecting area (1/600 of the CCD area per bright column). Figure 5-14 shows a typical 10-minute exposure taken using a grade 1 device. Several cosmic ray traces are apparent with an oblique interaction in the upper right. The lack of defects or bright columns is obvious.

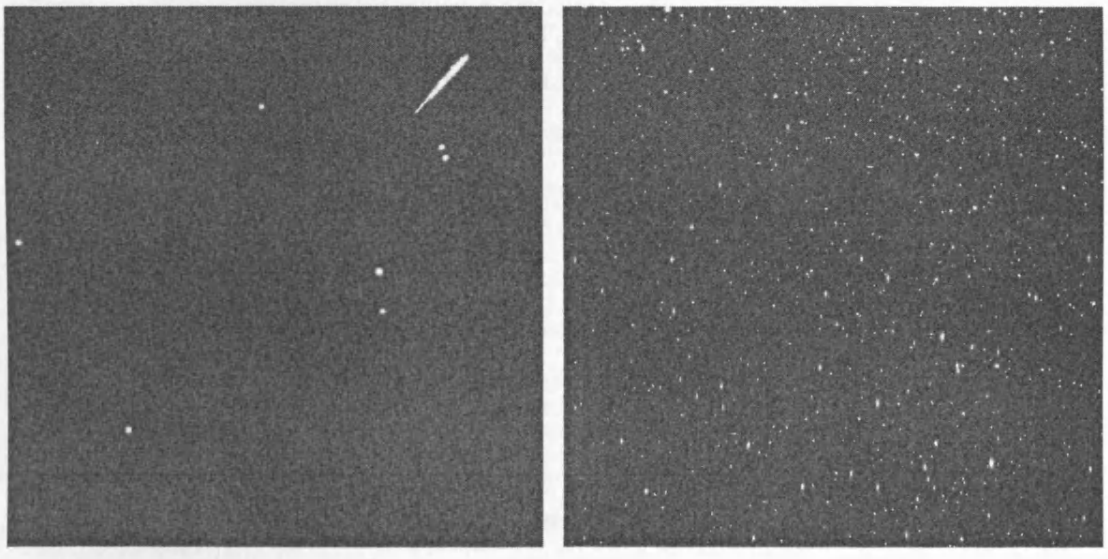

Figure 5-14. CCD22 images, showing cosmic ray interactions (left) and titanium X-rays (right).

The read-noise and energy calibration of each CCD was determined using titanium X-rays (4.51 keV) fluoresced by an ^{55}Fe source. A CCD image was acquired where the majority of active pixels contained charge generated by a single X-ray photon (figure 5-14 right) and an energy histogram produced (figure 5-17).

Using a simple gaussian fit, the peak positions of the titanium Kα line and the background noise peak (equivalent to zero energy) were determined, in ADC units. Since the energy of the titanium line is known (4.51 keV), the energy scale can be calibrated as follows:

$$Cal = \frac{X_{energy}}{X_{pk} - N_{pk}} \text{ eV/ADC unit,} \qquad 5\text{-}5$$

where X_{energy} is the energy of the incident X-ray, X_{pk} is the X-ray peak position in ADC units and N_{pk} is the zero energy (noise) peak position in ADC units. The standard deviation of the noise peak and the full-width half maximum (FWHM) of the X-ray line can now be determined in eV. The noise figure is more commonly quoted in electrons rms, obtained by dividing the value in eV by 3.68, the average energy required to create an electron-hole pair (see section 4.2.2). After adjusting the CCD bias voltages, this process was repeated until the read noise was minimised. The pixel integration time of the dual-slope integrator CDS is variable and the noise was investigated for different values. The results for a typical CCD are plotted in figure 5-15.

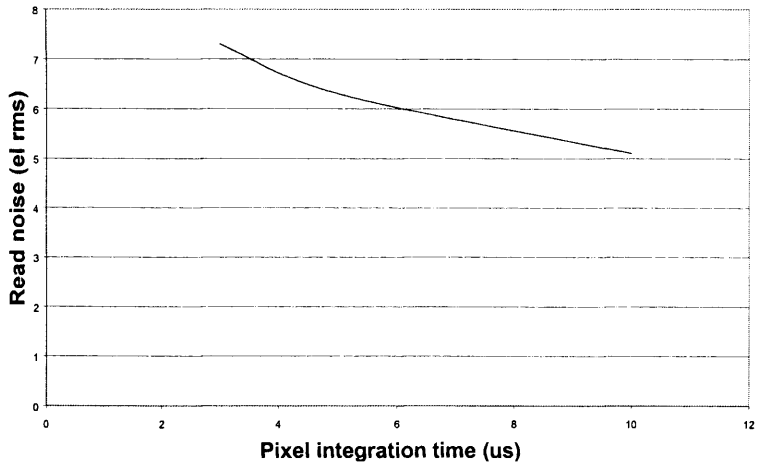

Figure 5-15. Noise versus pixel integration time for CCD22 using dual-slope integrator CDS.

CCD	Read noise (e^- rms)	Ti Kα FWHM (eV)
1	4.88	148
2	5.00	130
3	5.01	136
4	4.76	130
5	5.59	132
6	4.81	130
7	5.30	133
8	4.91	132

Table 5-1. Read noise and titanium X-ray peak FWHM evaluation results.

A 10 μs pixel integration time was selected for operational use and Table 4-1 lists noise and FWHM results for all eight CCD22 devices. Calibration was 1.6 eV/ADC unit.

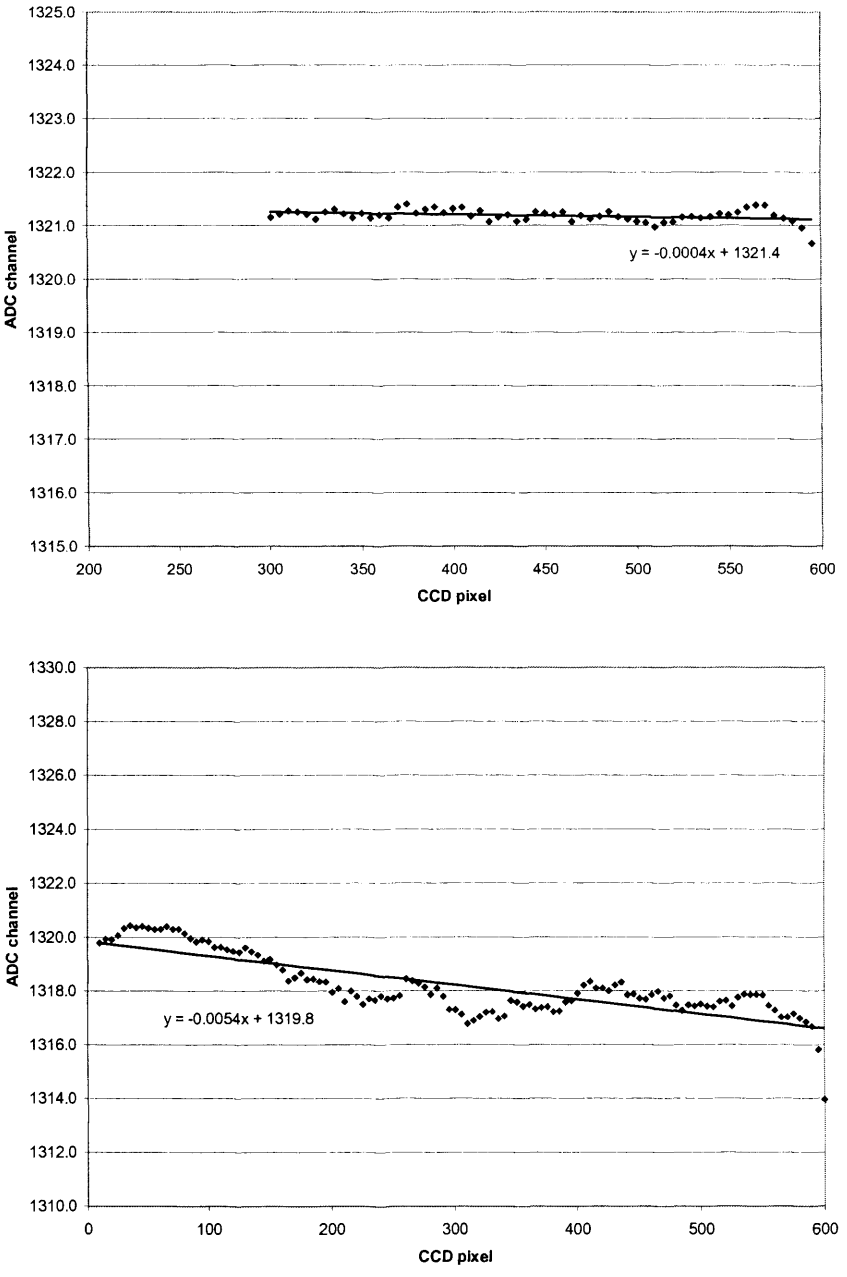

Figure 5-16. Parallel (top) and serial (bottom) CTE measurment of CCD22. Mn K X-rays (5.9 keV) were used and the pixel data has been averaged.

Once the read-noise had been minimised, the charge-transfer efficiency (CTE) was investigated (section 4.3.3). Poor CTE can result in degraded energy spectra, which in turn affects event recognition and reconstruction. CTE was examined in both the parallel and serial transfer directions using Mn K X-rays (5.9 keV). Only isolated events were used and

rows (or columns) were binned and averaged. The results were then plotted against pixel position. A straight line was fitted to the data points, the slope of which is proportional to the charge loss during transfer. The results for both parallel and serial CTE tests from a single CCD22 device are shown in figure 5-16, with the straight-line equations displayed in each case. The CTE is given by

$$CTE = 1 - \frac{m}{A}, \qquad 5\text{-}6$$

where m is the slope of the fitted line and A is the average pixel charge (in ADC units). Substituting the slope values from figure 5-16, we obtain

$CTE_{parallel}$ = 99.9999 %/pixel transfer,
CTE_{serial} = 99.9996 %/pixel transfer.

These values are typical of all eight devices with none falling below 99.9995% in either direction.

The final set of optimised CCD operating voltages are shown in table 5-2. Compatibility between different devices is very good and even the output drain voltages are the same for each CCD.

CCD voltage	Optimised value (V)
Image clock	3.5
Store clock	7.4
Serial clock	10.7
Reset gate	6.0
Input drain (Vid)	16.8
Reset drain (Vrd)	15.3
Output drain (Vod)	20.0
Output gate (Vog)	1.9
Guard ring (Vgr)	20.0
Substrate (Vss)	1.5

Table 5-2. CCD22 optimised operating voltages.

Once optimised, the spectral performance of the CCDs was investigated in more detail. This was again performed using titanium X-rays fluoresced by an ^{55}Fe source. Using the

technique described above, the CCD outputs were calibrated and fifty frames of thresholded CCD data recorded, taken with a 10 s frame integration period (Figure 5-17).

The top plot shows an energy histogram of all active CCD pixels. Multiple pixel events, where the charge generated by a single X-ray photon is spread over several pixels, appear in the spectrum between the areas indicated. In the middle plot, only isolated CCD events are shown. The area below the titanium Kα peak is now much cleaner with the spread event charge removed. The bottom plot shows the same spectrum but with the vertical scale expanded. The titanium escape peaks are now clearly visible along with the associated silicon K (1.73 keV) line. Manganese Kα (5.9 keV) is from the ^{55}Fe source directly whilst the aluminium (1.49 keV) is from the ^{55}Fe source mount or part of the laboratory cryostat. The line at 3.7 keV is probably calcium, from a separate target on the target wheel. The full width half maximum (FWHM) of the titanium peak is typically 130 eV (Table 5-1), while at manganese (5.9 keV) it is typically 150 eV.

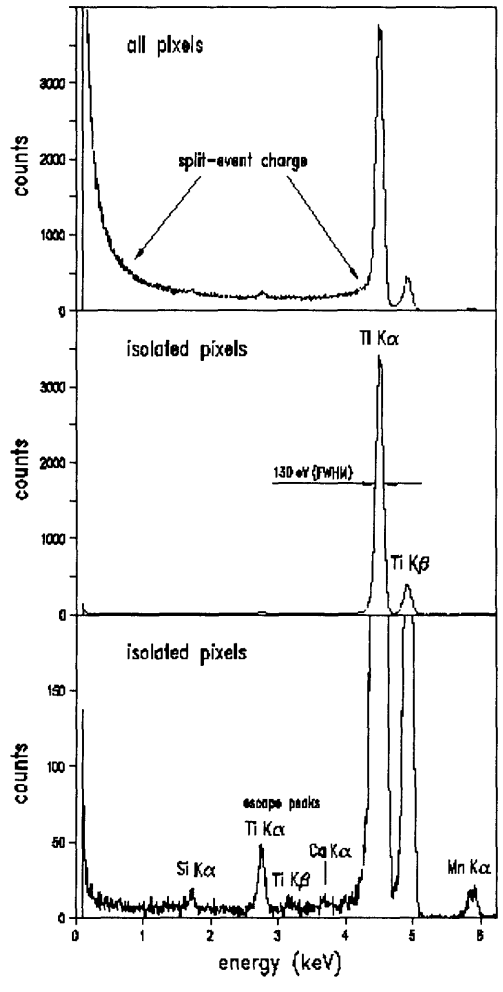

Figure 5-17. CCD energy spectrum taken with titanium fluorescence X-rays.

6 The pion

This chapter discusses the 'evolution' of the pi-meson or pion from its theoretical beginnings over sixty years ago, up to the present day, where meson physics plays an important role in the study of nuclear structure. Prediction of the pion is discussed followed by its subsequent discovery. Energetics of pion production are presented, followed by methods of pion mass measurement and modes of decay. The pion mass, combined with the muon mass and the muon momentum in pion decay at rest, currently provides the best method of setting the upper limit of the muon-neutrino mass. Finally, the relationship between the pion mass and the mass of the muon-neutrino is presented.

6.1 Prediction of the pion

With the development of relativistic quantum theory by Dirac in 1928, the electromagnetic force between charged particles had been understood on the basis of electromagnetic potentials and fields describing an exchange of photons. The question existed as to whether there was a potential that would describe an exchange of particles that gave rise to the short-range nuclear or strong interaction between nucleons. In 1935 the Japanese physicist, Hideki Yukawa, attempted to find this potential and suggested a hypothetical particle, which he named a meson (meaning middle) with a mass between that of the electron and proton, that could act as the mediator of the strong nuclear force [60].

This 'exchange model' is based upon the creation of a virtual particle, as the force mediator, which is exchanged between interacting particles, i.e. the nucleons. For conservation of energy to be maintained the particle may exist for a maximum time t, as specified by the uncertainty relationship

$$t = \frac{\hbar}{E} = \frac{\hbar}{mc^2} \quad , \qquad 6\text{-}1$$

where $\hbar$ is Planck's constant/2π and E is the rest-mass energy. Assuming the particle is travelling at close to the speed of light, c, the maximum distance, r, the virtual particle can travel in time t is given by

$$r = ct = \frac{\hbar c}{mc^2} \quad . \qquad 6\text{-}2$$

By inserting the values for the constants, measuring the particle mass in MeV/c^2 and the range in fm (10^{-15} m) this equation can be rewritten as

$$r \approx \frac{200MeV.fm}{mc^2}\ , \qquad 6\text{-}3$$

which provides a convenient relationship between the mass of the exchanged particle and its range. Thus for a range of ~1.5 fm, known from the nuclear size and over which the strong interaction has effect, a meson mass of ~130 MeV/c^2, or about 250 times more massive than the electron, is expected.

Photons have zero rest mass (and thus infinite range) and it is clear that the electromagnetic equations used to describe the photon exchange field will not work for the suggested nuclear field. If, as we assumed earlier, the exchange particles are travelling at near to the speed of light, then the non-relativistic Schrödinger equation is not suitable either.

In relativistic mechanics, the total energy, momentum and particle rest mass, are related by

$$E^2 = p^2c^2 + m^2c^4\ . \qquad 6\text{-}4$$

If we replace the energy, E, and the momentum, p, by their quantum mechanical operators, $i\hbar\partial/\partial t$ and $-i\hbar\nabla$ respectively (operating on ϕ, the wave function), then we obtain

$$-\hbar^2 \frac{\partial^2\phi}{\partial t^2} = -c^2\hbar^2\nabla^2\phi + m^2c^4\phi\ . \qquad 6\text{-}5$$

Re-arranging and cancelling gives

$$\left(\nabla^2 - \frac{1}{c^2}\frac{\partial^2}{\partial t^2}\right)\phi = \frac{m^2c^2}{\hbar^2}\phi \qquad 6\text{-}6$$

which is the Klein-Gordon relativistic wave equation. If m=0, as for the photon, this reduces to the more familiar electromagnetic wave equation.

Time-independent solutions to this equation have the form

$$\phi = g\frac{e^{-kr}}{r}\,, \qquad 6\text{-}7$$

where g is a coupling constant, $k = mc/\hbar$ and r is the range of the force. This can be compared to the potential for the Coulomb field of an electron, which has the form

$$U = -\frac{e}{4\pi\varepsilon_0 r} \qquad 6\text{-}8$$

where e is the electronic charge and r is the range of the force. The Coulomb interaction between two like-charged particles is

$$U' = \frac{e^2}{4\pi\varepsilon_0 r} \qquad 6\text{-}9$$

and by analogy, the nuclear interaction between two nucleons is given by

$$\phi' = g^2\frac{e^{-kr}}{r}\,. \qquad 6\text{-}10$$

From this analysis, Yukawa estimated the range of the nuclear force to be $1/k = \hbar/mc$, exactly that obtained in Eq. 6-2 from the uncertainty principle. A more detailed treatment of this analysis can be found in [61, 62]. The proposal of this meson field particle by Yukawa was a purely theoretical concept, with no experimental evidence at the time that such a particle existed.

6.2 Discovery of the pion

At the time of Yukawa's proposal, accelerators were not powerful enough to generate particles of this mass-energy. Searches for mesons were limited to cosmic ray detection methods using cloud chambers and photographic plates taken to high altitude. In the early 1930s, Anderson and Neddermeyer, using a cloud chamber, had detected traces of particles, which they believed to be high-energy electrons.

Then, in 1936, just one year after Yukawa's prediction and after careful analysis of the tracks, they demonstrated that what they had observed was actually a new particle, with a mass between that of the electron and the proton [63]. The new 'meson' discovered by

Anderson and Neddermeyer was quickly assumed to be Yukawa's proposed mediator of the strong nuclear force. This assumption was reinforced when photographic evidence was published which appeared to show the cosmic ray mesons decaying into electrons, in accordance with Yukawa's proposal that his particle was also responsible for beta-decay in the form of a two-stage process. Instead of a neutron emitting an electron and an antineutrino, as it changed into a proton, as Fermi had suggested, Yukawa proposed that the neutron began by emitting a field particle (his meson) as it changed into a proton. The meson then decays rapidly into an electron and an antineutrino, producing the same final result.

The acceptance of the Anderson and Neddermeyer cosmic ray meson as the predicted Yukawa particle persisted for nearly a decade until work by Conversi, Pancini and Piccione in 1945 [64] showed that this was not the case. They demonstrated that the range of the particle in solid matter was too great for one that should be affected by strong nuclear forces. Then, in 1947, C.F. Powell and his team at Bristol University [65] produced photographic evidence showing a heavier particle decaying into a lighter one. This new, heavier particle fulfilled the requirements of Yukawa's prediction and it soon became clear that the decay product of this meson was in fact the muon particle that had been discovered by Anderson and Neddermeyer in 1936.

Yukawa's field particle, predicted in 1935 and discovered in 1947 by Powell is now known as the π–meson or pion, while the lighter particle is not a meson at all but an elementary particle of the lepton family, the muon. The muon then decays into an electron and an antineutrino (and a muon neutrino), in line with Yukawa's prediction.

The π-mesons discovered by Powell are the charged pions. In 1950, the third variety of pion, the neutral pion was discovered by a team working at M.I.T. This completed the family of π-mesons which are π^+, π^- and π^0 with charges of $+e$, $-e$ and zero respectively.

6.3 Pion production

Only a year after Powell's discovery of the pion using cosmic ray techniques, particle accelerators passed the threshold required for the production of mesons. This allowed the properties of these particles to be studied in detail in the laboratory for the first time. The first mesons to be produced artificially were in fact π-mesons or pions using the 184-inch synchro-cyclotron at the University of California, Berkley [66]. Using 380 MeV alpha

particles, Gardner and Lattes bombarded a carbon target and produced mesons and other particles.

Pion production at modern particle accelerators or meson factories is usually achieved by bombarding either a carbon or beryllium target with protons. The basic nucleon-nucleon reactions are

$$p + p \Rightarrow p + p + \pi^0 \qquad \text{6-11a}$$

$$p + p \Rightarrow p + n + \pi^+ \qquad \text{6-11b}$$

$$p + n \Rightarrow p + p + \pi^- \qquad \text{6-11c}$$

$$p + n \Rightarrow p + n + \pi^0 \qquad \text{6-11d}$$

From these reactions it may be tempting to think that the bombarding proton need only posses enough kinetic energy equivalent to the mass of produced pion. However, because of conservation of momentum this is not the case. It is obvious that the initial system has kinetic energy from the bombarding particle and if this were just equal to the rest mass of the pion, it implies that the products of the reaction would all be produced at rest. If this were true momentum would not be conserved. The particles after the reaction must have momentum, therefore the kinetic energy of the initial system must be greater than the mass-equivalence of the pion. We can determine the minimum, or threshold, kinetic energy for the reaction to occur by applying conservation of energy and momentum to the reaction.

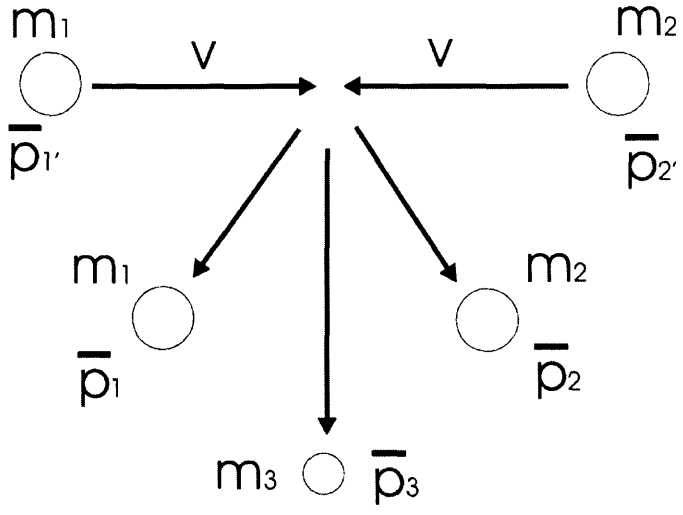

Figure 6-1. Particle reaction analogous to eqs. 6-11, in the centre-of-mass system. After the collision the reaction products are all at rest in this frame of reference at the threshold.

Referring to figure 6-1, which shows two particles colliding in the centre-of-mass (or zero-momentum) frame of reference, in four-vector notation we have

$$(\bar{p}'_1+\bar{p}'_2)^2 = (\bar{p}_1 + \bar{p}_2 + \bar{p}_3)^2 \qquad 6\text{-}12$$

where $\bar{p}_*$ are the four-momenta of the particles shown in figure 6-1. Since four-vectors are invariant between different frames of reference, we can write

$$E_{cm} = \sqrt{(m_1^2 + m_2^2 + 2E_{1lab}m_2)} = m_1 + m_2 + m_3\,, \qquad 6\text{-}13$$

where E_{cm} is the total centre-of-mass system energy, c has been set equal to 1, m_* is the rest mass of each particle and E_{1lab} is the total energy of the bombarding proton in the laboratory frame of reference, given by

$$E_{1lab} = T_1 + m'_1\,, \qquad 6\text{-}14$$

where T_1 is the kinetic energy, again with c set to 1. We can now evaluate eq. 6-13 to find E_{1lab}. Taking eq. 6-11a as an example and substituting for the masses of the proton and the neutral pion ($m_p \sim 938$ MeV/c^2, $m_{\pi 0} \sim 135$ MeV/c^2), we get

$$E_{1lab} \sim 1218 \text{ MeV}\,. \qquad 6\text{-}15$$

Using eq. 6-14, we then obtain

$$T_1 \sim 280 \text{ MeV} \qquad 6\text{-}16$$

as the threshold kinetic energy of the bombarding proton for pion production to occur. At this energy the probability or cross-section for pion production is quite small but rises sharply to a maximum at around 1 GeV. This is the reason most meson factories, such as the 590 MeV cyclotron at the Paul Scherrer Institute in Switzerland, produce protons in the energy range 0.5-0.8 MeV.

6.4 Pion mass

6.4.1 Early measurements

Yukawa's original prediction of the pion mass (~250 m_e) had been the guideline for the search for the pion itself. As soon as pion production using accelerators began, accurate pion mass measurements were attempted. Gardner and Lattes [66] used magnetic deflection to direct negative mesons onto a stack of photographic plates (Figure 6-2). Measurements of the point and angle of incidence of the particle track in the photographic plates can be used to determine the radius of curvature of the meson track. Combined with the known magnetic field, the charge-to-mass of the particle can be determined. Gardner and Lattes concluded, from the measurement of 49 separate tracks, a negatively charged pion mass of 313±16 electron masses, or ~160 MeV/c^2. This method was developed further during the late 1940s and early 1950s with pion mass measurements of 276±6 m_e reported [68]. Later improvements, with magnetic deflection of both negative and positive particles and using scattered protons from the main beam, enabled the uncertainty in the magnetic field strength to be eliminated, and pion mass measurements of π- = 276.1±1.3 m_e and π+ = 277.4±1.1 m_e (~140 MeV/c^2) were made [69].

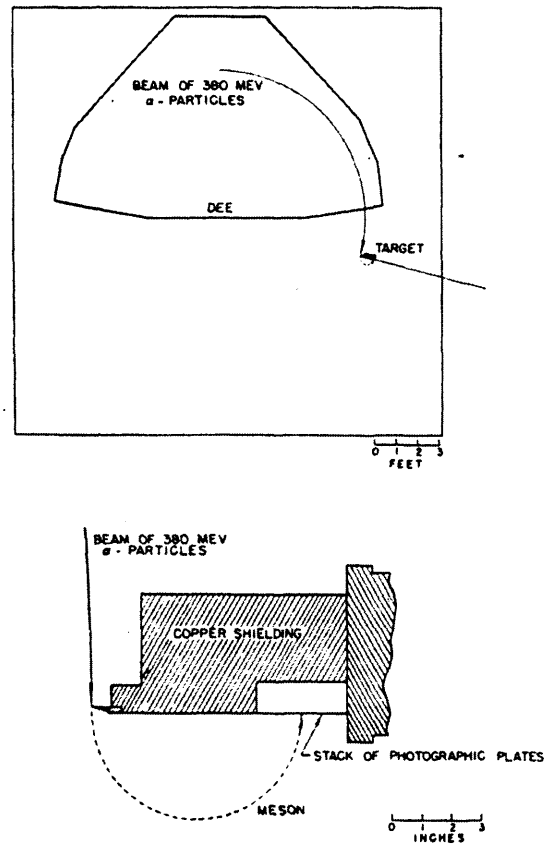

Figure 6-2. Pion mass measurement by magnetic deflection. (After Gardner & Lattes [66]).

6.4.2 Pionic atoms

Even before Powell's discovery of the pion in 1947, the existence of mesic atoms had been predicted [70]. Today, these form a subset of what are known as exotic atoms (see chapter 1), atoms where one or more of the atomic electrons are replaced by an alternative, negatively charged particle such as a (negative) pion. It was quickly realised that studies of mesic X-rays, X-rays produced during the decay of mesic atoms, could be used to provide accurate measurements of the meson mass.

Since the reduced mass of the system is proportional to the energy of these X-ray transitions, as given by

$$E_\pi = m_r F_\pi(n,l,j)\,, \qquad 6\text{-}17$$

where m_r is the reduced mass of the system, n is the primary quantum number, l is the angular momentum quantum number, j is the total angular momentum quantum number and F is given by solution of the Klein-Gordon equation (with QED corrections) for a pionic atom, measurement of the emitted X-ray energies can yield a value for the mass of the orbiting negatively charged particle.

Early measurements of pionic X-rays began with NaI detectors [71], which were quickly refined to use the critical absorption edge technique. In this method, different absorbers of a known element and concentration are inserted between the source of pionic X-rays and the detector. The concentration of the absorber is adjusted so that the X-rays, of an energy just below its K-absorption edge, are transmitted much more intensely than X-rays with energies just above the K-edge. Discontinuities in the intensity transmission between absorbers with adjacent atomic numbers (e.g. Z=58, Z=59) indicate that the pionic X-ray energy lies between these K-edge energies. In this way, Stearns et al [72] reported limits on the negatively charged pion mass of 272.2 $m_e \leq m_{\pi^-} \leq$ 273.6 m_e, a precision of ~±0.25%.

Crystal diffraction techniques were also considered at this time but the very low efficiencies of crystal spectrometers and the low intensity pion beams of the day made the method unfeasible before the 1960s. Using a bent crystal spectrometer, Shafer measured the energies of the 4f-3d transitions in pionic calcium and titanium [73] and obtained a value of m_{π^-} = 139.577±0.013 MeV/c^2, a precision of better than ±100 ppm. Shortly after, Booth et al [74] corroborated this value with a measurement of the positive pion mass to similar precision.

Since then, the pion mass has been re-measured several times using this technique and with increased precision [75, 76, 77] with the most precise value to date being obtained by measuring the 4f-3d transition in pionic magnesium, to the level of 3 ppm [78]. The measured line width of the 4f-3d transition was approximately 20% broader than expected and this was attributed to different K-shell electronic configurations. Two possible pion mass values were proposed, based upon one or two remaining K-shell electrons. Originally the one K-shell electron solution was assumed but a re-analysis [79] suggests the two K-shell electron configuration is more prevalent and this now provides the currently accepted charged pion mass value of 139.56995±0.00035 MeV/c^2 [80]. Two recent independent experiments [81, 82], to measure the 5-4 transition in pionic nitrogen, corroborate this re-analysis. Figure 6-3 summarises the pion mass measurements made since 1967.

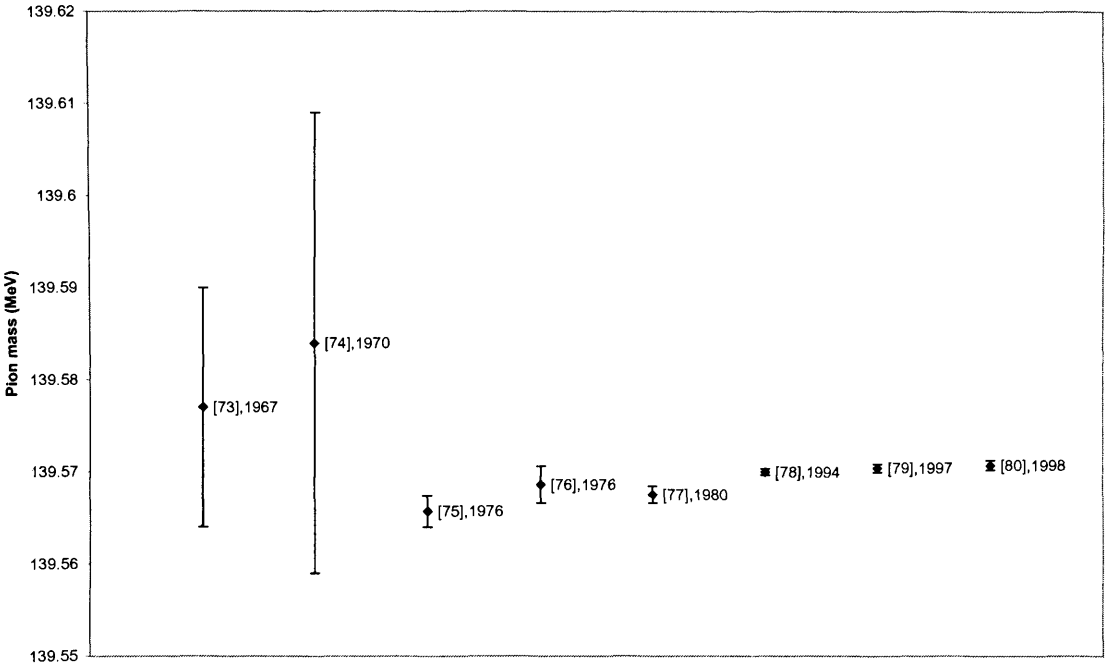

Figure 6-3. Pion mass measurements and uncertainties.

6.5 Pion decay (muon production)

Pion decay was initially observed by Anderson and Neddermeyer (although not recognised) when they proposed the muon as Yukawa's predicted π-meson (section 6.2). The charged pions decay by the weak interaction into leptons and have lifetimes of order 2.6 x 10^{-8} seconds [80]. The decay can be characterised by the following equations [61]:

$$\pi^- \Rightarrow \mu^- + \overline{\nu}_\mu \qquad \pi^+ \Rightarrow \mu^+ + \nu_\mu \qquad (\sim 100\%) \qquad 6\text{-}18a$$

$$\pi^- \Rightarrow e^- + \overline{\nu}_e \qquad \pi^+ \Rightarrow e^+ + \nu_e \qquad (1.23 \times 10^{-4}\%) \qquad 6\text{-}18b$$

$$\pi^- \Rightarrow \mu^- + \overline{\nu}_\mu + \gamma \qquad \pi^+ \Rightarrow \mu^+ + \nu_\mu + \gamma \qquad (1.24 \times 10^{-4}\%) \qquad 6\text{-}18c$$

$$\pi^- \Rightarrow e^- + \overline{\nu}_e + \gamma \qquad \pi^+ \Rightarrow e^+ + \nu_e + \gamma \qquad (5.6 \times 10^{-8}\%) \qquad 6\text{-}18d$$

$$\pi^- \Rightarrow e^- + \overline{\nu}_e + \pi^0 \qquad \pi^+ \Rightarrow e^+ + \nu_e + \pi^0 \qquad (1.03 \times 10^{-8}\%) \qquad 6\text{-}18e$$

Conservation of lepton number, where muon and electron type leptons are conserved separately, ensure that pion decay into an electron and a muon neutrino, for example, does not occur. The branching ratios, given as a percentage, show that pion decay into a muon and muon-neutrino is far more likely than into an electron and its corresponding neutrino.

The neutral pion decays via the electromagnetic process (eq. 6-19) and consequently has a much shorter lifetime than the charged pions, of order 2×10^{-16} seconds.

$$\pi^0 \Rightarrow \gamma + \gamma \qquad 6\text{-}19$$

6.6 Muon neutrino mass

Measurement of the muon momentum resulting from pion decay at rest, has been used for more than forty years to investigate the muon neutrino mass [83, 84, 85, 86, 87, 88, 89]. From the decay of the positive pion,

$$\pi^+ \Rightarrow \mu^+ + \nu_\mu \ , \qquad 6\text{-}20$$

we can write the relativistic equations for energy and momentum conservation as follows

$$E_{\pi+} = E_{\mu+} + E_{\nu\mu} \qquad 6\text{-}21a$$

$$p_{\pi+} = p_{\mu+} + p_{\nu\mu} \ , \qquad 6\text{-}21b$$

where E is related to p and m by

$$E = \left(p^2c^2 + m^2c^4\right)^{\frac{1}{2}} \ . \qquad 6\text{-}22$$

Using the theory developed in [90], we can extract from these conservation equations an expression for the mass of the muon neutrino. Since the pion is at rest, we obtain (from Eq. 6-21)

$$E_{\mu+} + E_{\nu\mu} = m_{\pi+}c^2 \qquad \text{6-23a}$$

$$p_{\mu+} = -p_{\nu\mu} \ . \qquad \text{6-23b}$$

Squaring Eq. 6-23b and multiplying by c^2 gives

$$p_{\mu+}^2 c^2 = p_{\nu\mu}^2 c^2 \ . \qquad \text{6-24}$$

From Eq. 6-22

$$p_{\mu+}^2 c^2 = E_{\mu+}^2 - m_{\mu+}^2 c^4 \qquad \text{6-25a}$$

$$p_{\nu\mu}^2 c^2 = E_{\nu\mu}^2 - m_{\nu\mu}^2 c^4 \qquad \text{6-25b}$$

and using Eq. 6-24 gives

$$E_{\mu+}^2 - m_{\mu+}^2 c^4 = E_{\nu\mu}^2 - m_{\nu\mu}^2 c^4 \qquad \text{6-26}$$

or

$$E_{\mu+}^2 - E_{\nu\mu}^2 = \left(E_{\mu+} + E_{\nu\mu}\right)\cdot\left(E_{\mu+} - E_{\nu\mu}\right) = \left(m_{\mu+}^2 - m_{\nu\mu}^2\right)\cdot c^4 \ . \qquad \text{6-27}$$

If we now divide Eq. 6-27 by Eq. 6-23a and then add Eq. 6-23a to the result, we obtain

$$E_{\mu+} = \frac{\left(m_{\pi+}^2 + m_{\mu+}^2 - m_{\nu\mu}^2\right)\cdot c^2}{2m_{\pi+}} \ . \qquad \text{6-28}$$

Using the relation 6-22 and setting the speed of light, c, equal to 1 gives

$$\left(p_{\mu+}^2 + m_{\mu+}^2\right)^{\frac{1}{2}} = \frac{\left(m_{\pi+}^2 + m_{\mu+}^2 - m_{\nu\mu}^2\right)}{2m_{\pi+}} \ . \qquad \text{6-29}$$

Finally, re-arranging, and assuming CPT (Charge/Parity/Time) invariance for the charged pion mass ($m_{\pi^-} = m_{\pi^+}$), we obtain for the squared muon-neutrino mass

$$m_{\nu\mu}^2 = m_{\pi-}^2 + m_{\mu+}^2 - 2m_{\pi-}\left(p_{\mu+}^2 + m_{\mu+}^2\right)^{\frac{1}{2}} . \qquad 6\text{-}30$$

In this relationship, the squared muon-neutrino mass is obtained by the subtraction of one relatively large number from another, making a precise determination of the (very small) muon-neutrino mass unreliable. What is possible, by accurate measurement of the charged pion mass, the muon mass and the momentum of the muon in the pion decay (at rest), is to place an upper limit on the mass of the muon-neutrino. From [89] the uncertainty in the squared muon-neutrino mass in Eq. 6-30 is given by

$$\Delta\left(m_{\nu\mu}^2\right) = \left[\left(\eta_1 \Delta m_{\pi-}\right)^2 + \left(\eta_2 \Delta m_{\mu+}\right)^2 + \left(\eta_3 \Delta p_{\mu+}\right)^2\right]^{\frac{1}{2}} , \qquad 6\text{-}31$$

where η_1, η_2 and η_3 are the partial derivatives $\partial(m_{\nu\mu}{}^2/\partial m_{\pi^-})$, $\partial(m_{\nu\mu}{}^2/\partial m_{\mu+})$ and $\partial(m_{\nu\mu}{}^2/\partial p_{\mu+})$. The current values and their uncertainties for the three quantities on the right hand side of Eq. 6-30, taken from [80] (m_{π^-}, $m_{\mu+}$) and [89] ($p_{\mu+}$), are as follows:

$$m_{\pi^-} = 139.569\,95 \pm 0.00035 \text{ MeV/c}^2 \qquad 6\text{-}32a$$

$$m_{\mu+} = 105.658\,389 \pm 0.000034 \text{ MeV/c}^2 \qquad 6\text{-}32b$$

$$p_{\mu+} = 29.79200 \pm 0.00011 \text{ MeV/c} \qquad 6\text{-}32c$$

Using these quantities, Eq. 6-30 and 6-31 can be evaluated to give a value for the squared muon-neutrino mass of

$$(m_{\nu\mu})^2 = -0.016 \pm 0.023 \text{ (MeV/c}^2)^2 . \qquad 6\text{-}33$$

Using the Bayesian method[1] described in [80] (probability for a negative muon-neutrino mass set to zero), we obtain from Eq. 6-33 an upper limit for the muon-neutrino mass of

$$m_{\nu\mu} < 0.17 \text{ MeV/c}^2 \quad \text{(Confidence Limit 90\%)} . \qquad 6\text{-}34$$

[1] The Bayesian method is appropriate since it relies upon *a priori* information. A negative muon-neutrino mass squared is unfeasible and so the information in this case is to set the probability of such a result to zero.

If the three partial derivative terms on the right hand side of Eq. 6-31 are evaluated, we find that the uncertainty in the squared muon-neutrino mass is almost completely due to the uncertainty in the charged pion mass value.

The new experiment described in this thesis aims at re-measuring the charged pion mass to the 1 ppm level. Re-calculation of Eq. 6-31, assuming the value from Eq. 6-30 is unchanged, gives

$$m_{\nu\mu} < 0.105 \text{ MeV/c}^2 \quad \text{(Confidence Limit 90\%)} . \qquad 6\text{-}35$$

Even with zero error on the pion mass, the upper limit would only be lowered to ~ 90 keV/c^2. A further improvement could be made by making a more precise measurement of the muon momentum.

7 Experimental approach

This chapter describes the experimental approach and arrangement used to make a determination of the charged pion mass by measuring characteristic X-rays from the decay of exotic atoms. It begins by describing what is necessary to achieve a pion mass measurement to the 1 ppm level and the experimental equipment and arrangement used. Beam time operation and data collection are explained and the chapter concludes with an analysis of the crystal performance and CCD stability measurements.

7.1 Introduction

As discussed in Chapter 6, the measurement of characteristic X-rays from pionic atoms has produced the most precise determination of the charged pion mass to date [91, 92]. This was achieved by measuring the pionic 4f-3d transition in solid magnesium. This line has an energy of 26.9 keV and was measured using a Du Mond type spectrometer with an instrumental resolution of 0.93 eV. A NaI/CsI phoswich detector was used at the focus of the spectrometer. From this experiment the pion mass was determined as 139.56995 ± 0.00035 MeV/c^2, a precision of 2.5 ppm.

7.2 A 1 ppm pion mass measurement

Using high precision spectroscopy of characteristic X-rays to determine the pion mass to the 1 ppm level places strict requirements on the experimental arrangement. In the experiment described in the introduction the observed line width was about 20% larger than the instrumental resolution, which was attributed to the occurrence of more than one electronic configuration of the pionic atom. Different levels of electron screening of the nuclear charge cause shifts in the pionic transition energy. For exotic atoms formed in a solid target (e.g. magnesium) electron re-filling occurs rapidly and the status of the electron shell is difficult to determine, which leads to an unknown degree of electron screening. Using gas targets with $Z \leq 10$ overcomes this problem, where complete ionisation of low Z exotic atoms has been demonstrated [12], but greatly reduces the stop rate of pions.

In pionic atoms strong interaction shifts in the energy of characteristic X-rays can also be significant. A precise determination of the pion mass using this method therefore requires the measurement of transitions that are not affected by the strong interaction. This effectively means transition levels in the intermediate part of the cascade, i.e. lower transition energies, but these transitions may then be influenced by interaction with the electron shell.

The high-resolution spectroscopy, in the few keV range necessary for a precise pion mass determination, requires the use of a Bragg crystal spectrometer. However, a calibration line at least equal in accuracy to the measurement requirement is needed. The energy of the pionic transition is directly proportional to the pion mass, so a 1 ppm energy measurement requires a calibration line with energy known to 1 ppm or better. Commonly used fluorescence lines are unsuitable due to uncertainties in their energies and large natural line widths. One possible exception is the Cu Kα line, the shape of which has been extensively studied [93]. A better alternative is to use another exotic atom transition. The only choice in this instance is a muonic atom, where the muon mass is known to 0.06 ppm [94]. It is also highly desirable to measure the calibration line simultaneously with the pionic line, to remove the requirement to mechanically shift the spectrometer between measurements. This has been identified as a major source of error in previous experiments [95].

Suitable, low Z gas targets should also be close in atomic number to ensure a similar atomic cascade during de-excitation. This leads to the choice of nitrogen and oxygen, with atomic numbers 7 and 8 respectively. As gases, they are both diatomic (again important in terms of atomic cascade) and there are a number of transitions with energies in the soft X-ray range if pionic nitrogen and muonic oxygen are selected. Possible transitions are 6-5, 5-4 and 4-3. The 6-5 transition can be rejected on the grounds of too much self-absorption in the target due to the lower energy. In pionic nitrogen, the 4-3 transition begins to exhibit strong interaction effects due to the proximity of the pion to the nucleus, which adds a large uncertainty to the transition energy. The 5-4 transition avoids these problems and has an energy of ~4 keV. With an energy difference of only ~32 eV between pionic nitrogen (5g-4f) and muonic oxygen (5g-4f) they make excellent candidates for simultaneous measurement.

Accurate interpretation of the reflections from a Bragg crystal spectrometer requires a two-dimensional position sensitive detector. X-ray sensitive CCD detectors are ideal when the X-ray energy of the transitions is in the 1 – 10 keV range. The position resolution of the detector needs to over-sample the reflected line profiles. For a particular crystal, the dispersion at the detector is determined by the size of the Rowland circle and the CCD pixel size must be small enough to ensure that adequate over-sampling is achieved.

A feasibility study [96] has already successfully demonstrated the suitability of this approach but using only Cu Kα X-rays for calibration and a smaller detector. The detector size required movement of the spectrometer between pionic nitrogen and Cu Kα line

measurements, which introduced the single largest source of error in the experiment. The new experimental arrangement described below uses muonic oxygen X-rays for calibration and a new large area CCD detector to provide simultaneous measurement of both lines of interest.

7.3 Experimental arrangement

The experiment uses the high-intensity pion beam generated at the 590 MeV proton cyclotron at the Paul Scherrer Institute (PSI). A graphite target wheel placed in the main proton beam generates positive and negative pions (see section 2.3.1), some of which decay within the target into muons. Pions are produced in the ratio of 4:1, positive to negative. Negative pions are selected using a bending magnet, which directs them into the πE5 beam line. Magnets focus the negative pions into a beam line set up for an average momentum of 107 MeV/c. An intensity of ~2.7×10^8 π^-/s is achieved for a proton beam current of 1.5 mA. The experimental apparatus is shown in figure 7-1 and comprises a cyclotron trap, a curved crystal spectrometer and CCD detector located in a cryostat.

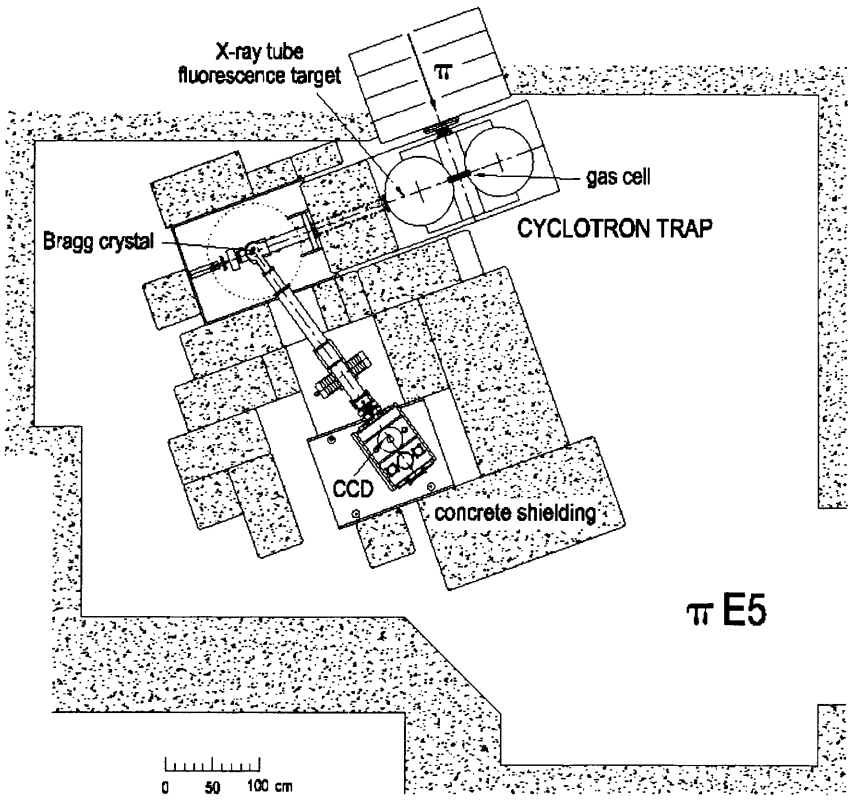

Figure 7-1. Experimental arrangement in the πE5 area at the PSI.

The neutron-induced background in close proximity to the beam-line can be overwhelming and so background reduction begins during experiment installation. This is achieved with the application of a large number of concrete blocks. Careful positioning limits detector exposure to that via the spectrometer tube only.

7.3.1 Cyclotron trap

Using a gas target to generate the pionic and muonic atoms is necessary for the advantages described in section 7.2. A major disadvantage is the greatly reduced stopping power over a solid or liquid target. To achieve any level of acceptable stop rate the gas target chamber would need to be tens of metres in length with the result that X-rays would be emitted within a very large volume and be virtually undetectable. By employing a cyclotron trap [97, 98] the long stopping distance is effectively 'wound up' by inverting the principle of a weakly focusing cyclotron. This allows particles to be captured efficiently inside a small volume at gas pressures of around 1 bar.

The cyclotron field is produced by a superconducting split-coil magnet (figure 7-2), the two halves of which are mounted in separate cryostats and embedded in a soft-iron housing that forms the evacuated deceleration chamber.

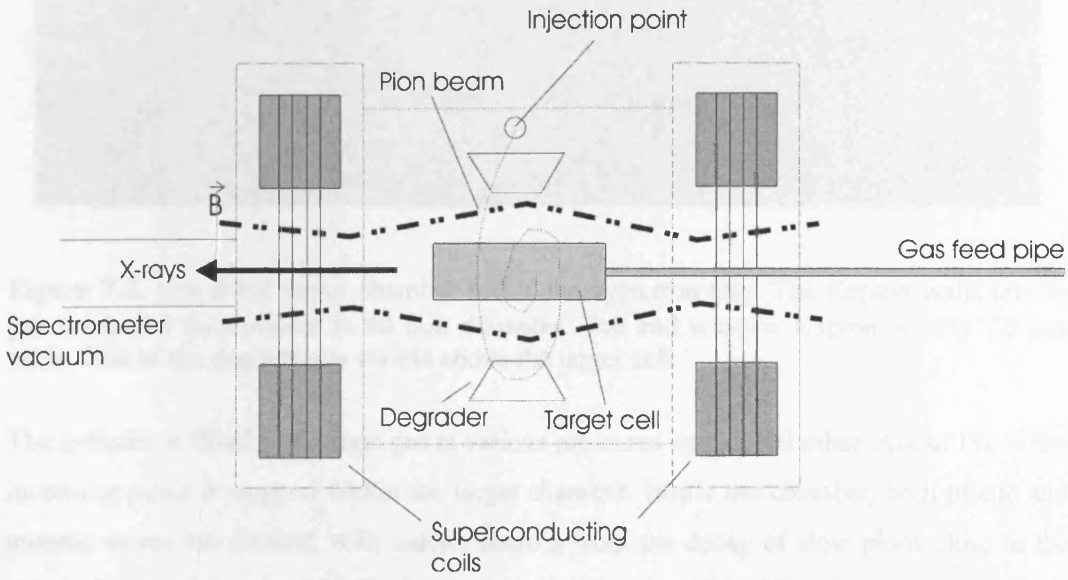

Figure 7-2. Cyclotron trap schematic diagram.

The two halves can be shifted apart by 1 m to allow entry to the interior of the chamber with access to the stop region through a warm axial bore hole. The magnet accepts pions of momentum up to 200 MeV/c with a field diameter of 290 mm. The radius of injection is

between 110 and 140 mm where a low Z moderator decelerates the pions to a momentum which prevents them from hitting the moderator for a second time. The particles then enter the deceleration volume, fitted with radial foils and wedges which produce a fast degradation of the pion momentum, within the particle's lifetime of ~2.6×10^{-8} s. At the centre of the trap is located a thin-walled Kapton chamber, cylindrical in shape with a diameter of 60 mm (figure 7-3). The window of the chamber (7.5 μm) is thin enough to avoid significant absorption of the 4 keV pionic and muonic X-rays.

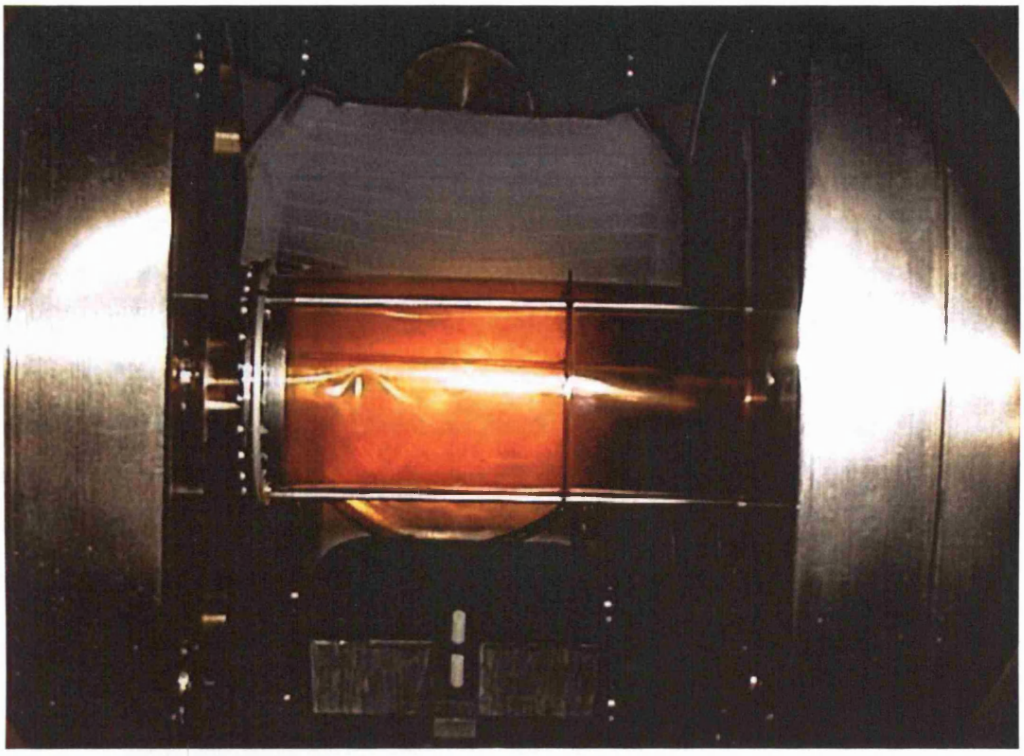

Figure 7-3. Gas filled target chamber inside the cyclotron trap. The Kapton walls are 50 μm thick and the cylinder is 60 mm diameter. The end window Kapton is only 7.5 μm thick. One of the degraders is visible above the target cell.

The cylinder is filled with target gas at various pressures up to 1400 mbar. About 1% of the incoming pions is stopped within the target chamber. Inside the chamber, both pionic and muonic atoms are formed, with muons coming from the decay of slow pions close to the target chamber (see section 6.5). A stop rate of only about 5% of the pion rate is achieved. However, these stop rates represent an increase by a factor of as much as 1000 over conventional high-volume gas target methods. X-rays from the de-excitation of the pionic and muonic atoms can leave the cyclotron trap via the ends of the target chamber, aligned axially within the bore hole.

7.4 Bragg crystal spectrometer

Connected to the bore hole of the cyclotron trap is a Bragg crystal spectrometer set up in Johann geometry (see section 3.3.1) which is used to focus characteristic X-rays emitted from the de-excitation of the exotic atoms. With this geometry it is possible to record all energies in a certain interval, determined by the width of the source (60 mm), simultaneously by using a position-sensitive detector of corresponding size. The dispersion element is a silicon wafer cut along the (110) direction, 100 mm in diameter.

The spectrometer layout is shown in figure 7-1. It comprises a stainless steel crystal housing (figure 7-4) with two stainless steel tubes, which form the arms of the spectrometer. The bore hole of the cyclotron trap is located at the end of one arm with the detector cryostat at the other. This arrangement ensures that the crystal, cyclotron trap and detector all lie on the Rowland circle. Calibration of the spectrometer dispersion is achieved by mounting the crystal on a high precision angular encoder with a measured accuracy of 0.14" over small angles. This corresponds to ~2 meV at the detector (~0.5 ppm of the πN (5g-4f) transition energy). The crystal can be independently rotated allowing the reflection to be positioned anywhere on the detector. This makes angular dispersion in terms of CCD pixels simple to determine. Crystal temperature is not controlled but monitored with three temperature sensors, which allow thermal variations of the lattice spacing to be taken into account during data analysis.

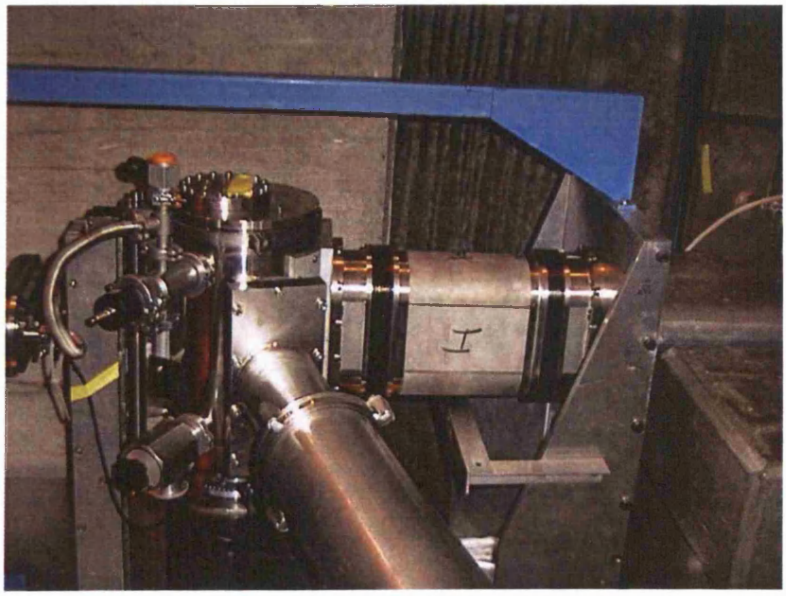

Figure 7-4. Spectrometer crystal housing.

The energies of the πN (5g-4f) and μO (5g-4f) lines differ by only ~32 eV or a change in Bragg angle of ~36' (see Table 7-1). With a Rowland circle radius of 1.5 m, this corresponds to a line separation of ~30 mm at the detector, a dispersion of ~1 eV/mm. To avoid position errors introduced by shifting the spectrometer (one of the key aims of this experiment), the detector must be at least this wide in order to measure the two lines simultaneously. Use of a spherically bent crystal improves the count rate at the detector by partially focussing the reflection in the vertical direction. For a 60 mm source and a crystal diameter of 100 mm, the image height at the detector is ~110 mm (at Bragg angles around 53°), compared to 260 mm for a flat crystal of the same dimensions (see section 3.3.2).

Changes to the crystal lattice structure at the edge of the crystal can cause poor reflection in this region and so the apparent crystal size was reduced by placing a mask with a 90 mm diameter circular aperture in front of the crystal.

From the geometry of the spectrometer it is possible to estimate the X-ray count rates which will be seen at the detector. Starting from the beam conditions described in section 7.3, figure 7-5 illustrates the estimated X-ray rates at the detector for pionic nitrogen and muonic oxygen.

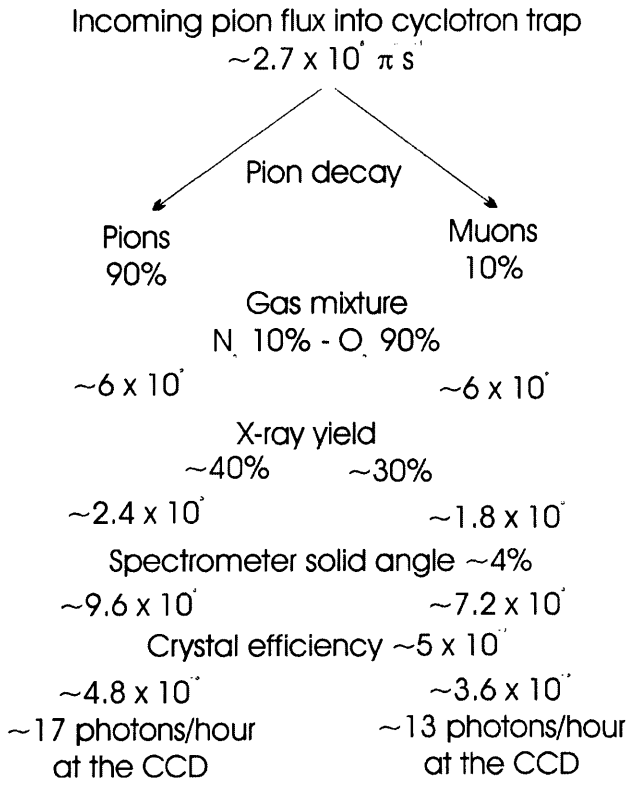

Figure 7-5. Estimated X-ray count rates.

7.5 X-ray detector

To meet the dimensional requirements of the detector discussed in section 7.4, an array of X-ray sensitive CCDs (see chapter 4) is located at the focus of the spectrometer on the Rowland circle. The array comprises six CCD22 devices arranged as two columns of three (figure 7-6). These devices are described in detail in section 4.5. Each CCD22 is mounted on a thermally isolated package, with a connection to a cold-finger for cooling.

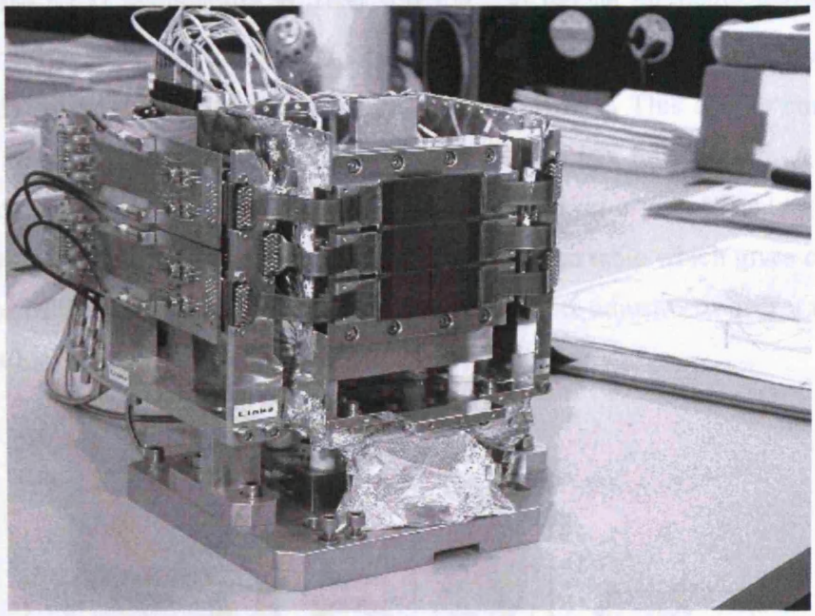

Figure 7-6. Array of CCD22 devices mounted on cold-finger assembly, prior to installation in the cryostat. The dual pre-amplifier cards are visible on the side.

Figure 7-7. CCD22 mounted on three-sides buttable package. All connections are made via the flexible, thermally isolating Kapton circuit (Photo F. Balam).

Electrical connection is provided for the clock and bias signals via a Kapton flex-circuit (figure 7-7). Each device has an image region 24 mm x 24 mm, giving a total imaging area for the array of 48 mm x 72 mm. There is a maximum gap of 500 μm between devices and they are rotationally aligned to better than 7 mrad (see section 8.2). The six CCDs are attached to an invar cold-finger and the whole assembly is mounted inside a custom built, stainless steel vacuum cryostat (figure 7-8). The cold-finger is cooled using liquid nitrogen and closed-loop temperature control using a PT100 platinum resistance thermometer maintains the CCD temperature at –100 ± 0.5 °C, to reduce thermally generated 'dark current' to negligible levels. The CCD array is wrapped in 5 μm metalised Mylar, cooled very quickly by direct connection to the liquid nitrogen feed. This acts to condense any remaining water or contaminants before the CCD surface has fully cooled. A gate valve allows disconnection of the spectrometer tube without losing cryostat vacuum. The cold-finger is mounted on a motorised, high-precision translation table which gives control over the distance of the CCD array to the Bragg crystal. Remote adjustment over a range of 95 mm is possible, to match the focal length of the crystal in use.

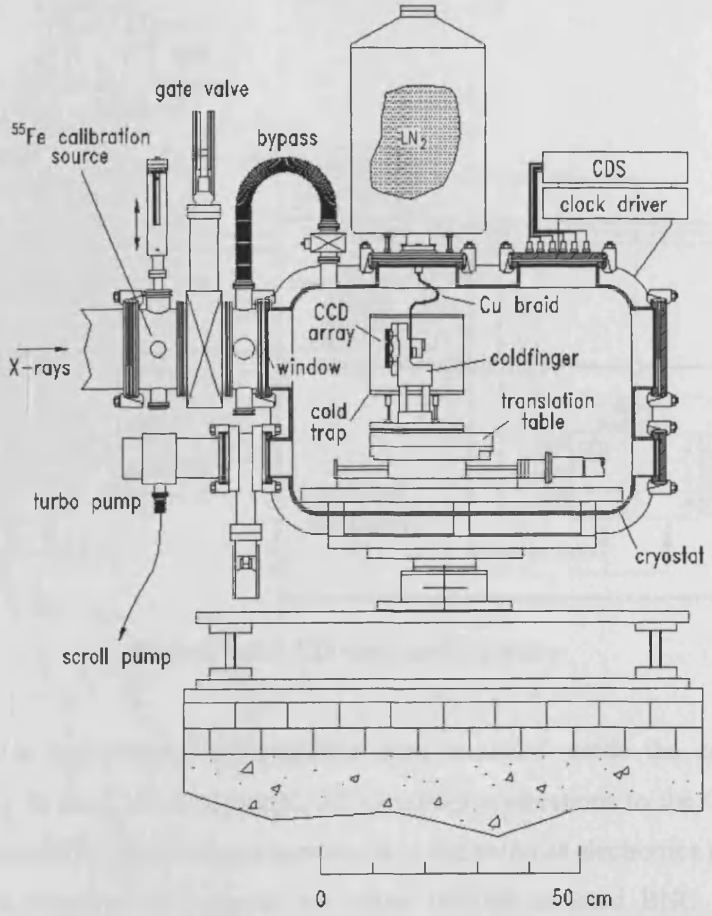

Figure 7-8. CCD cryostat.

The position perpendicular to the crystal-detector direction (transverse offset), i.e. the direction of dispersion, is controlled by a precision gauge and is reproducible to 1 μm. The vertical direction is fixed. Movement of the linear table, verification of the transverse offset and monitoring of various temperatures of the cooling system are all included in the spectrometer control system. The entrance aperture of the cryostat is covered by a 5 μm aluminized Mylar window which is protected against over-pressure by a bypass arrangement which is closed automatically whenever the spectrometer vacuum is above 10^{-3} mbar. Below this pressure, the gate valve can be opened in front of the CCD array allowing measurement of X-rays reflected from the crystal. An ^{55}Fe source is available to determine calibration and resolution at 5.9 keV and can be positioned manually in front of the CCD array when required.

7.5.1 Detector operation

The CCD array is controlled using a combination of modified commercial and custom-built electronics (figure 7-9).

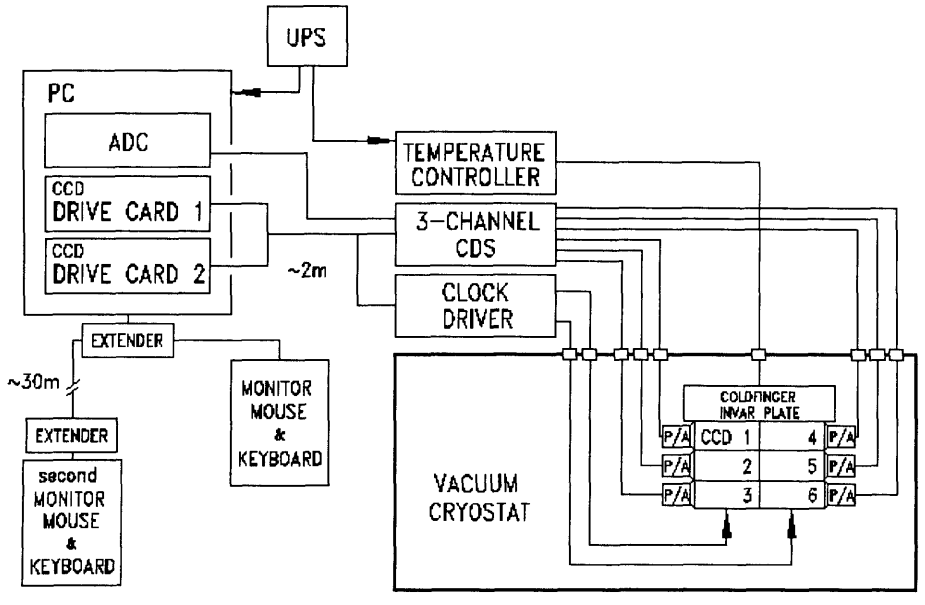

Figure 7-9. CCD control electronics.

Each CCD has a dual-channel pre-amplifier card mounted inside the cryostat, which connects directly to the CCD flex-circuit. All electrical connections to the CCD are made through the pre-amplifier card and are connected to the external electronics using hermetic connectors. The pre-amplifier outputs are taken through isolated BNC connectors to prevent ground noise coupling from the cryostat.

A separate PC expansion card supplies control signals for each column of CCDs. The clock sequences are generated using a digital signal processor, which is programmable from the host PC. This allows any clock sequence to be written, e.g. full-frame or frame-transfer, with variable timing and 50 ns resolution. The clock signals from the PC cards are routed through a clock driver box which boosts the output signals to a level where they are capable of driving three CCDs in parallel. The bias voltages are all derived using digital to analogue converters and are again software adjustable from the PC. Custom sequence programs were written which provide synchronised operation between the two columns of CCDs. Image integration followed by frame-transfer occurs at the same time for all six CCDs. The storage regions of the devices are read out, one column at a time using a multiplexed, three channel correlated double sampling (CDS) processor. The CDS processor is a custom design using a variation of the dual-slope integration method (see section 5.5.4). Figure 7-10 illustrates the basic scheme.

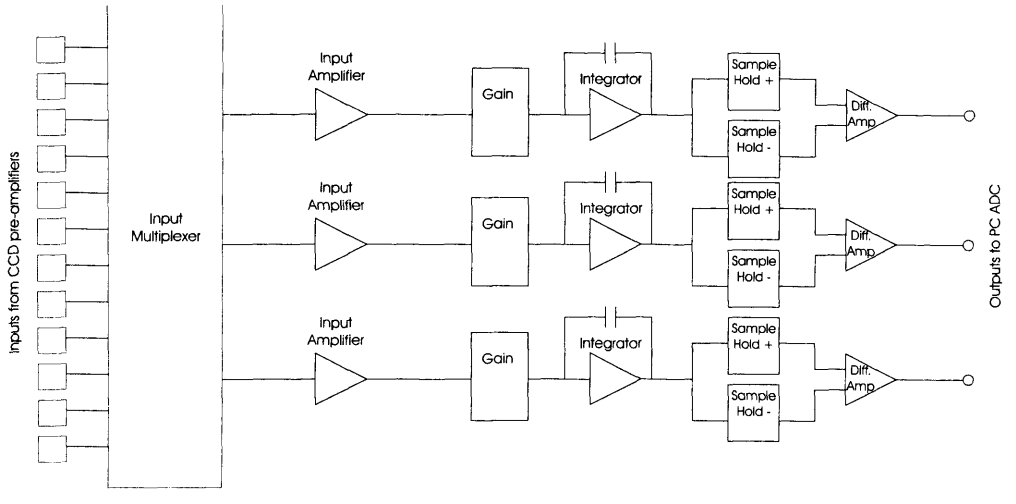

Figure 7-10. Three channel dual slope integrator.

The CDS has twelve inputs, one for each of the two output nodes of each CCD. During normal operation only one node from each CCD is used, the second is connected in case of node failure. The six operational outputs are multiplexed into the three processing channels, one column of devices at a time. Each channel has programmable gain (x2 to x16). The variation from the usual dual-slope integration method is that the integrated reset and charge (+ reset) levels are stored separately and then correlated using a final stage difference amplifier. This method has the advantage that an extra amplifier for inverting the charge level is not required, reducing the possibility of introducing gain errors. The three outputs from the CDS are then digitised using a multi-channel 12-bit, analogue to digital converter expansion card in the PC. Once the first column of CCDs has been read-out

completely, the CDS input multiplexer is switched and the second column of devices is processed and digitised. Custom sequence programs control the operation of both columns of CCDs to ensure that synchronisation is maintained. The pixel read-out rate is ~25 kpixels/s. However, since three CCDs are read-out in parallel, the read-out time for a column of CCDs is the same as for a single device, ~ 15 s. Total read-out time for the array is twice this figure, 30 s. In frame-transfer operation, the CCDs continue to image the source during read-out of the storage region and so 'lost' data only occurs during the actual frame-transfer time of ~20 ms.

The PC is powered from an un-interruptible power supply (UPS) and is also equipped with an extender unit. This allows a second monitor, mouse and keyboard to be located in the control hut, some 30 m outside the πE5 area.

Long integration times (>1 hour) are possible using cryogenic operation without thermal charge contributing significantly to the read noise. However, in the high background environment of the beam line, background events of order 20000 per CCD per hour have been detected. A CCD pixel activated by a background event is either saturated or contains an indeterminate amount of charge making it unusable for detecting an X-ray photon. With very low X-ray count-rates at the detector it is important to minimise the dead area of the CCD. This can be achieved by using a much shorter frame integration time. With integration times of order 1 minute, the number of background events per frame can be reduced to ~300, equivalent to <0.1 % of the imaging area. This has the disadvantage that the quantity of CCD data collected is increased substantially. Each CCD has 600 x 600 = 360000 pixels. Assuming 16 bits (2 bytes) per pixel, one full image from the array amounts to 4.3 Mb, corresponding to 6.2 Gb of data per day. Over a ten-week beam run, storage and back-up of this quantity of data can be difficult. Using real-time data compression, this quantity is reduced substantially. Each CCD is calibrated before use, which provides read-noise peak position and width. From this, an event threshold is determined (usually 3 or 5 standard deviations above the noise peak). Only pixels with a charge value above this threshold are stored, as a 3-byte position and 2-byte value. In comparison to raw data storage (360000 pixels/CCD/frame) there may be only 2000 active pixels per minute for a full six-CCD image. This reduces data storage requirements to 600 kb per hour or less than 15 Mb per day, a factor of >400 reduction on the raw data rate.

7.6 System operation

The run-time operation of the whole target-spectrometer-cryostat system is controlled from a separate computer. Pressure and temperature of the target chamber are continuously monitored. The crystal temperature is also monitored in several places. The crystal angle and the angle of the detector arm of the spectrometer are set remotely. Positioning to ~1" accuracy is performed using stepper motor driven mounts with fine positioning for the crystal angle achieved using piezo-actuator active feedback. In this way, the crystal angle is maintained with an accuracy of ±0.14". During calibration and alignment a fluorescence target illuminated by an X-ray tube is used in place of the target cell. The fluorescence target contains both scandium and copper, selection of which is achieved using a motor driven mount. The extensive remote control of the experimental apparatus ensures that minimum access to the beam area is required during operations, which would otherwise reduce valuable beam-time.

7.7 Beam-time operation and data collection

Data was taken continuously over a nine-week period in Spring 2000. Measurements comprised system optimisation, taking data from the target cell with different gases and mixtures, calibration data and system stability data. Figure 7-11 shows how the experimental period was organised.

Week 1	**Week 2**	**Week 3**	**Week 4**	**Week 5**
Experimental apparatus set-up	Target scan Tilt angle Cu dispersion Focus check	Cu dispersion πN/μO data	πN/μO data Calibration check	πN/μO data Calibration check
Week 6	**Week 7**	**Week 8**	**Week 9**	
πN/μO data Calibration check	πN/μO data Calibration check	πN dispersion	πNe resolution	

Figure 7-11. Experimental time line and measurement divisions during the nine-week beam run in Spring 2000.

Each of the different experimental operations is described in the following sections. However, prior to any data collection operation being performed the experimental apparatus was configured. This includes setting the appropriate Bragg angle, crystal tilt angle, target conditions and CCD operating parameters. Table 7-1 lists the Bragg angles and transition energies of all lines used during the experiment. The configuration used for each measurement type is given in the relevant section.

7.7.1 Target chamber optimisation

The cylindrical, gas-filled target was optimised for both gas mixture and position within the cyclotron trap.

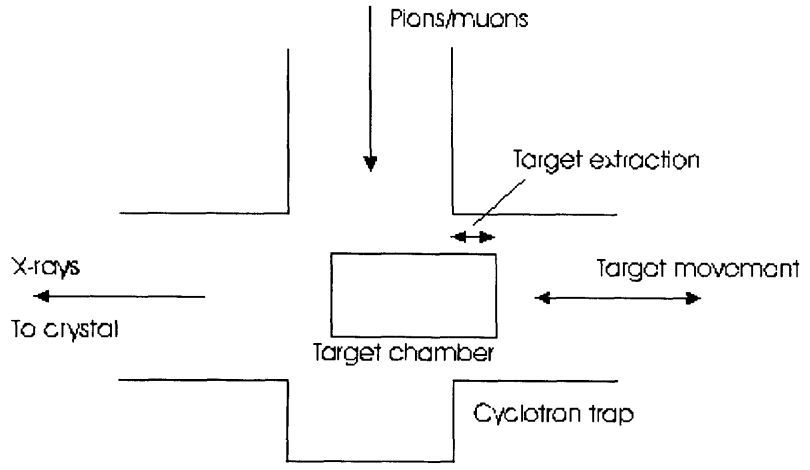

Figure 7-12. Schematic showing target cell location within the bore of the cyclotron trap. X-ray production is optimised by moving the target in the direction of the arrow.

The location of the target chamber is shown schematically in figure 7-12 and can be moved in the direction of the arrow. The further the target is inserted into the bore of the cyclotron trap, the larger the stop volume for pions and muons. However, the larger the stop volume, the more pionic and muonic X-rays will be absorbed within the target gas before they can escape from the chamber. Since only part of the target volume is actually involved in X-ray production, the optimum position is when X-ray absorption in the target gas is minimised without cutting into the stop distribution. This configuration was determined by filling the target chamber with neon at 1 bar and measuring the X-ray count rate against target extraction. X-rays from the pionic neon 3-2 transition at ~40 keV were measured using a germanium detector. At this energy there is no self-absorption within the target gas and the X-ray count rate depends solely upon stop volume. The results are shown in figure 7-13 and indicate that the target can be extracted by up to 60 mm before a reduction in count rate is detected. Measurement of the pionic neon 3-2 transition was also used to optimise parameters of the πE5 beam-line (e.g. focusing using quadropole magnets) and the degrader fitted inside the cyclotron trap.

For the main experimental data of pionic nitrogen and muonic oxygen, the nitrogen/oxygen gas mixture ratio was selected simply as the inverse of the ratio of muons (from decayed pions) to pions, i.e. 90% oxygen, 10% nitrogen. Target gas pressure was kept between 1000 mbar and 1400 mbar, optimised for count rate in the previous feasibility study.

Transition	Energy (eV)	Relative intensity	Bragg angle (θ_B)	Index of refraction correction ($\Delta\theta_B$)	Experimental Bragg angle ($\theta_B + \Delta\theta_B$)
π^{14}N(5g-4f) electron screening	4055.38078 + 0.494(1K e-)		52°45'36.00"	12.94"	52°45'48.94"
(5f-4d)	4057.69371				
(5d-4p) ε_{4p} = +720±180 meV	4061.948 QED 4062.668				
π^{15}N(5g-4f)	4058.23991		52°42'24.95"	12.91"	52°42'37.86"
μ^{16}O($5g_{7/2}$-$4f_{7/2}$)	4023.50871	1			
($5g_{9/2}$-$4f_{7/2}$) electron screening	4023.75253 + 1.050(1K e-)	35	53°21'23.67"	13.22"	53°21'36.89"
($5g_{7/2}$-$4f_{5/2}$)	4024.30301	27			
($5f_{5/2}$-$4d_{5/2}$)	4025.39943	1			
($5f_{7/2}$-$4d_{5/2}$)	4025.80616	20			
($5f_{5/2}$-$4d_{3/2}$)	4026.99152	14			
μ^{18}O($5g_{9/2}$-$4f_{7/2}$)	4026.67	35			
π^{20}Ne(6h-5g)	4509.89361		45°42'53.81"	10.08	45°43'03.89"
(6g-5f)	4511.86286				
π^{22}Ne(6h-5g)	4512.94834		45°40'30.71"	10.07	45°40'40.78"
Cu $K\alpha_{22}$	8027.993(5)		53°32'39.13"	3.30	53°32'42.43"
Cu $K\alpha_{12}$	8045.367(22)		53°22'37.38"	3.28	53°22'40.66"
Cu $K\alpha_{11}$	8047.837(2)		53°21'12.23"	3.27	53°21'15.50"

Table 7-1. Bragg angles and transition energies of experimental lines. The energies are determined from QED [99] and the Bragg angles are calculated using XOP2 [105].

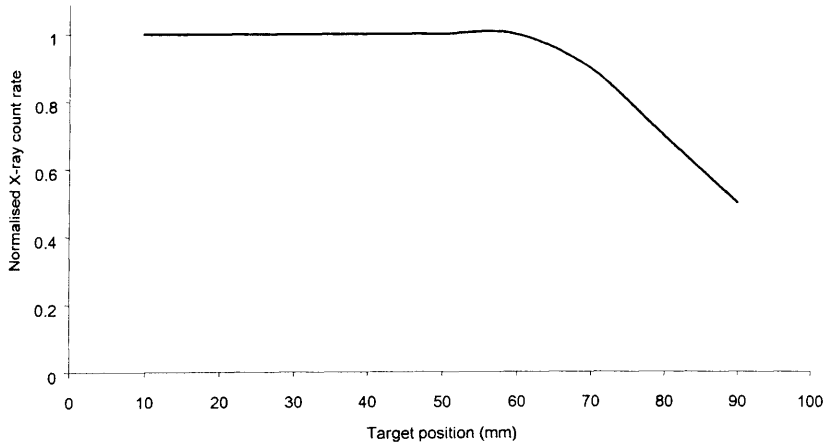

Figure 7-13. X-ray count rate plotted as a function of target extraction.

7.7.2 Spectrometer optimisation

The crystal was not only mounted on a high precision angular encoder but could also be tilted remotely in the vertical direction. Spectrometer optimisation consisted of two operations. The first was to determine the tilt angle that provided a balanced reflection at the detector i.e. with a similar proportion of X-rays on the top and bottom CCDs of a column. The target cylinder was filled with nitrogen (using nitrogen alone provides increased X-ray count rate – see section 7.7.1) at a pressure of 1000 mbar. The cylinder was extracted by 60 mm from the cyclotron trap and exposed to the pion beam. With the pionic nitrogen 5g-4f line reflected onto one column of CCDs, the number of X-rays detected by the top (CCD 1) and bottom (CCD 3) CCDs in the column was recorded for different crystal tilt angles. The results are plotted in figure 7-14. A tilt angle of ~0.35 degrees gives an even distribution of X-rays.

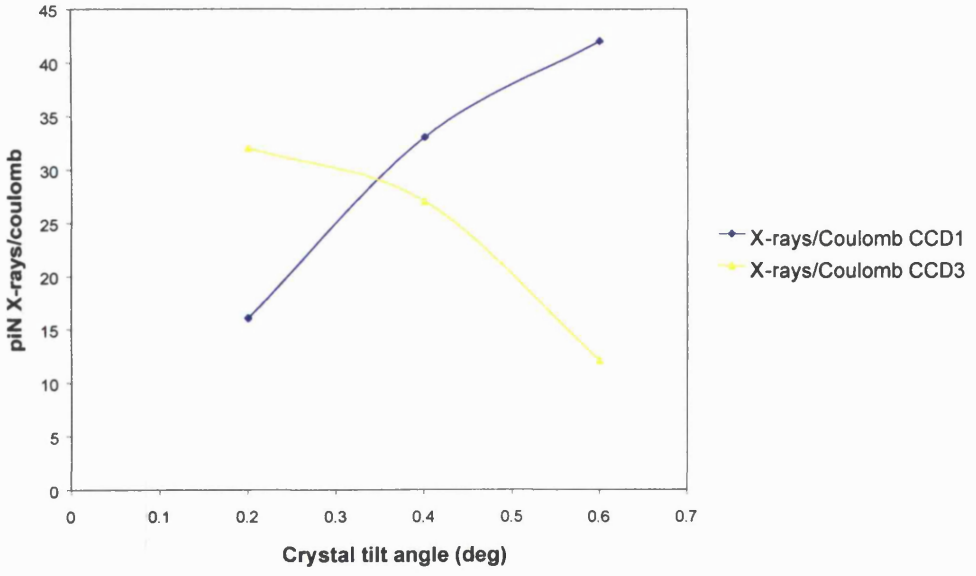

Figure 7-14. Crystal tilt-angle scan results.

The second operation was a target scan. Since the target is finite in size, measurements were taken to determine where the edges of the target occurred to ensure that the spectrometer was looking at the optimal, central region. Also, the visible target end is supported by an aluminium honeycomb structure (figure 7-15) and the target scan (figure 7-16) provided information to ensure that the crystal was not aligned with a possible vertical structure within this honeycomb, which would reduce the X-ray count rate.

Figure 7-15. Honeycomb support structure on the end of the target cell.

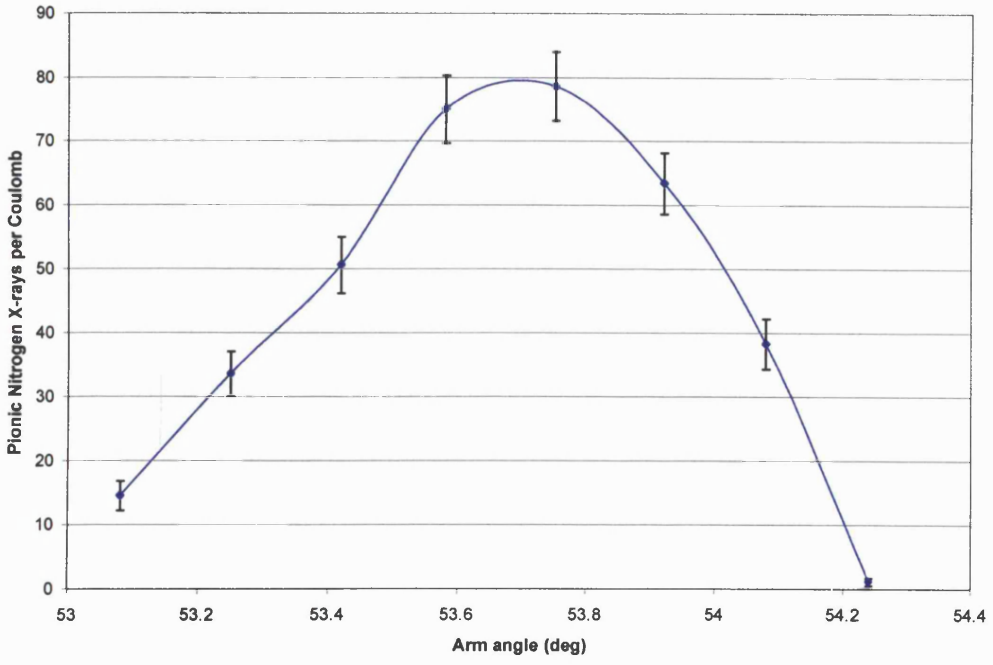

Figure 7-16. Target scan results. Plot of count rate against spectrometer arm angle. Peak count rate is obtained at an arm angle of 53.7°.

7.7.3 Exotic atom X-ray measurements

Three different exotic atom measurements were made and these are described below.

a) Pionic nitrogen dispersion measurement

Bragg angle	52°46'4.93"
Target gas	N_2
Target pressure	~1400 mbar
Target extraction	60 mm
Crystal tilt angle	0.35°
Transition	πN (5g-4f)
Crystal plane	(220)

A high statistics measurement was taken to determine the dispersion of the spectrometer. The reflection of the πN (5g-4f) transition was located at six different positions across the CCD detector array, by adjusting the crystal angle (measured by the angular encoder). The spectrometer arm angle was also adjusted to ensure that the crystal viewed the same part of the target cell.

b) Pionic nitrogen/muonic oxygen simultaneous measurement

Bragg angles	52°46'4.93"/ 53°21'53.24"
Target gas	N_2 10%/O_2 90%
Target pressure	~1400 mbar
Target extraction	60 mm
Crystal tilt angle	0.35°
Transitions	πN (5g-4f)/μO (5g-4f)
Crystal plane	(220)

This is the primary pion mass experimental data configuration. Simultaneous reflections from πN (5g-4f) and μO (5g-4f) were recorded, with one reflected line on each column of CCDs.

c) Pionic neon spectrometer resolution measurement

Bragg angle	45°43'16.36"
Target gas	Ne
Target pressure	~1000 mbar
Target extraction	60 mm
Crystal tilt angle	0.35°
Transition	πNe (6h-5g)
Crystal plane	(220)

X-rays from the πNe (6h-5g) transition were recorded as a test of the spectrometer resolution.

7.7.4 Fluorescence X-ray measurements

At intervals throughout the beam-run, the target chamber was removed and replaced with an X-ray tube and copper fluorescence target.

Bragg angle	53°32'58.88"/53°21'31.85"
Target	Cu
Crystal tilt angle	0.35°
Transition	Cu $K\alpha_1$/Cu $K\alpha_2$
Crystal plane	(440)

Spectra were recorded of the Cu $K\alpha_1$ and Cu $K\alpha_2$ lines as an alternative calibration line to the muonic oxygen line. The Cu Kα lines were measured in second order and have a very similar Bragg angle to the μO(5g-4f) transition. Because of this it was also used as a means of system verification when setting up the experiment.

7.7.5 CCD camera stability

During the beam run the internal ^{55}Fe source was moved into position and data taken during periods when the cyclotron trap was being refilled with liquid nitrogen. This was done for two reasons. First, it provided verification that CCD calibration remained constant. Second, other equipment in the experimental area influenced CCD noise performance. The data storage threshold was calculated as either 3σ or 5σ above the noise peak (see section 7.5.1). If read-noise was to increase after calibration, excessive data storage could occur by including events within the noise peak that would have been excluded under properly calibrated conditions.

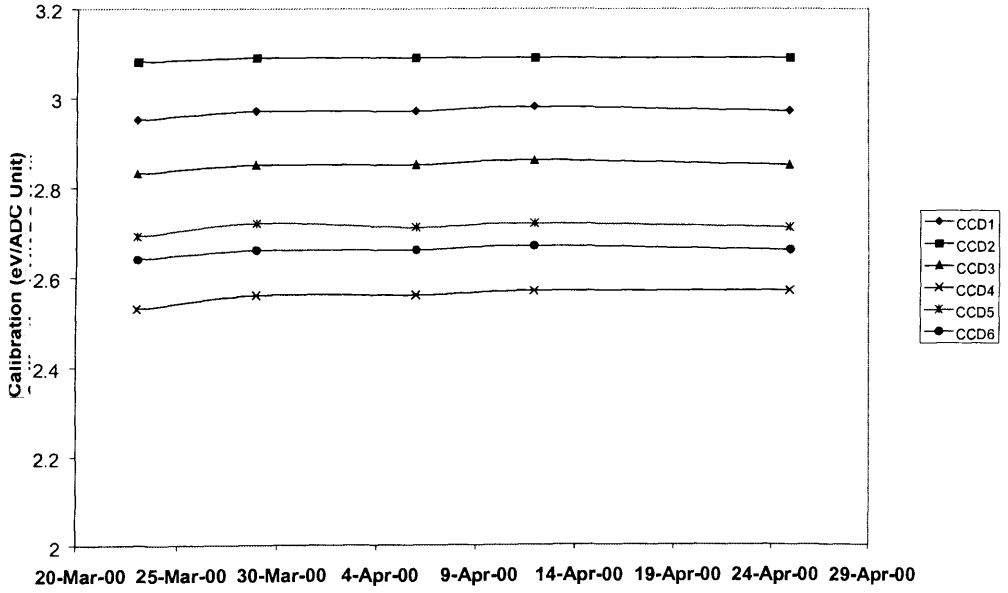

Figure 7-17. CCD calibration stability during beam run.

Calibration and read-noise variation are plotted in figures 7-17 and 7-18 respectively. The variation in gain between the CCD channels is due to differences in the on-chip amplifier, pre-amplifier and CDS processing chains. The largest variation in gain for any CCD was only 1.5% over the duration of the beam run.

7.8 Spectrometer characterisation

As input to the experimental data analysis, the spectrometer needs to be characterised. This requires measurement of the spectrometer resolution and dispersion.

7.8.1 Spectrometer resolution

The spectrometer resolution was determined by taking a high statistics measurement of X-rays from the πNe (6h-5g) transition at ~4.5 keV (see Table 7-1). Pionic neon was chosen because neon is monatomic and consequently does not suffer from Doppler broadening due to Coulomb explosion (see section 8.4.2). A one-dimensional position spectrum, corrected for reflection curvature, is shown in figure 7-19. The FWHM is ~500 meV.

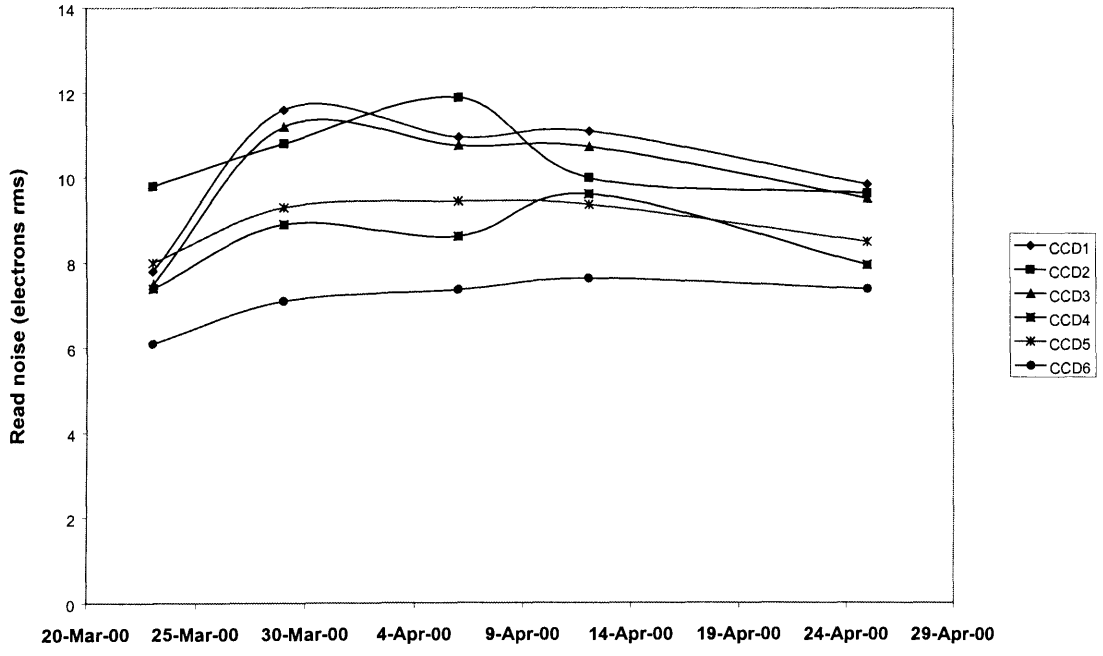

Figure 7-18. CCD read noise stability during beam run.

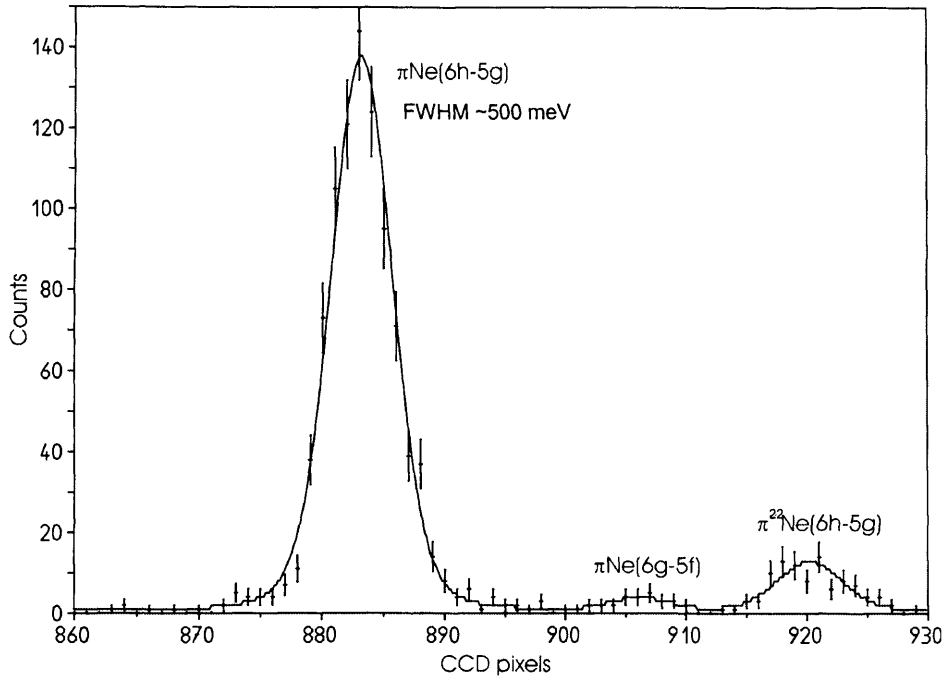

Figure 7-19. One-dimensional position spectrum of the πNe (6h-5g) transition, corrected for reflection curvature. Spectrometer resolution (FWHM) is ~500 meV. The 6h-5g line for the naturally occurring ^{22}Ne isotope is also visible.

7.8.2 Spectrometer dispersion

Spectrometer dispersion can be determined in two ways, either by direct measurement of the crystal-detector distance or by taking specific X-ray dispersion measurements and combining the results with readings from the crystal angular encoder. Both methods were employed.

The crystal-detector distance was measured directly as

$$Y_{CD} = 2386.8 \pm 0.2 \text{ mm} \qquad 7\text{-}1$$

Two sets of X-ray dispersion measurements were taken, πN (5g-4f) (see section 7.7.3) and copper fluorescence (section 7.7.4). In each case, a high statistics measurement of the reflection was recorded at six separate positions across the CCD array by adjusting the crystal angle. The spectrometer arm angle was also adjusted for each position, to ensure that the crystal viewed the same part of the target. A corrected, one-dimensional position spectrum, showing all six reflections of the pionic nitrogen transition, is shown in figure 7-20.

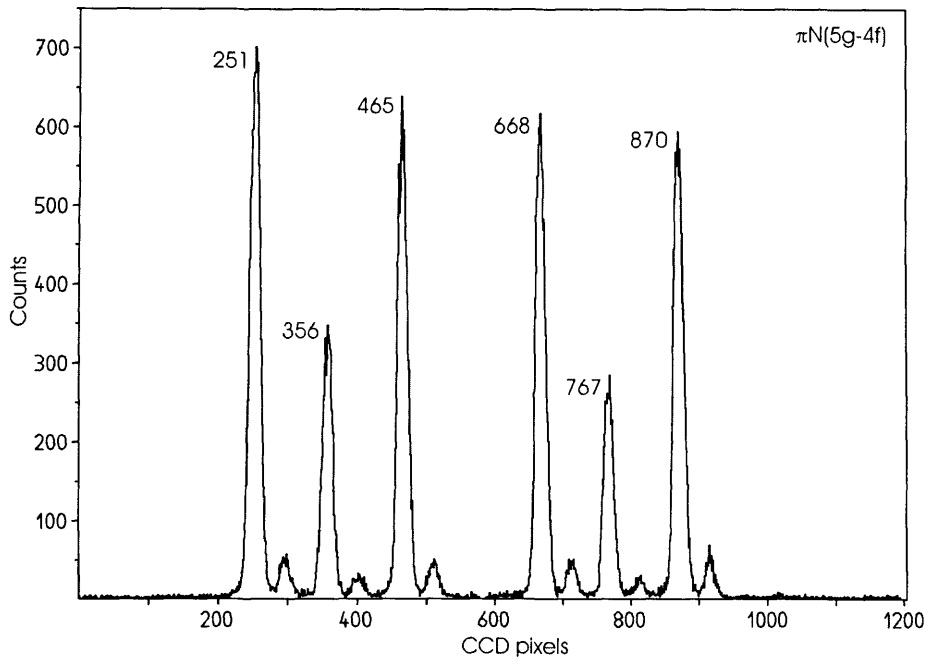

Figure 7-20. Superimposed, curvature corrected position spectrum of πN (5g-4f) transition reflections recorded at six different crystal angles. Peak positions to nearest pixel are labelled.

The peak positions of the reflections were then determined and are plotted against crystal angle in figure 7-21. From these plots, we can see that there are quite large deviations from the expected straight line, with the largest change occurring between columns of CCDs (third and fourth points on the plot). The 8 pixel deviation from expected peak position corresponds to a shift in energy terms of ~400 meV, or 100 ppm of transition energy. When the crystal angle was changed, the spectrometer arm angle was also adjusted to bring the crystal view back to the same part of the target to avoid errors due to variations in target shape. Unfortunately, a mechanical instability in the arm movement caused a distortion of the spectrometer tube, which resulted in a slight rotation of the CCD cryostat. This is evident in the non-linear relationship shown in figure 7-20 and consequently invalidates this method of spectrometer dispersion measurement. The crystal-detector distance measurement was therefore used in the following analysis.

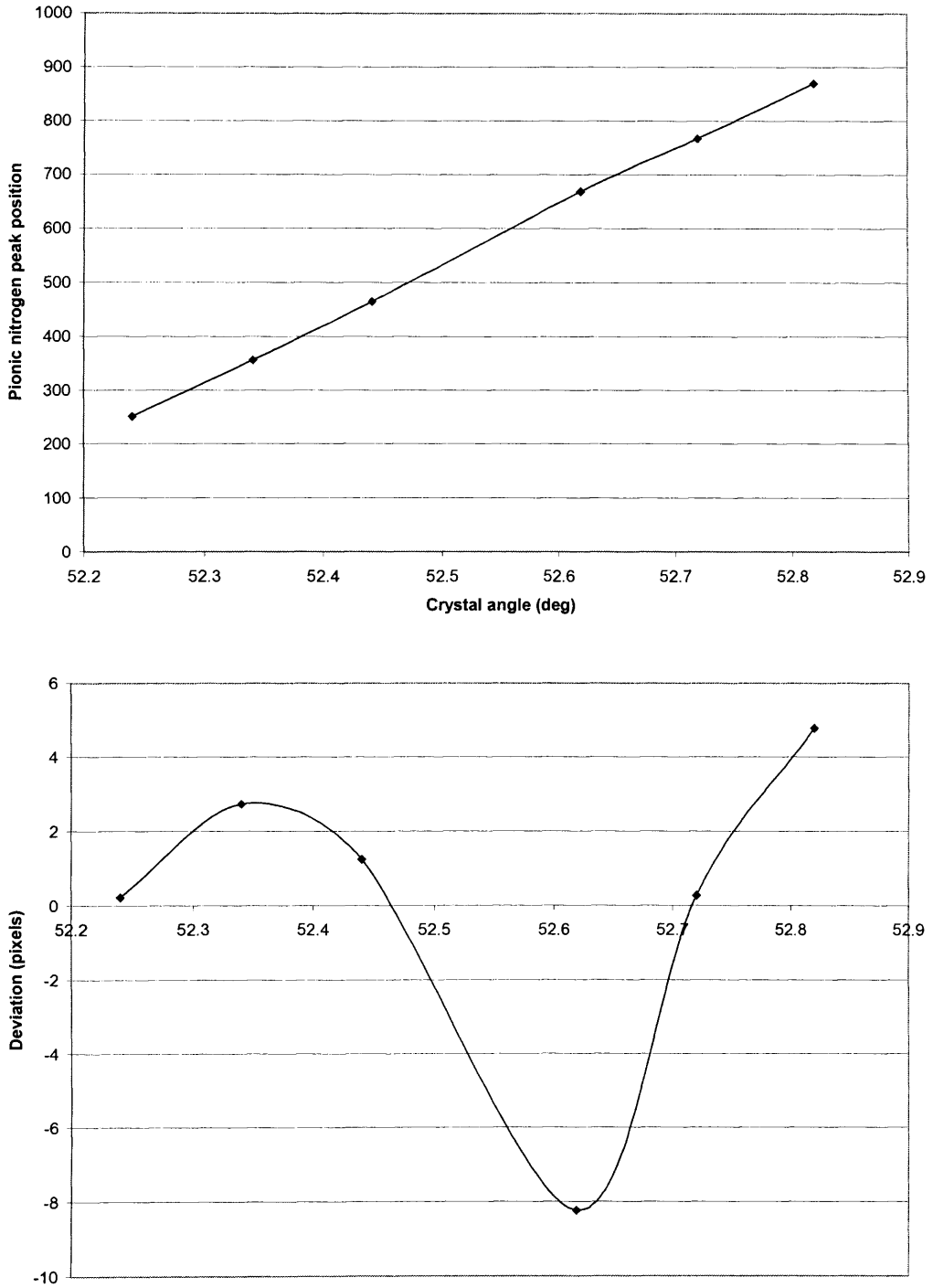

Figure 7-21. Peak position versus crystal angle (top plot) for the πN (5g-4f) dispersion measurement. The bottom plot shows the residual difference from a straight line fitted to the points in the top plot.

8 Experimental results and analysis

8.1 Introduction

The mass of the charged pion is determined from the precise energy difference between the 5g-4f transitions of muonic oxygen (μO) and pionic nitrogen (πN) (see section 7.2). The experimental data can be divided into two categories, with approximately half of the data files falling into each category. The first category contains μO and πN X-ray events and is the primary experimental data source. The second category contains calibration and characterisation data, essential for the correct analysis of the primary data. The initial aim of the data processing is to produce a two-dimensional position spectrum of the πN and μO (5g-4f) transition X-ray lines, corrected for relative rotation and displacement of the six CCDs which make up the focal plane. A one–dimensional position spectrum is then produced by applying correction for the curvature of the reflections and binning the CCD image data in the vertical direction. From this, the separation, between the πN (5g-4f) and μO (5g-4f) lines, in pixels is determined. The spectrometer dispersion, calculated either from crystal-detector distance or using specific X-ray dispersion data, is used to convert the pixel line separation into an angular separation. Finally, correction factors and systematic errors are determined to produce a measured angular difference between the πN (5g-4f) line and accurately known (in terms of Bragg angle) μO (5g-4f) line. Once the Bragg angle is known, it is a simple matter to convert this to wavelength using the modified Bragg law. This in turn is converted to an energy value and then using calculations from QED we obtain a value directly for the pion mass.

To put the following analysis into perspective, some simple calculations can be performed. An accurate determination of the charged pion mass, with a precision of order 1 ppm is sought. As we have seen, the pion mass is directly proportional to the energy of the X-ray transition we are measuring, πN (5g-4f), separated by <32 eV from the calibration line μO (5g-4f). The angular separation of these lines at the detector is ~35'50'' and this is equivalent to ~600 CCD pixels. Using these numbers we can make the following (approximate) statements about the experimental arrangement:

1 CCD pixel $\equiv$ 0.053 eV $\equiv$ 13 ppm

1" Angular separation at CCD $\equiv$ 0.015 eV $\equiv$ 3.7 ppm

From these equivalencies, we can immediately see that to get close to 1 ppm precision, we are looking for total errors of order one-tenth of a pixel or a quarter of an arc-second.

8.2 Relative CCD alignment

A single spectral line is typically reflected onto a column of CCDs, often with reflections on both columns. Consequently, prior to the analysis of any detector data, the positional and rotational relationship between the six CCDs must be determined, to the level of one-tenth of a CCD pixel or better. To provide the relative location and orientation information for each CCD, two different approaches were adopted. The first was to place an aluminium mask, with identifying features, in front of the detector array and to illuminate it with X-rays. The second was to remove the CCD camera from the cryostat and use an optical measuring machine to determine the relative positions of two reference points on each CCD. The optical method, described in appendix A2, suffers from an unknown systematic error at the present time and is currently discounted. The mask alignment procedure is described in the following section.

8.2.1 Mask alignment

The alignment measurement was done by illuminating the CCD array through the mask using sulphur Kα fluorescence X-rays (2.31 keV), excited by means of an X-ray tube (see figure 8-1).

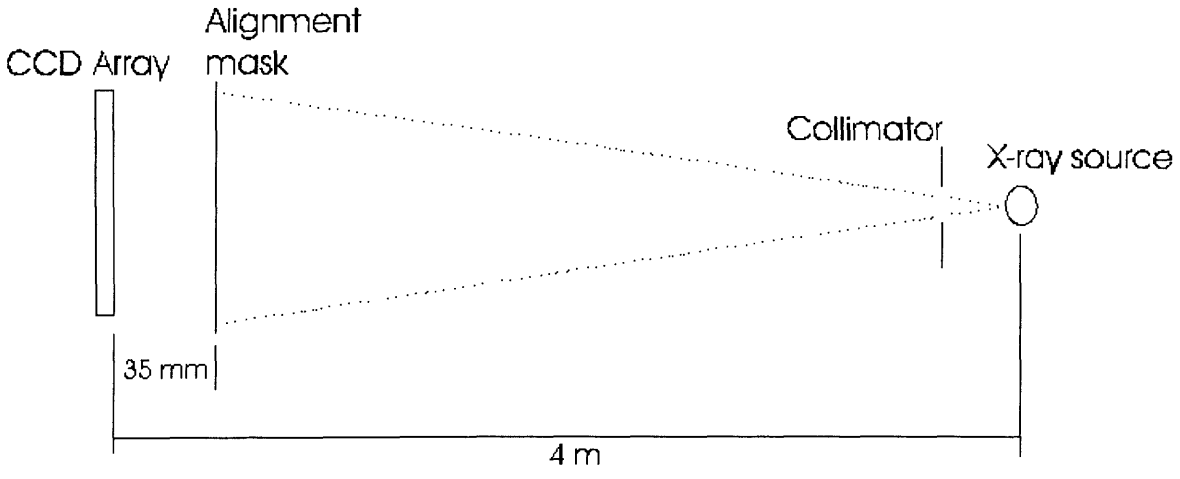

Figure 8-1. CCD mask alignment measurement arrangement. The collimator is 5 mm in diameter and located 100 mm in front of the source.

To avoid aberrations, the sulphur target was positioned 4 m in front of the mask, which in turn is ~35 mm from the CCD array. A 5 mm diameter collimator was placed 100 mm in front of the target, to produce an approximate "point like" source and to eliminate unwanted scatter. CCD data was collected for 44 hours (~530000 events) and is plotted in figure 8-2.

The aluminium mask itself is 1 mm thick and the slits are wire eroded to a width of 0.15 mm. The slits have an integral non-linearity of 5 μm along their length and the pattern in the mask is designed to provide either a horizontal or vertical line and a diagonal line, which cross the boundary between adjacent CCDs. Using this pattern, alignment determination is possible without precise knowledge of the distance between the mask and CCD surface. Two corrections need to be determined, individual CCD rotation and relative CCD displacement.

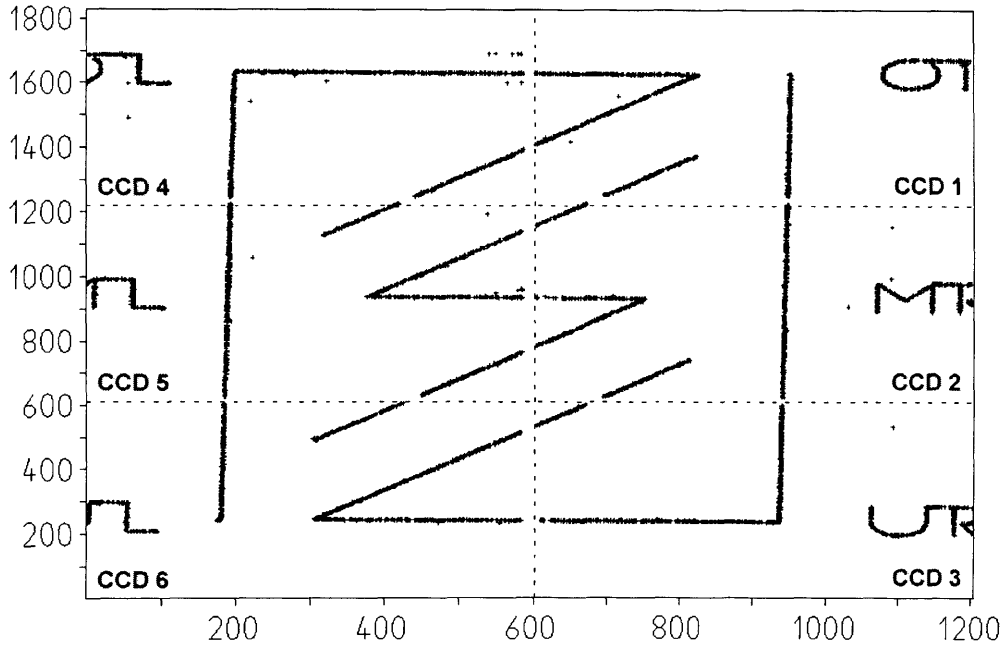

Figure 8-2. CCD mask alignment data (the CCD x label is not part of the data).

The rotations were calculated first by using a least-squares fit to obtain the slope of all lines on each CCD. From the image data, horizontal and vertical lines are assumed to have a width of 4 pixels (4 x 40 μm) and the diagonal lines a width of 6 pixels. Diagonal lines were fitted in both the horizontal and the vertical directions. The relative rotations of the CCDs were then obtained by comparing the slope of a mask slit image that appears on different CCDs. For example, a horizontal mask slit image covers both CCD3 and CCD6. Where more than one line crosses between a pair of CCDs, the weighted average of the two fits was used. Table 8-1 shows the calculated rotations of each CCD relative to CCD3. The choice of reference CCD is somewhat arbitrary, but CCD3 was chosen because it offers longer lines (higher statistics) for column1 and for relating the two columns via CCD6. CCD4 and CCD5 rotations are the weighted averages of rotations determined indirectly via CCD1 and CCD6.

CCD	Relative rotation (mrad)
1	0.094±0.110
2	0.343±0.56
3	0
4	1.861±0.109
5	2.984±0.091
6	6.660±0.093

Table 8-1. CCD rotations relative to CCD3.

After correcting for rotation, a new line fit was performed to determine the boundary intercept of the slit lines with the edge of each CCD, see figure 8-3.

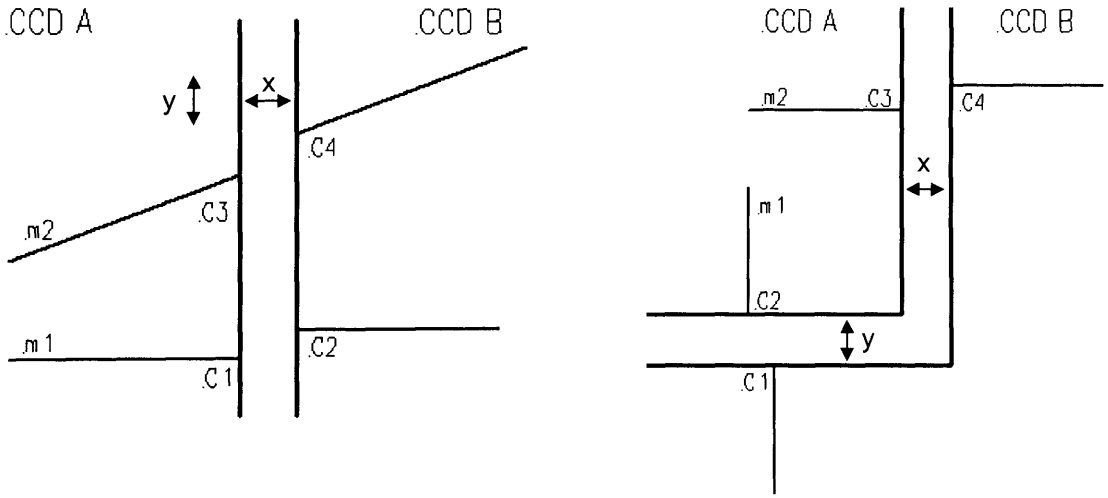

Figure 8-3. CCD mask line boundary point (C*) and slope definitions (m*). x and y are the horizontal and vertical offsets respectively.

The relative offsets of the CCDs can now be determined, provided there are at least two lines crossing the boundary region of each CCD junction (see figure 8-3) [100]. For the situation where one horizontal and one vertical line cross the CCD boundary, we get

$$C_2 = y + C_1 + m_1 x \qquad 8\text{-}1$$

and

$$C_4 = y + C_3 + m_2 x \ . \qquad 8\text{-}2$$

Combining equations 8-1 and 8-2 we obtain an expression for the horizontal offset,

$$x = \frac{(C_2 - C_4) - (C_1 - C_3))}{m_1 - m_2} \ , \qquad 8\text{-}3$$

The error of the horizontal offset, in terms of errors on the measured parameters, is obtained by partial differentiation of eq. 8-3,

$$\Delta x^2 = \frac{\Delta C_1^2 + \Delta C_2^2 + \Delta C_3^2 + \Delta C_4^2}{(m_1 - m_2)^2} + \frac{(\Delta m_1^2 + \Delta m_2^2) \cdot (C_2 - C_4 - C_1 + C_3)^2}{(m_1 - m_2)^4} \qquad 8\text{-}4$$

In the case of one horizontal and one vertical line,

$$x = \frac{C_1 - C_2 - m_1(C_3 - C_4)}{m_1 m_2 - 1} \ , \qquad 8\text{-}5$$

and the error is given by

$$\begin{aligned} \Delta x^2 = & \frac{\Delta C_1^2 + \Delta C_2^2 + \Delta m_1^2 (\Delta C_3^2 + \Delta C_4^2)}{(m_1 m_2 - 1)^2} \\ & + \Delta m_1^2 \left(\frac{C_4 - C_3}{m_1 m_2 - 1} - \frac{m_2 (C_1 - C_2 - m_1 (C_3 - C_4))}{(m_1 m_2 - 1)^2} \right)^2 \\ & + \Delta m_2^2 \left(\frac{m_1 (C_1 - C_2 - m_1 (C_3 - C_4))}{(m_1 m_2 - 1)^2} \right)^2 \end{aligned} \qquad 8\text{-}6$$

The y values are then determined by substituting for x in eq. 8-2 or 8-3. The y-value errors are obtained by re-working the x-value procedures outlined above.

Using the measured values for the line intercepts, we obtain the relative CCD displacements listed in table 8-2.

CCD	X offset (pixels)	Y offset (pixels)
1	-2.818±0.022	22.264±0.077
2	-1.049±0.015	10.901±0.085
3	0	0
4	-14.347±0.046	20.808±0.075
5	-14.597±0.0243	12.265±0.064
6	-16.487±0.040	1.173±0.052

Table 8-2. CCD offsets (relative to CCD3), after rotation correction, determined using mask alignment.

8.2.2 CCD alignment correction

The relative rotations and displacements of the six CCDs are applied to all X-ray data files prior to any further data processing. When a CCD image is rotated or shifted, it is quite probable for an X-ray event to be moved by a sub-pixel amount. In the case of single pixel events, it is not possible to determine the sub-pixel interaction location of the X-ray and so is given a random intra-pixel starting point. With multi-pixel events the interaction position can be determined using a weighted average of the charge values in each pixel. The rotation, followed by shift is then applied to this calculated interaction position to give a new pixel location. In the case of multi-pixel events, the original charge distribution is preserved for analysis by the X-ray event software. The random distribution of the X-ray interaction point introduces an error that is quantified by Monte Carlo simulation (see section 8.4.2).

8.3 X-ray event processing

The vast majority of events recorded in each detector frame are background events generated by the beam line, typically 2000:1. The initial aims of data processing are to remove the intense background signal. Fast charged particles and high-energy Compton-induced events generally create multi-pixel events in the CCD, whereas for low energy X-rays the charge is generated by photo-effect and, if the interaction occurs within the depletion region, typically deposited in one or two adjacent pixels only (figure 8-4). For the CCD22, at 4 keV, the energy of the pionic and muonic lines, about 90% of X-rays are converted before reaching the field-free region (figure 4-6). The first stage in the data analysis is to apply topographic discrimination to the recorded events.

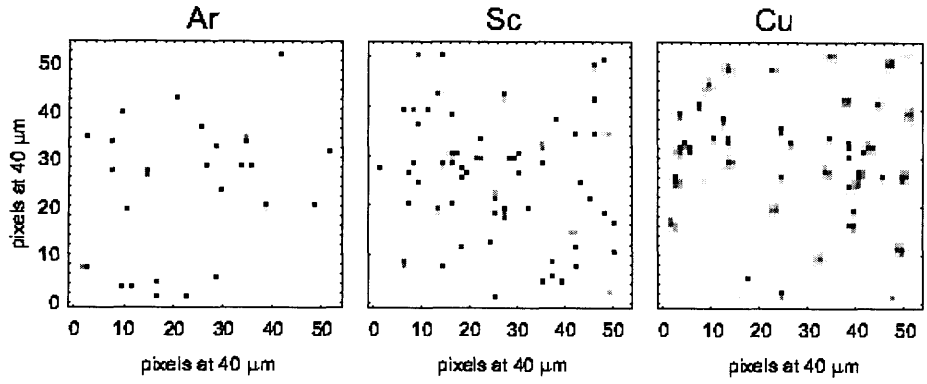

Figure 8-4. Comparison of event cluster size for incident X-rays of 2.96 keV (Ar), 4.10 keV (Sc) and 8.04 keV (Cu). Each plot shows a 50 pixel square region from the centre of the reflection. The large increase in multi-pixel events for Cu X-rays is evident, due to conversion in the field-free region of the CCD. Event size percentages for 1, 2 and 4 (or more) pixel events are Ar (76/22/2), Sc(68/22/10) and Cu(54/29/17).

The discrimination was performed, one frame at a time, using software to determine each event size and all events of more than two pixels were discarded. The two-pixel events were assumed to come from a single X-ray and their charge added together. The position of each two-pixel event was determined by the pixel containing the highest charge. An energy histogram was then produced, by summing the remaining events from all frames of data.

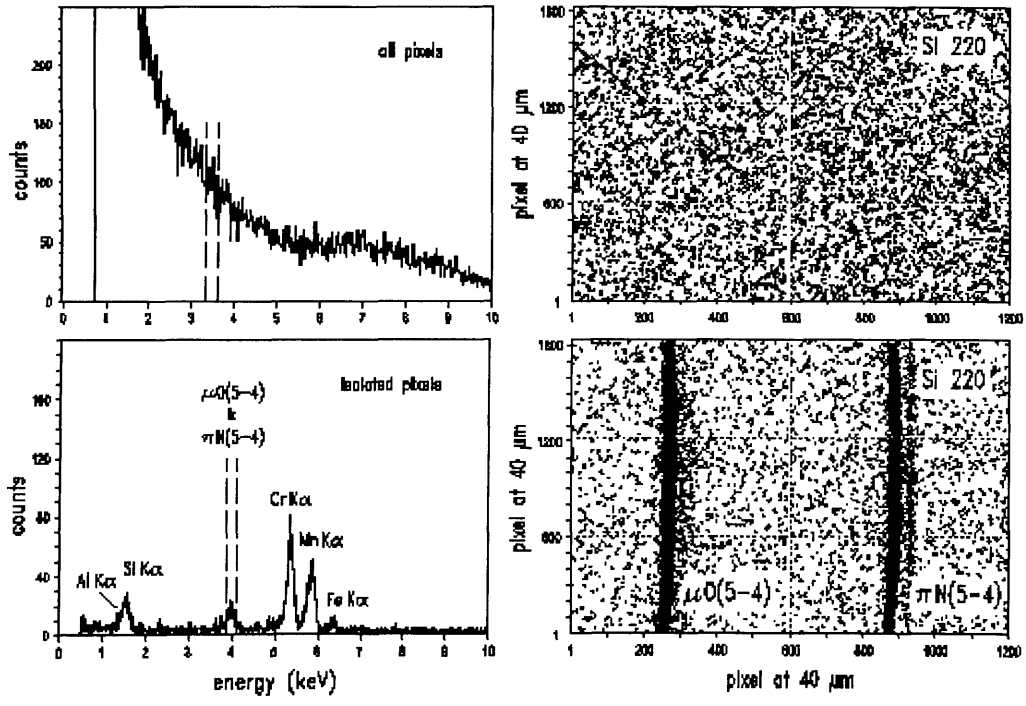

Figure 8-5. Energy and two-dimensional position spectra of simultaneously recorded πN and μO (5g-4f) transitions are shown before topographic and energy discrimination (top) and after (bottom).

Less than 32 eV separates the πN and μO (5g-4f) lines, which are indistinguishable in energy terms by the CCD and an energy window was defined around the exotic atom X-ray events. All events falling outside this window were removed from the spectra. Energy histograms and two-dimensional position spectra are plotted in figure 8-5, showing before and after topographic and energy discrimination. In the top plots, before cluster analysis, the X-ray lines are indistinguishable in the energy spectrum. The two-dimensional image plot represents data from a short period only, otherwise the image would be completely black due to the very large number of background events. A cosmic ray track, which crosses the boundary between two CCDs, is visible in the upper left. After processing, the X-ray lines in the energy spectrum are now prominent with the πN and μO (5g-4f) reflections clearly defined in the image plot. The curvature of the reflected lines, due to the spherical nature of the crystal, is apparent.

8.4 One-dimensional position spectrum

A one-dimensional position spectrum is obtained by applying curvature correction and binning the two-dimensional CCD data in the vertical direction. From this spectrum, the peak separation of the πN and μO (5g-4f) lines is determined.

8.4.1 Curvature correction

Curvature correction is easily obtained from the two-dimensional position spectrum. A high-statistics, narrow reflection provides the best option for fitting and so the experimental data lines were used. A region of interest is selected around the reflected line and it is divided into twelve vertical slices (figure 8-6a). The centre of gravity (COG) is then calculated for each slice and a quadratic curve fitted to the COGs. A new, curved region of interest is then determined (figure 8-6b) and the process iterated, until a minimum chi-square value is obtained. Curvature corrections were determined for both the πN (5g-4f) and the μO (5g-4f) lines and are given in Table 8-3, as quadratic coefficients of the format $x_2 = cx_1^2 + bx_1 + a$, where x_1 is the original x coordinate and x_2 is the corrected x coordinate.

Line	a	b	c
πN (5g-4f)	870.099 ± 0.2456	0.02552 ± 0.00059	$-1.13508\times10^{-5} \pm 0.00314\times10^{-5}$
μO (5g-4f)	251.871 ± 0.2802	0.02581 ± 0.00067	$-1.12323\times10^{-5} \pm 0.00360\times10^{-5}$
average	-	0.02567	-1.12916×10^{-5}

Table 8-3. Curvature correction coefficients for πN (5g-4f) and μO (5g-4f) lines.

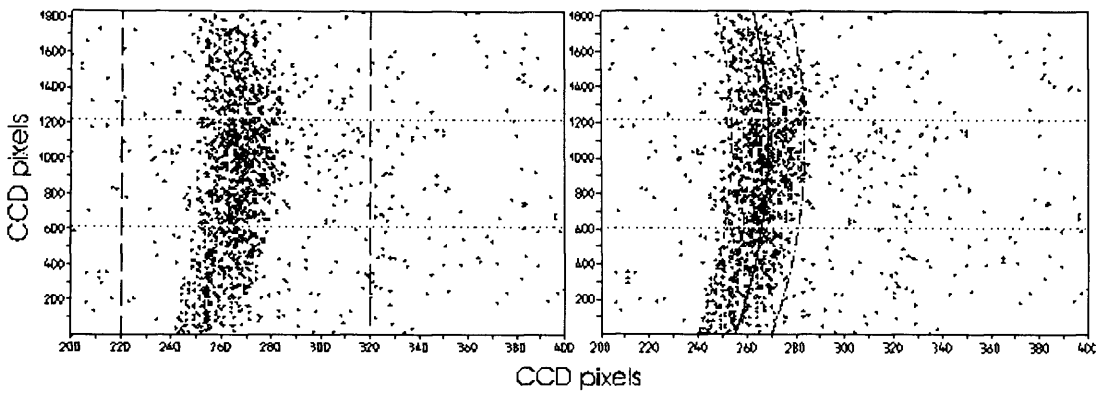

Figure 8-6. Regions of interest used for curvature correction determination (indicated by the dashed lines). Figure a (left), initial fit. Figure b (right), iterated fit.

The experiment is sensitive to the relative position of the two reflections and the energy of the two lines is very close. Consequently, to avoid introducing a systematic error, it is essential to use the same curvature correction for both lines. As the two sets of coefficients are so similar it was decided to use the average for the final correction. After applying curvature correction to the spectrum of figure 8-5 and binning in the vertical direction, we obtain a one-dimensional position spectrum for the simultaneous πN and μO (5g-4f) transition X-ray measurement (figure 8-7). The 5g-4f and the parallel 5f-4d transitions can be clearly seen.

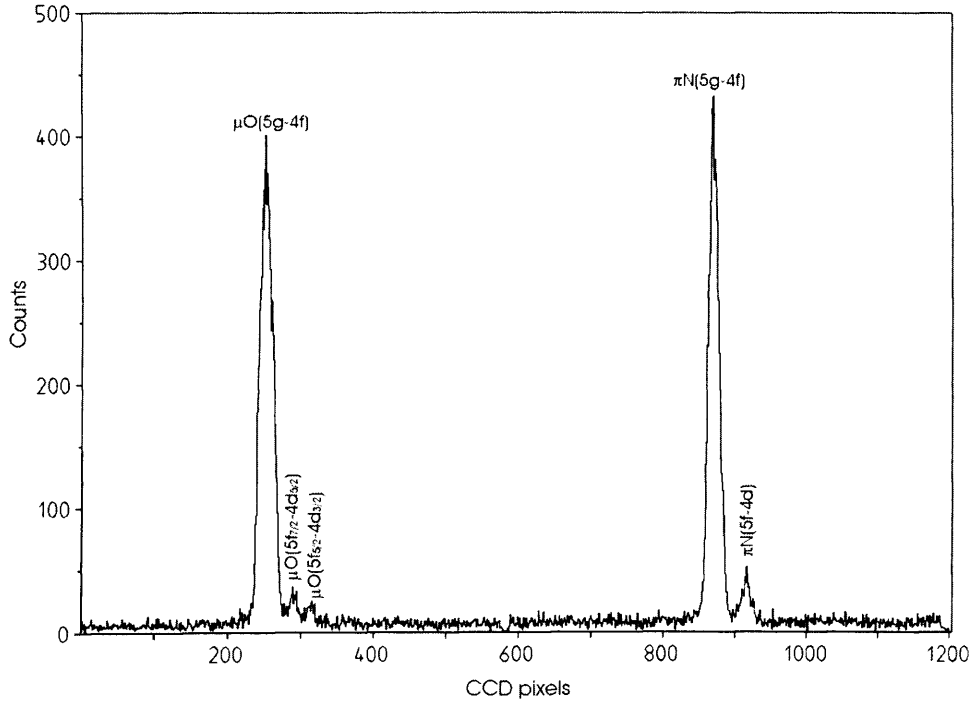

Figure 8-7. Final one-dimensional position spectrum for simultaneously measured πN and μO (5g-4f) transitions after applying curvature correction and binning in the vertical direction. The fine structure of the μO (5g-4f) transition is not resolved but the parallel 5f-4d transitions can be seen for both lines (except for the low intensity μO ($5f_{5/2}$-$4d_{5/2}$) (see table 7-1).

8.4.2 πN and μO (5-4) line separation

To calculate the separation of the πN and μO (5g-4f) lines, we first need to determine the peak position of each response curve in figure 8-7. Both curves have complex line shapes, with contributions from a number of different sources. These are discussed below, first for muonic oxygen and then for pionic nitrogen.

The μO (5g-4f) transition is split into three different lines due to the spin of the muon. These are μO ($5g_{7/2}$-$4f_{7/2}$), μO ($5g_{9/2}$-$4f_{7/2}$) and μO ($5g_{7/2}$-$4f_{5/2}$), their energies and relative intensities are listed in Table 7-1. The parallel 5f-4d transition has a similar splitting. These lines are for ^{16}O, but ^{18}O is a naturally occurring isotope at the 0.21% level and makes a noticeable contribution from the $\mu^{18}O$ ($5g_{9/2}$-$4f_{7/2}$) transition. No fine structure splitting occurs in the case of pionic nitrogen, but the parallel 5f-4d transition must be taken into account, along with a small contribution from the naturally occurring (0.36%) ^{15}N, 5g-4f transition.

A number of factors have a significant effect on both response curves, the first being Doppler shift due to Coulomb explosion [96]. Both oxygen and nitrogen are diatomic and as electrons are ejected during de-excitation (of the exotic atoms), the ionisation reaches a level where the Coulomb repulsion between nuclei forces the molecule apart, causing a Doppler shift in the observable transition energy. This results in a symmetrical broadening of the base of the response curve. Consequently, the FWHM of the pionic nitrogen and muonic oxygen lines is of order 800 meV, compared to only 500 meV for pionic neon (see section 7.8.1). Secondly, although cascade models predict a high probability of complete ionisation in the case of pionic nitrogen and muonic oxygen, there is still a small chance (~2-3%) of one or two K shell electrons remaining [101]. This causes an increase in the observed X-ray energy, due to electron screening of the nucleus, of 0.494 eV for πN (5g-4f) and 1.050 eV for μO (5g-4f) in the case of one K shell electron remaining. These energy shifts are doubled when two K shell electrons remain. Finally, de-focusing of the reflected lines (due to the use of a flat detector positioned perpendicular to the incoming X-rays – see section 8.6.5) introduces an asymmetrical shift in the response curve, towards the high-energy side.

Figure 8-8 shows the fitted response curves for both muonic oxygen and pionic nitrogen, with contributions from the various factors identified.

The peak positions of the μO ($5g_{9/2}$-$4f_{7/2}$) and πN (5g-4f) lines were then determined from the fitted curves, as

μO ($5g_{9/2}$-$4f_{7/2}$)	248.507 ± 0.096 pixels	8-8a
πN (5g-4f)	871.026 ± 0.091 pixels.	8-8b

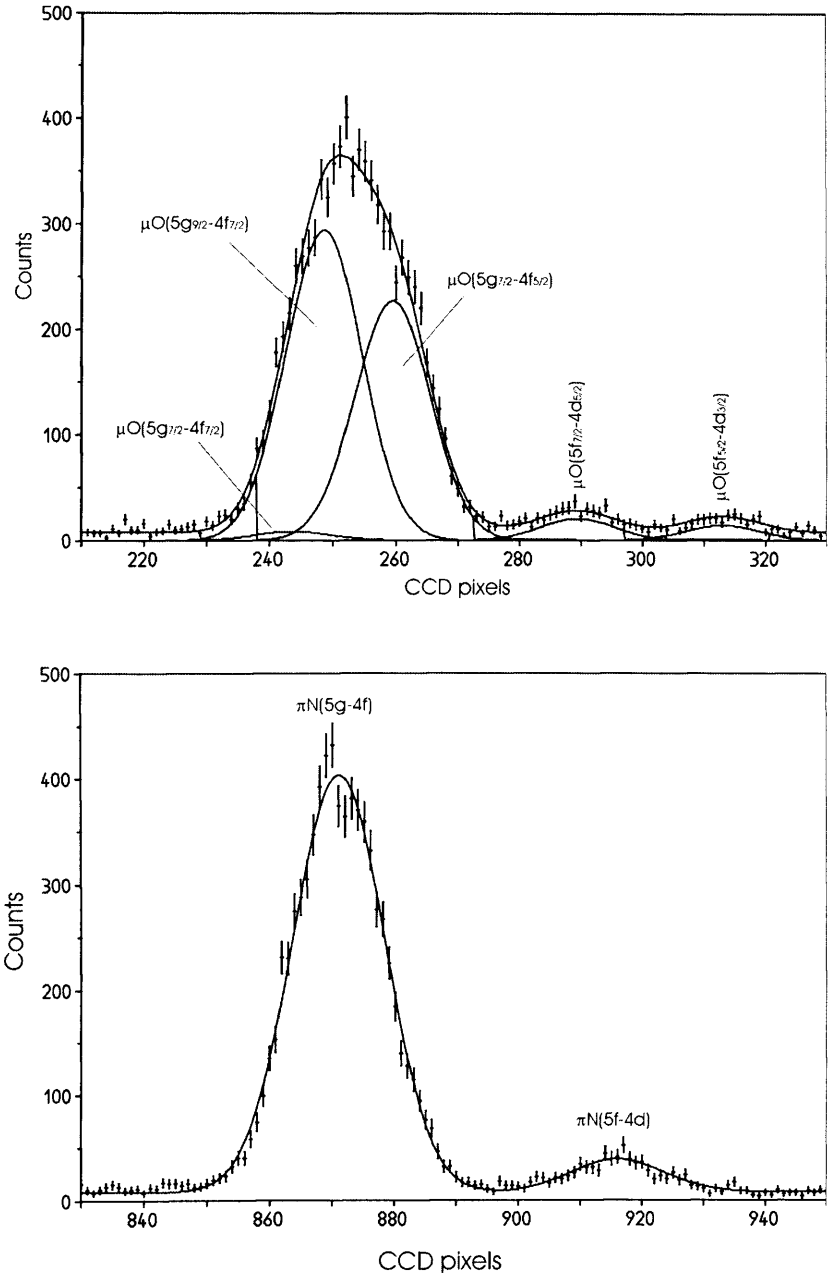

Figure 8-8. Curve function models fitted to measured response profiles of the μO (top) and πN (bottom) (5-4) regions. Reduced chi-square values for fits are $r\chi^2$ (μO) = 0.699, $r\chi^2$ (πN) = 0.857. Components due to fine structure splitting (μO) are identified. Contributions from naturally occurring isotopes and any remaining k-shell electrons are accounted for but too small to be seen in the figure. Line broadening due to Coulomb explosion is modeled by fitting a Voigt profile instead of a simple Gaussian.

The relative energies and intensities of the μO fine structure splitting are known from QED and atomic theory and allow the statistical error for the peak position to obtained by treating the curve fitting as that of a single line.

We also need to take into account the error introduced by the Monte Carlo redistribution of X-ray events during the CCD alignment correction (see section 8.2.2). This was determined by performing 1000 rotation and alignment corrections on the same initial two-dimensional position spectrum and calculating the peak position of the μO (5g-4f) and πN (5g-4f) lines. The statistical distribution of the peak positions then provided the error introduced by the alignment correction process, giving an uncertainty for each line position of

$$\Delta MC\ \mu O\ (5g\text{-}4f) = 0.014 \text{ pixels} \qquad 8\text{-}8a$$

$$\Delta MC\ \pi N\ (5g\text{-}4f) = 0.014 \text{ pixels.} \qquad 8\text{-}8b$$

Combining these uncertainties with the peak positions from eq. 8-7, we obtain an uncorrected peak separation and uncertainties of

$$\text{peak separation } (pixels \pm \Delta fit \pm \Delta MC) = 622.519 \pm 0.132 \pm 0.020 \text{ pixels.} \qquad 8\text{-}9$$

8.5 Spectrometer dispersion

To convert the peak separation in pixels into an angular difference requires knowledge of the spectrometer dispersion. The dispersion is calculated using the crystal-detector distance (Y_{CD}), measured as 2386.8 ± 0.2 mm. From eqs. 3-14 and 3-18, we obtain an angular difference of

$$\tan(\Delta\theta) = \frac{\Delta x}{Y_{CD}} . \qquad 8\text{-}10$$

Substituting for Δx (622.519 x 40 μm CCD pixel size) and Y_{CD}, we obtain an uncorrected angle difference between the πN (5g-4f) and μO ($5g_{9/2}$-$4f_{7/2}$) lines of

$$\text{uncorrected peak separation} = 35' \ 51.88'' \pm 0.46'' , \qquad 8\text{-}11$$

where the error is the total statistical error given by $\Delta stat = \sqrt{(\Delta fit^2 + \Delta MC^2)}$.

The contributions to the uncorrected angle difference are summarised in Table 8-4.

Contribution	$\mu O(5g_{9/2}\text{-}4f_{7/2})$	$\pi N(5g\text{-}4f)$
Line position (pixels)	248.507	871.026
Statistical error Δfit (pixels)	± 0.096	± 0.091
MC redistribution error ΔMC (pixels)	± 0.014	± 0.014
Line position difference (pixels ± Δfit ± ΔMC)	622.519 ± 0.132 ± 0.020	
Crystal-detector distance (mm)	2386.8 ± 0.2	
Uncorrected angular separation	35' 51.88" ± 0.46"	

Table 8-4. Determination of the uncorrected angle difference between πN (5g-4f) and μO ($5g_{9/2}$-$4f_{7/2}$) lines.

8.6 Correction factors

A number of instrumental correction factors need to be applied to the peak separation calculated from the one-dimensional position spectrum. These are described below in detail and calculated for the experimental conditions.

8.6.1 Crystal temperature correction

The crystal temperature was passively monitored using three Platinum Resistance Thermometers (PRT), one on the front of the crystal, one on the back and one inside the crystal chamber. The variation of these temperatures over the duration of the beam run is plotted in figure 8-19.

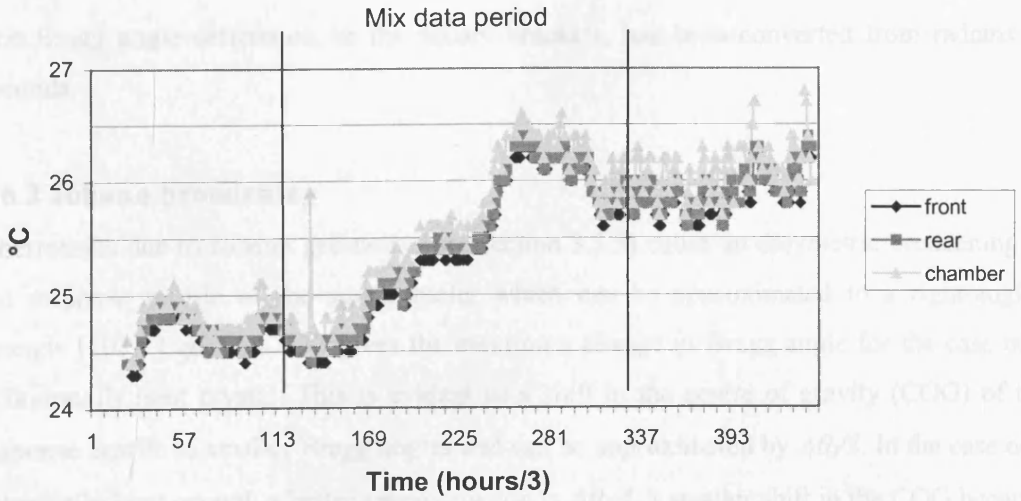

Figure 8-9. Crystal and housing temperature variation over the duration of the beam run. The mix data period, where simultaneous pionic nitrogen and muonic oxygen data were recorded, is identified.

The crystal d spacing is temperature dependent and can be calculated for the minimum and maximum temperatures of the crystal measured during the beam run (eq. 3-2). However, it is simpler to calculate the change in Bragg angle difference (between the πN and μO (5g-4f) lines). If we start with the Bragg law (eq. 3-1) and differentiate $sin\theta$ with respect to d, we get

$$\frac{\Delta\theta}{(\Delta d/d)} = -\tan\theta \ . \qquad 8\text{-}12$$

$\Delta\theta$ is the change in Bragg angle θ for a given change in d spacing, $\Delta d/d$ which in turn is given by αT, where T is the temperature change and α is the thermal expansion coefficient of Si, 2.56 x 10^{-6} /°C [102]. The Bragg angle difference is then given by

$$\Delta\theta_1 - \Delta\theta_2 = (\Delta d/d)[\tan\theta_2 - \tan\theta_1] \ , \qquad 8\text{-}13$$

where θ is in radians. From figure 8-9, we can see that a maximum temperature variation of 2.0 °C occurred over the period of the πN and μO simultaneous data measurement. Substituting this value into eq. 8-14 and using the Bragg angle values from table 7-1, we obtain a change in Bragg angle difference, $\Delta\theta_{BD}$, of

$$(2.0 \times 2.56 \times 10^{-6})\ [-5948.44''] = -0.030''. \qquad 8\text{-}14$$

The Bragg angle difference, in the square brackets, has been converted from radians to seconds.

8.6.2 Johann broadening

Aberrations due to Johann geometry (see section 3.3.5) cause an assymetric broadening in the response profile of the spectrometer which can be approximated to a right-angled triangle [103]. Equation 3-33 gives the maximum change in Bragg angle for the case of a cylindrically bent crystal. This is evident as a shift in the centre of gravity (COG) of the response profile to smaller Bragg angles and can be approximated by $\Delta\theta_I/3$. In the case of a spherically bent crystal, a better approximation is $\Delta\theta_I/4$, a smaller shift in the COG because the crystal width, b, reduces as you move towards the top and bottom of the crystal. The experimental width of the crystal is determined by the aperture plate, which has an effective diameter of 90 mm. The radius of curvature of the crystal, R_C, is 2985.4 ± 0.1

mm. Substituting these values into eq.3-33, and again using the Bragg angles from table 7-1, we obtain response profile shifts of

$$\Delta\theta_f(\mu O)/4 = -3.24" \qquad 8\text{-}15a$$

$$\Delta\theta_f(\pi N)/4 = -3.38" \qquad 8\text{-}15b$$

and a change in Bragg angle difference between the πN and μO (5-4) lines of

$$\Delta\theta_f(\mu O)/4 - \Delta\theta_f(\pi N)/4 = 0.14". \qquad 8\text{-}16$$

This result demonstrates the order of magnitude of the change in Bragg angle due to Johann broadening, but in this instance, the correction factor is included as part of the de-focussing Monte Carlo simulation (section 8.6.5).

8.6.3 Crystal bending correction

Bending the initially flat crystal, causes lattice deformation and consequently the d spacing is altered (see section 3.3.6). The central neutral layer of the crystal retains the original d spacing which increases towards the back and decreases towards the front. The relative change in the d spacing, taking into account extinction length (at energy e), Z_e, and the elasticity (Poisson number) of Si (= 0.25), is given by equation 3-34, repeated here for clarity,

$$\frac{\Delta d}{d} = -\frac{2\nu}{1-\nu}\frac{Z_e - \delta}{R_C}, \qquad 8\text{-}17$$

where δ is the distance of the crystal surface to the neutral layer (or crystal thickness divided by 2) which is 0.145 mm and R_C is the radius of curvature of the crystal. The extinction length is different for p and s polarisation and, since the X-rays in this experiment are unpolarised, we use the weighted average. The extinction lengths were calculated using the XOP2 computer program [104] and are listed in table 8-5.

Substituting these values into eq. 8-17 and using the relationship from eq. 8-12, we obtain Bragg angle corrections as follows,

$$\Delta\theta_b(\mu O) = 8.49" \qquad 8\text{-}18a$$

$$\Delta\theta_b(\pi N) = 8.31" \qquad 8\text{-}18a$$

and a relative change in Bragg angle of

$$\Delta\theta_b(\mu O) - \Delta\theta_b(\pi N) = 0.18''. \qquad 8\text{-}19$$

	p – polarisation		s - polarisation		
Energy (eV)	Extinction length (μm)	Relative intensity	Extinction length (μm)	Relative intensity	Mean extinction length (μm)
4023.75253	16.29	13.83	4.69	69.88	6.60
4055.38078	17.89	12.25	4.79	69.50	6.75

Table 8-5. Crystal extinction lengths for πN (5g-4f) (top) and μO ($5g_{9/2}$-$4f_{7/2}$) (bottom) X-ray photons. The transition energies are from table 7-1.

8.6.4 Penetration depth correction

There is a simple geometrical aberration caused by X-rays on the same path being reflected at different depths within the crystal. This results in a change in Bragg angle, which can be approximated by [105]

$$\Delta\theta_p \approx \frac{Z_e}{R_C}\cot\theta_B\,, \qquad 8\text{-}20$$

where Z_e is the extinction length (at energy e), R_C is the radius of curvature of the crystal and θ_B is the Bragg angle. Substituting in values from section 8.6.3, we get the following changes in Bragg angle for πN and μO (5g-4f) transitions

$$\Delta\theta_p(\mu O) = -0.41'' \qquad 8\text{-}21a$$

$$\Delta\theta_p(\pi N) = -0.42'' \qquad 8\text{-}21b$$

and a relative change in Bragg angle of

$$\Delta\theta_p(\mu O) - \Delta\theta_p(\pi N) = 0.01''. \qquad 8\text{-}22$$

8.6.5 De-focusing correction

A flat detector can be positioned such that it lies on the Rowland Circle (RC) at one point only. The centre of the detector was chosen to sit on the RC. Consequently the πN (5g-4f)

line focus is in front of the detector and the μO (5-4) line focus is behind the detector (figure 8-10).

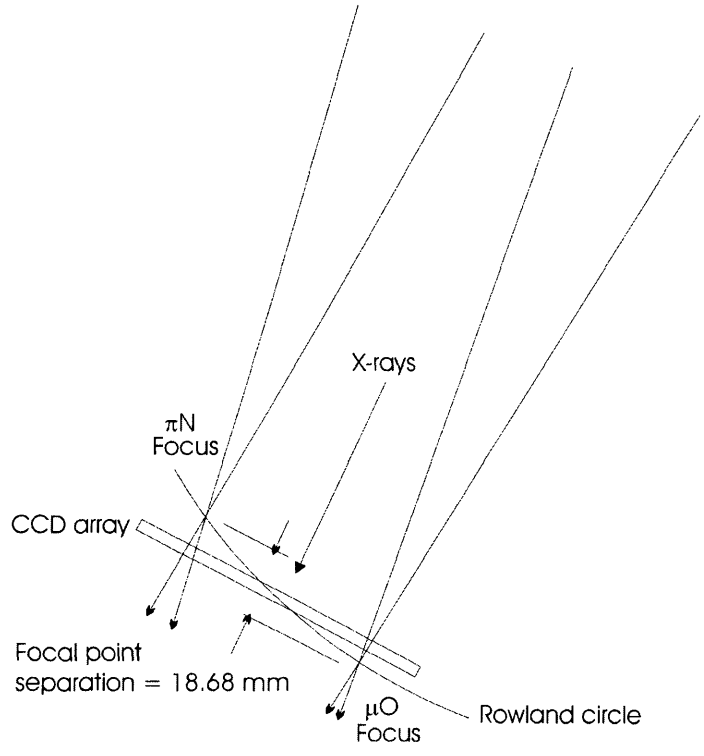

Figure 8-10. Detector position on the Rowland Circle.

Using eq. 3-14, the distance between the focal points along the crystal-detector direction is given by

$$d_F = R_C \sin\theta_{B\mu} - R_C \sin\theta_{B\pi} \ , \qquad 8\text{-}23$$

where R_C is the radius of curvature of the crystal, $\theta_{B\mu}$ is the μO (5g-4f) line Bragg angle and $\theta_{B\pi}$ is the πN (5g-4f) line Bragg angle. Substituting for crystal radius of curvature, along with the Bragg angle values from table 7-1 into eq. 8-23 we obtain an in-line distance between the πN (5g-4f) and the μO (5g-4f) line foci of 18.68 mm. For small distances from the RC, Monte Carlo studies [106] have shown that the change in reflected line separation is dependent only upon the distance between the focal points, not on the relative position of the detector to the RC (figure 8-11).

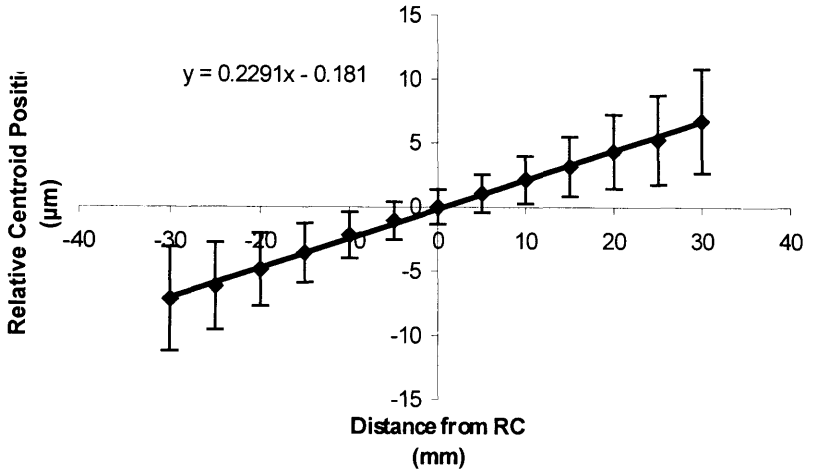

Figure 8-11. Monte Carlo model results showing relative line centroid shift with respect to distance from the RC. The error on the line fit is only the error shown divided by $\sqrt{13}$ (the number of points). This gives a maximum error of 8/13 µm, ~1/100th of a pixel.

From the relationship given in figure 8-11, a focal point separation of 18.68 mm corresponds to an increase in line separation of 4.28 µm at the detector. The crystal-detector distance has been measured as 2386.8 ± 0.2 mm and using simple geometry, we obtain a change in angular separation of the lines of –0.37 ± 0.02".

8.6.6 CCD temperature

The CCD pixel size is 40 µm square at +20 °C, but the CCD detectors are operated at –100 °C. Consequently, we need to take into account the thermal contraction of Si when the CCDs are at operating temperature. The coefficient of thermal expansion for Si is 2.5 x 10^{-6} /°C at 0 °C and reduces approximately linearly to 1.0 x 10^{-6} /°C at –100 °C [102]. Taking a value of 1.9 x 10^{-6} /°C (halfway between +20 °C where the pixel size is defined and –100 °C) results in a change in pixel size of ~9 nm, equal to –0.14 pixels over the 622.519 pixels between the µO(5g-4f) and the πN(5g-4f) reflections. Using the crystal-detector distance, this is equivalent to a change in angular separation of –0.49".

8.7 Corrected angle difference

The correction factors defined and calculated in section 8.6 can now be applied to the uncorrected angle difference from section 8.5. The factors are summarised in Table 8-6.

Using the total correction from Table 8-6 and eq. 8-12 we obtain

corrected angle difference = 35'51.12 ± 0.46" . 8-24

Correction factor	μO $\Delta\theta_B$	$\Delta\theta_{B\mu O} - \Delta\theta_{B\pi N}$	πN $\Delta\theta_B$
Crystal temperature	-	-0.03"	-
Crystal bending	8.49"	0.18"	8.31"
Penetration depth	-0.41"	0.01"	-0.42"
De-focussing	-	-0.37 ± 0.02"	-
CCD temperature		-0.49"	
Total correction	-	-0.73"	-

Table 8-6. Summary of correction factors leading to corrected angle difference between πN (5g-4f) and μO (5g-4f) lines.

8.8 Systematic errors

A number of systematic errors also need to be determined and these are described in the following sections.

8.8.1 Curvature correction error

Curvature corrections were determined using both the πN (5g-4f) and the μO (5g-4f) experimental data lines (section 8.4.1) and the average determined. This average was used to provide the actual curvature correction. To determine a possible error introduced, a corrected angular separation was calculated using both individual curvature corrections and the results subtracted, giving a systematic error of

$$\Delta\theta = \pm 0.024".$$ 8-25

8.8.2 Reflection height reduction

At the top and bottom extremes of the reflection on the CCD array, the line profiles begin to broaden (due to the spherical nature of the crystal). The heights of the reflections were trimmed to determine whether this would make any improvement to the curvature correction fit. A number of symmetrical reductions were made, with the corrected line separation calculated each time. The largest difference between line separations (divided by two) was taken to be the systematic error, with a value of

$$\Delta\theta = \pm 0.061".$$ 8-26

8.8.3 Fit region

The centroid of each curvature corrected, reflected line profile is determined statistically (section 8.4.2) which begins by selecting a 'fit region'. The same method to determine the error was used as for the reflection height reduction described in section 8.8.2, resulting in an error in the angular separation, of

$$\Delta\theta = \pm 0.004''. \qquad 8\text{-}27$$

8.8.4 CCD array orientation

Ideally, the CCD array should be oriented perpendicular to the direction of the incoming X-ray path from the crystal. However, mechanical tolerances from the spectrometer tubes, the cryostat flange and the CCD cold-finger all introduce a deviation from this ideal. If the offset angle of the CCD array is measured, the error can be represented as an apparent change in angular separation, as given by

$$\Delta\theta = \arctan\left[\frac{l(1-\cos\alpha)}{Y_{CD}}\right], \qquad 8\text{-}28$$

where l is the measured separation of the reflections, α is the measured offset angle of the CCD array and Y_{CD} is the crystal-detector distance. The offset angle was measured and determined to be < 0.5°. With Y_{CD} = 2386.8 mm, we get an angle change of

$$\Delta\theta = \pm 0.08'' \text{ maximum.} \qquad 8\text{-}29$$

8.8.5 Angular encoder error

The crystal is mounted on a high precision angular encoder but since the πN and μO (5-4) lines are measured simultaneously any error in the angular encoder position is discounted.

8.8.6 Target window structure

It is possible for the honeycomb support structure of the target cell to distort the line shape by selectively blocking part of the reflection. However, the arm angle was optimised (see section 7.7.2) to ensure that the no vertical part of the honeycomb was located in the path of the reflected X-rays.

8.8.7 CCD column separation error

The statistical errors associated with correcting relative CCD positions and rotations are given in section 8.2.1. Each column of CCDs is covered by a single straight line from the mask that makes alignment simple and accurate to the statistical error of the line fit. The column separation, which is more important since it contributes directly to the angular separation of the pionic and muonic lines, is dependent upon difference between the fits to both columns. The error on this distance is taken to be the maximum horizontal offset error between CCD3 and the CCDs in the adjacent column. This is to CCD4 and is ± 0.046 pixels or

$$\Delta\theta_B = \pm 0.16''. \qquad 8\text{-}30$$

8.9 Total systematic error

The total systematic error is summarised in Table 8-7.

Systematic error	Δθ
Curvature correction	± 0.024"
Reflection height	± 0.061"
Fit region	± 0.004"
Response function model	± 0.0"
CCD orientation	± 0.08"
CCD column separation	± 0.16"
Total systematic error	± 0.191"

Table 8-7. Summary of systematic errors of angle difference between πN (5g-4f) and μO ($5g_{9/2}$-$4f_{7/2}$) lines.

The total error given is the sum in quadrature of all systematic errors.

8.10 Final measured πN (5g-4f) transition Bragg angle

If we now combine the corrected angle difference from section 8.5 with the known μO ($5g_{9/2}$-$4f_{7/2}$) Bragg angle (from table 7-1) and the errors from section 8.9 (including the de-focusing error from section 8.6.5), we get

$$\theta_{Bexp}\pi N(5g\text{-}4f) = 52°45'45.77'' \pm 0.46'' \pm 0.191'' \qquad 8\text{-}31$$

for the experimentally measured Bragg angle of the πN (5g-4f) transition, where the format is *Bragg angle ± statistical error ± systematic error.*

8.11 Pion mass value

The experimentally measured Bragg angle presented in the previous section can be expressed as

$$\theta_{Bexp} = \theta_B + \Delta\theta_{ind}, \qquad 8\text{-}32$$

where θ_B is the Bragg angle in vacuum and $\Delta\theta_{ind}$ is the change in Bragg angle due to refraction (see section 3.2). Therefore, using the modified Bragg Law (eq. 3-9) we can get the wavelength corresponding to the experimentally measured Bragg angle. The crystal is silicon, cut along the (110) plane. The reflection from this plane is destructive and the pionic and muonic transitions are actually reflected in 2nd order from the (220) plane. The crystal d spacing for the (220) plane is known to better than 30 ppb [107]. The index of refraction for silicon is less well known (of order 5%) and is energy dependent, but using the μO (5g-4f) line as calibration means that only the difference in refractive index is relevant. $\Delta\theta_{ind}$ was calculated using XOP2 for both the μO ($5g_{9/2}$-$4f_{7/2}$) and the πN (5g-4f) lines (the πN (5g-4f) was determined using the current pion mass value) and are given below

$$\Delta\theta_{ind}\ \mu O(5g_{9/2}\text{-}4f_{7/2}) = 13.22'' \qquad 8\text{-}33a$$

$$\Delta\theta_{ind}\ \pi N(5g\text{-}4f) = 12.94''. \qquad 8\text{-}33b$$

The difference is 0.28", equivalent to a ~1 ppm correction, but with a maximum possible error of 5% it has no impact on the final result. Using $\Delta\theta_{ind}$ from eq. 8-33b and θ_{Bexp} from eq. 8-32, we get a vacuum Bragg angle for the πN(5g-4f) transition of

$$\theta_B\ \pi N(5g\text{-}4f) = \theta_{Bexp} - \Delta\theta_{ind} = 52°45'32.83''. \qquad 8\text{-}34$$

We can now use the standard Bragg equation (eq. 3-1) to determine the wavelength of the πN (5g-4f) transition from the vacuum Bragg angle. Substituting for lattice spacing, d_{220} = 192015.569 ± 0.006 fm and Bragg angle from eq. 8-34, we get a value of

$$\lambda\ \pi N\ (5g\text{-}4f) = 3.057265\ \text{Å}. \qquad 8\text{-}35$$

Using the energy-wavelength relationship, $E = hc/\lambda$, the experimental transition energy is obtained as (converting energy to eV)

$$E\ \pi N\ (5g\text{-}4f) = 4055.42821\ \text{eV}\ . \qquad 8\text{-}36$$

The constants within this relationship are defined to much higher levels of precision than required by the experimental data.

In order to obtain the pion mass value from the energy of the πN (5g-4f) transition, QED calculations have been performed [108] to determine the relationship between the mass and energy, in the region of the pion mass value. The calculated values are plotted in figure 8-12.

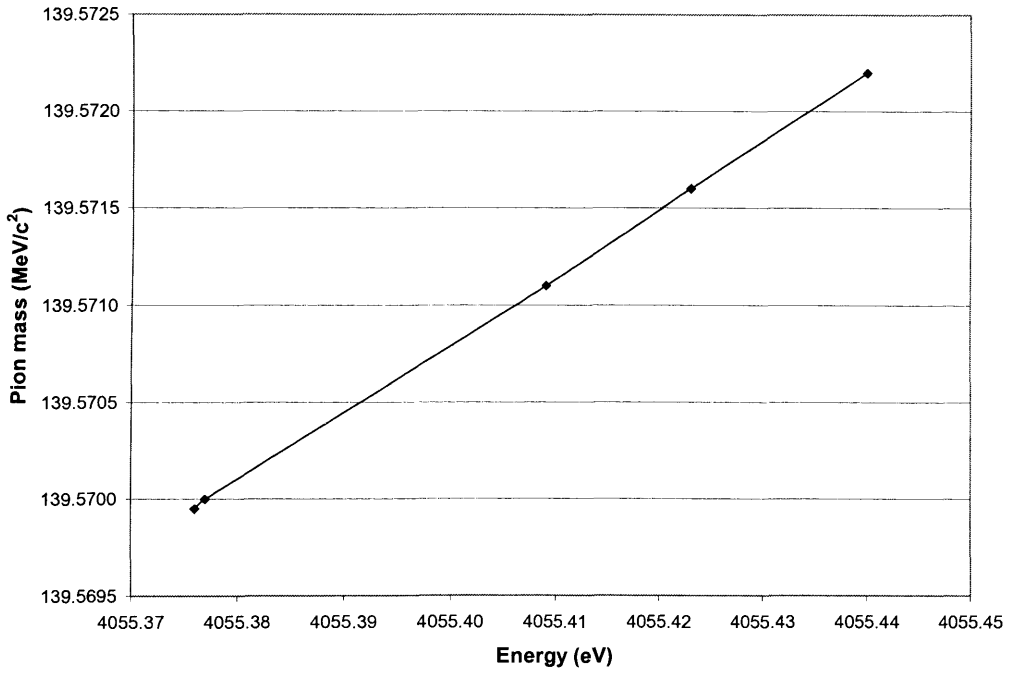

Figure 8-12. Plot of pion mass against πN (5g-4f) transition energy. The data points have been fitted with the straight line shown in the diagram.

Over the small range of energy/mass values given here, the relationship is linear and has been fitted with the following relationship,

$$m_{\pi^-} = 0.03475592362E_{\pi^-} - 1.378395493\ \text{MeV/c}^2\ . \qquad 8\text{-}37$$

Substituting for E_{π^-} from eq. 8-36, we obtain a value for the negatively charged pion mass of

$$m_{\pi^-} = 139.57176 \pm 0.000239 \pm 0.000099 \text{ MeV/c}^2 , \qquad 8\text{-}38$$

where the errors are statistical and systematic respectively. If we combine these errors quadratically we get a total error of 1.85 ppm. This result is compared with previous values and the current Particle Data Group (PDG) figure (139.57018 ± 0.00035 MeV/c^2, 2.5 ppm) for the charged pion mass, in figure 8-13.

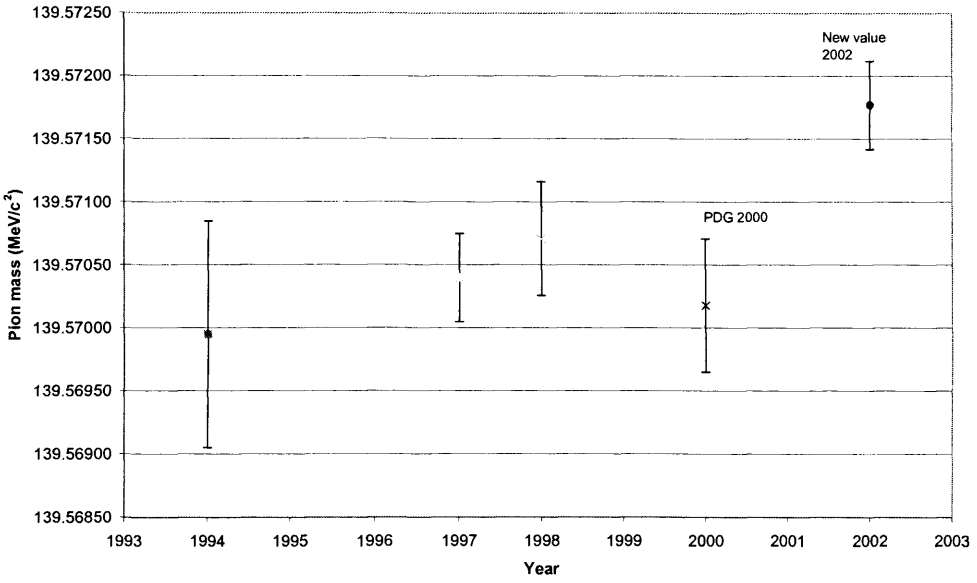

Figure 8-15. Comparison of new value for the charged pion mass with the PDG world average figure (2000) and previous values.

Although the precision of the new value is good, there is concern over the accuracy since the new value is 11.3 ppm larger than the PDG value.

8.12 Muon neutrino mass upper limit

The charged pion mass we have from eq. 8-38, the muon mass and muon momentum are given in eqs. 6-32b and 6-32c respectively. Substituting these values into eq. 6-30, and their uncertainties into eq. 6-31, we obtain a value for the muon-neutrino mass upper limit of

$$m_{\nu\mu} < \quad 0.33 \text{ MeV/c}^2 , 90\% \text{ confidence level} . \qquad 8\text{-}39$$

This value does not constrain the muon-neutrino mass to the same level as the previous pion mass value, due to the fact the new pion mass value is ~11 ppm larger than the current world average.

9 Conclusions and further work

The PDG value for the charged pion mass is 139.57018 ± 0.00035 MeV/c^2, a precision of 2.5 ppm. This number is essentially the average of two previous measurements, Lenz 98 and Jeckelmann 94. The Lenz value (139.57071 ± 0.00053 MeV/c^2) resulted from the feasibility study for the experiment presented in this thesis. It used the 5g-4f transition from pionic nitrogen (gas target) but with a copper fluorescence calibration line and a single column of two CCD detectors. This result has good agreement with the Jeckelmann measurement (139.56995 ± 0.00035 MeV/c^2) obtained in a different way, measuring the 4f-3d transition of pionic magnesium from a solid target, with a NaI/CsI detector. The new pion mass value (139.57150 ± 0.000259 MeV/c^2) has a precision of 1.85 ppm, better than that of the world average. However, the new value is 9.5 ppm higher and consequently the error bars do not overlap. Studying recent results from other pion mass measurements (figure 8-15) does not indicate that such an increase should be expected. The fact that the Lenz value is in good agreement with previous experiments indicates, as the feasibility study attempted to show, that the physical method presented here is valid.

The analysis presented in chapter 8 has been studied closely in an attempt to identify a possible source of the discrepancy. Basic arithmetic error has been eliminated by three different members of the collaboration following the analytical process. 9.5 ppm is equivalent to 0.73 pixels (~2.5") at the detector and so the measured line separation would have to be about 29 μm too large to compensate for this difference fully. In calculating the separation of the lines, several correction factors are taken into account. These factors are dominated by the de-focusing correction (-0.37") and the CCD temperature correction (-0.49") both of which are required due to the use of the new large area CCD detector, which is the main difference between the new experiment and the Lenz study. The focus position on the Rowland circle was verified at the end of the beam run experimentally by measuring the response profile of the πNe (6h-5g) transition. The CCD array was found to be ~5 mm inside the true focus. However, as demonstrated in section 8.6.5, the change in line separation is dependent only upon the distance between the focal points and not on the relative position to the Rowland circle. This relationship holds for at least 8 mm either side of the focus on the Rowland circle and is not considered to be the source of the discrepancy. The CCD operating temperature of –100 °C raises a number of issues related to thermal contraction. The calibration and experimental lines are measured simultaneously the lines are separated by more than 24 mm of silicon (~622 pixels). The six CCDs are mounted on invar substrates, which in turn are supported on a single invar cold finger. Invar was chosen for its low coefficient of thermal expansion (0.9 x10^{-6} /°C) and since the

gap between the CCDs is of order 300 μm it can not contribute a change of the order required. Also, the column separation distance was determined using the mask alignment method at the normal operating temperature and so the effect is cancelled. Of more interest is the change in pixel size with temperature due to the coefficient of thermal expansion of silicon. This has already been taken into account in the analysis and even allowing for coefficient variations with temperature it can not contribute more than a 2 ppm correction. However, this correction, along with conversion from pixels to angular separation of the lines, depends upon the original pixel size at room temperature. The nominal pixel size as quoted by the CCD manufacturer is 40 μm square. No uncertainty on this figure is given and a reduction in pixel size of just 26 nm would provide one sigma correlation between the new determination of the charged pion mass and the world average value. Consequently, accurate determination of the CCD pixel dimension is a priority and methods to measure this are being considered. In parallel with this the CCD cryostat support has been re-designed to avoid alignment problems when the arm angle is changed, as seen in the X-ray dispersion measurements. A new dispersion measurement using copper fluorescence X-rays has been performed and analysis of this data should yield a dispersion relationship which is independent of pixel size.

Experimental data from the Super Kamiokande [109] and Sudbury Neutrino [110] observatories suggest mass values for the muon neutrino (indeed for all flavours of neutrino) of a few eV at most, far below the upper limit determined as part of this thesis. However, these results are only qualitative and the method described here still provides the most accurate quantitative measurement of the muon neutrino mass upper limit. The new value for the upper limit presented in this thesis is influenced by the relatively large increase of the new pion mass value over previous values. The new upper limit derived is larger than that already obtained and consequently offers no new information at present. This may well change once concerns over the pion mass value have been resolved.

Looking beyond the possible unresolved correction factor, the experimental apparatus and method described in this thesis has produced a new value for the charged pion mass with a precision better than that of any previous experiment. Although the target precision of 1 ppm was not reached, the new result is dominated by the statistical uncertainty. It would be quite possible to reach the 1 ppm level by taking data for approximately 50% longer than for this experiment.

The new pion mass value presented at the end of chapter 8 is the culmination of a period of experiment derivation and design, apparatus development, experimental operation and data and error analysis. Whilst the pion mass derivation and subsequent upper limit of the muon neutrino mass are valid pursuits in their own right, techniques learned (both practical and analytical) during the course of this work have application beyond this goal. A new experiment, to investigate the strong interaction shift and width of pionic hydrogen in the ground state, is already underway using the same experimental apparatus and will benefit directly from work presented here.

Appendix A

A.1 Correction of Bragg equation due to refraction

Inside the crystal (figure 3-2) we have

$$n\lambda' = 2d \sin\theta_B' \qquad \text{A1-1}$$

and the index of refraction is defined as

$$\mu = 1 - \delta = \frac{\lambda}{\lambda'} = \frac{\cos\theta_B}{\cos\theta_B'} \ . \qquad \text{A1-2}$$

From eqs. A1-1 and A1-2 we get

$$\mu = \frac{n\lambda}{2d \sin\theta_B'} \ . \qquad \text{A1-3}$$

Since

$$\cos^2\theta + \sin^2\theta = 1 \qquad \text{A1-4}$$

and from eq. A1-2

$$\cos\theta_B' = \frac{\cos\theta_B}{\mu} \ , \qquad \text{A1-5}$$

we can write

$$\sin\theta_B' = \left(1 - \frac{\cos^2\theta_B}{\mu^2}\right)^{\frac{1}{2}} \ . \qquad \text{A1-6}$$

Substituting eq. A1-6 into eq. A1-3, we get

$$\mu = \frac{n\lambda}{2d\left(1-\frac{\cos^2\theta_B}{\mu^2}\right)^{\frac{1}{2}}}, \qquad \text{A1-7}$$

or

$$n\lambda = 2d\mu\left(1-\frac{\cos^2\theta_B}{\mu^2}\right)^{\frac{1}{2}}. \qquad \text{A1-8}$$

Taking μ inside the bracket and replacing $cos^2\theta_B$ with $1\text{-}sin^2\theta_B$ gives

$$n\lambda = 2d\left(\mu^2 - 1 + \sin^2\theta_B\right)^{\frac{1}{2}} \qquad \text{A1-9}$$

and taking $sin\theta_B$ outside the bracket, we obtain

$$n\lambda = 2d\sin\theta_B\left(1+\frac{\mu^2-1}{\sin^2\theta_B}\right)^{\frac{1}{2}}. \qquad \text{A1-10}$$

Substituting for μ from eq. A2-2 gives

$$n\lambda = 2d\sin\theta_B\left(1-\frac{2\delta-\delta^2}{\sin^2\theta_B}\right)^{\frac{1}{2}}. \qquad \text{A1-11}$$

Since δ is of order 10^{-6}

$$n\lambda \approx 2d\sin\theta_B\left(1-\frac{2\delta}{\sin^2\theta_B}\right)^{\frac{1}{2}}. \qquad \text{A1-12}$$

Expanding the bracket and ignoring powers of δ higher than 1, we get

$$n\lambda = 2d \sin\theta_B \left(1 - \frac{\delta}{\sin^2 \theta_B}\right) \qquad \text{A1-13}$$

for the Bragg Law modified due to refraction.

A2 CCD alignment using optical measuring machine

The optical measuring machine (Messtechnik Horizontal-Mess-Projector ST360H) was configured with a x50 lens. The CCD camera was removed from the cryostat without disturbing the detector array and installed on the measuring machine table. The CCD array was aligned parallel to the axis of the measuring machine in both the vertical and horizontal directions by verifying the focus at the extremes of the array. Each CCD has two pre-defined reference marks that are part of the metalisation of the CCD itself (figure A2-1).

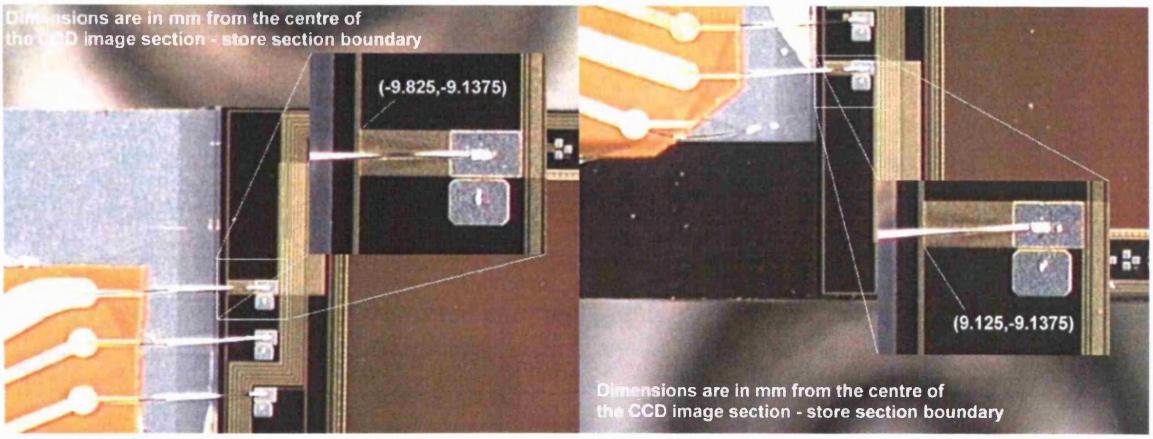

Figure A2-1. Location and identification of CCD position measurement reference points. The distances are in mm, from the centre of the image section/store section boundary.

Each reference point on the CCD array was given a number, starting at CCD4. The layout of these reference numbers is shown in figure A2-2.

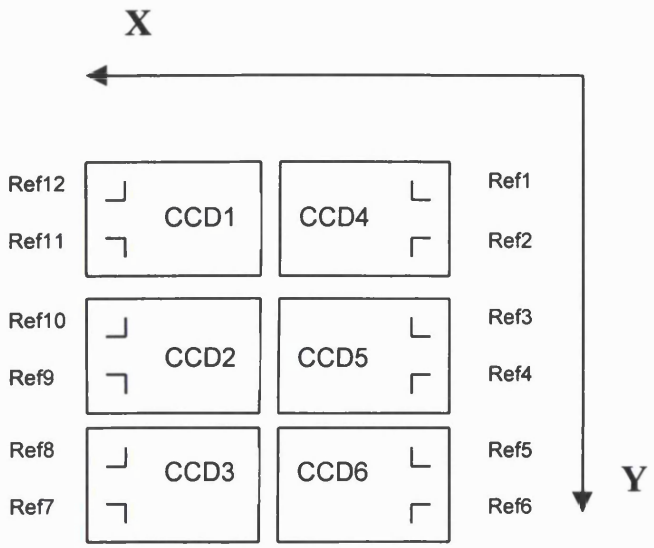

Figure A2-2. Layout of reference marks on CCD array. Array is viewed from the front.

The measurement axis of the measuring machine was aligned approximately with CCD4, with the X and Y axes as shown in figure A2-2. The origin was set to Ref1 by taking two measurement points on the each of the horizontal and vertical lines of the reference mark. The measuring machine is operated manually. The operator moves the translation table (and hence the CCD array) to align the cross-hairs with the point to be measured. This point is then recorded in mm, to 3 decimal places (i.e. to the 1 μm level). Since the machine does not calculate distances but only measures positions, Ref1, although defined as the origin, was treated as another point to be measured. The measured position of Ref1 was taken as the origin from which the distances to all other measured reference points were calculated.

Twenty position measurements of Ref1 and Ref2 were taken initially to determine the error on a single measurement, and also to determine the number of repeat measurements necessary to achieve a sub-micron error on the averaged position of each reference point. The average and standard deviation of the first twenty measurements are shown in Table A2-1.

	X-Coord		Y-Coord	
Reference	**Average**	**StdDev**	**Average**	**StdDev**
Ref1	0.0001	0.0012	-0.0005	0.001
Ref2	-0.0007	0.0016	18.9526	0.0014

Table A2-1. Average and standard deviation of twenty measurements of Ref1 and Ref2 positions (on CCD4). All dimensions are in mm.

From these figures we can see that the rms error is <1.5 μm on a single measurement. With twenty independent measurements of each reference point, a typical error of $1.5/\sqrt{20} = 0.34$ μm is possible. These measurements were taken by simply moving to each CCD in turn and taking repeat measurements between the pair of reference points. The complete results are summarised in Table A2-2. All distances are calculated from the averaged measurement of Ref1.

CCD	Reference Point	X-difference (mm)	error (mm)	Y-difference (mm)	error (mm)
4	1	0	0	0	0
4	2	-0.0008	0.00045	18.9531	0.00038
5	3	-0.0595	0.00056	24.8495	0.00029
5	4	-0.0672	0.00056	43.8009	0.00048
6	5	-0.1241	0.00063	49.7056	0.00034
6	6	-0.1187	0.00056	68.6589	0.00028
3	7	66.8747	0.00052	68.0288	0.00036
3	8	66.9951	0.0006	49.0754	0.00034
2	9	66.8166	0.00055	43.1199	0.00035
2	10	66.8644	0.00079	24.1679	0.00034
1	11	66.8188	0.00059	18.3467	0.00039
1	12	66.8488	0.00055	-0.6057	0.00032

Table A2-2. Summary of position measurements of reference points on all CCDs. The origin for all measurements is the averaged position of Ref1 on CCD4.

The error on each position measurement is the standard deviation of the twenty measurements at that point divided by $\sqrt{20}$ (not shown in the table). The errors in Table A2-2 are then calculated as the square-root of the quadratic sum of the error on the relevant position measurement summed with the error on the measurement of Ref1.

The distance between each pair of Reference points has also been calculated, as a measurement check, since this distance is known from CCD manufacture to be 18.950 ± 0.001 mm. The calculated separations are listed in Table A2-3.

CCD	Ref points	Separation (mm)	Error (mm)
4	2-1	18.9531	0.00038
5	4-3	18.9514	0.000561
6	6-5	18.9533	0.00044
3	7-8	18.9534	0.000495
2	9-10	18.9520	0.000488
1	11-12	18.9524	0.000504

Table A2-3. Calculated distances between Reference points on each CCD.

From these results, we can see that the statistical precision of the measurements is very good, with errors of typically 0.5 μm. However, there appears to be a systematic error of order 1 to 2 μm when we compare the measured value with that quoted by the CCD manufacturer. Until this discrepancy is resolved, this alignment measurement has been disregarded.

References

[1] Johnson, T.H., Pomerantz, M.A., Phys. Rev. **55**, 104, 1939.

[2] Tomonaga, S., Araki, G., Phys. Rev. **58**, 90, 1940.

[3] Conversi, M., Pancini, E., Piccioni, O., Phys.Rev. **71**, 209, 1947.

[4] Fermi, E., Teller, E., Weisskopf, V., Phys. Rev. **71**, 314, 1947.

[5] Fermi, E., Teller, E., Phys. Rev. **72**, 399, 1947.

[6] Horváth, D., Lambrecht, R.M., "Exotic atoms – a bibliography 1939-1982", Elsevier, 1984.

[7] Simons, L.M., Horváth, D. and Torelli, G., "Electromagnetic cascade and chemistry of exotic atoms", Plenum Press, 1990.

[8] Horváth, D., Nucl. Instr. Meth. **B87**, 273, 1994.

[9] Vogel, P., Haff, P.K., Akylas, V., Winther, A., Nucl. Phys. **A254**, 445, 1975.

[10] Akylas, V., Vogel, P., Comp. Phy. Comm. **15**, 291, 1978.

[11] Bacher, R. et al, Phys. Rev. Lett. **54**, 2087, 1985.

[12] Bacher, R. et al, Phys. Rev. **A39**, 1610, 1989.

[13] Taqqu, D. et al, Hyperfine Interactions **119**, 311, 199.

[14] Ruckstuhl, W. et al, Nucl. Phys. **A430**, 685, 1984.

[15] Indelicato, P., Simons, L., AIP Con. Proc. **564**, 2000.

[16] Pohl, R. et al, "The Hydrogen Atom: Precision physics of simple atomic systems", Springer, 454, 2000.

[17] Gabrielse, G. et al, Phys. Rev. Lett. **65**, 1317, 1990.

[18] PSI exp. R-98.01; http://pihydrogen.web.psi.ch.

[19] Ito, T.M. et al, Phys. Rev. **C58**, 2366, 1998.

[20] Bearden, J.A., Rev. Mod. Phys. **39**, 78, 1967.

[21] Von Laue, M., Ann. der Physik. **41**, 971, 1913.

[22] Bragg, W.L., Proc. Camb. Phil. Soc. **17**, 43, 1912.

[23] Dunn, J., High resolution X-ray spectroscopy of laboratory sources, Ph.D. thesis, University of Leicester, 1990.

[24] Compton, A.H., Allison, S.K., X-rays is theory and experiment, 2nd Ed., 672, 1960.

[25] Agarwal, B.K., I.S., X-ray spectroscopy, 1st Ed., 134, 1979.

[26] Brennan, S., Cowan, P.L., Rev. Sci. Instr. **63**, 850, 1992.

[27] Johann, H.H., Z. Phys. **69**, 185, 1931.

[28] Von Hamos, L., Ann. der Physik **17**, 716, 1933.

[29] Eggs, J., Ulmer, K., Zeit. f. Phys. **20**, 118, 1965.

[30] Cembali, F., Fabbri, R., Servidori, M., Zani, A., Basile, G., Cavagnero, G., Bergamin, A. Zosi, G., J. Appl. Cryst. **25**, 424, 1992.

[31] Johansson, T., Zeit. f. Phys. **82**, 507, 1933.

[32] Boyle,W., Smith, G., Bell Sys. Tech. J. **49**, 587, 1970.

[33] Fraser, G.W., X-ray detectors in astronomy, Cambridge University Press, 1st Ed., 208, 1989.

[34] McLean, I.S., Electronic and computer-aided astronomy, 1st Ed., 81, 1989.

[35] Gordon, E.I., IEEE Trans. Nucl. Sci. **NS-19**, 190 , 1972.

[36] Catura, R.C., Smithson, R.C., Rev. Sci. Instrum. **50**, 219 , 1970.

[37] Lumb, D.H., Hopkinson, G.R., Wells, A.A., Nucl. Inst. Meth. Phys. Res. **221**, 130, 1984.

[38] Lumb, D.H., X-ray imaging and spectroscopy with CCDs, Ph.D. thesis, University of Leicester, 1983.

[39] Chowanietz, E.G., Advances in CCDs for X-ray imaging and spectroscopy, Ph.D. thesis, University of Leicester, 1986.

[40] Holland, A.D., Radiation effects in CCD X-ray detectors, Ph.D. thesis, University of Leicester, 1990.

[41] Castelli, C.M., The soft X-ray performance of CCD detectors, Ph.D. thesis, University of Leicester, 1991.

[42] Keay, A., An investigation of fine structure effects in CCDs developed for JET-X, Ph.D. thesis, University of Leicester, 1997.

[43] Wells, A.A. et al, Proc. IAU Coll. **115**, 318, 1990.

[44] Lumb, D.H., Eggel, H., Laine, R., Peacock, A., Proc. SPIE **2808**, 326, 1996.

[45] Fano, U., Phys. Rev. **72**, 26, 1947.

[46] Lumb, D.H., Holland, A.D., IEEE Trans. Nucl. Sci. **NS-35**, 534, 1988.

[47] Bertolini, G., Coche, A., Semiconductor devices, Elsevier-North Holland Amsterdam, 1968.

[48] Fraser, G.W., Abbey, A.F., Holland, A., McCarthy, K., Owens, A., Wells, A., Nucl. Inst. Meth. **A350**, 365, 1994.

[49] Owens, A., Fraser, G.W., Abbey, A.F., Holland, A., McCarthy, K.J., Keay, A., Wells, A., Nucl. Inst. Meth. **A382**, 503, 1996.

[50] Grove, A.S., Physics and technology of semiconductor devices, Wiley, 1967.

[51] Holland, A.D., Ph.D. thesis Leicester University, 40, 1990.

[52] McCarthy, K.J., Owens, A., Holland, A.D., Wells, A., Nucl. Inst. Meth. **A346**, 353, 1994.

[53] Holland, A.D., Turner, M.J.L., Abbey, A.F., Pool, P., Proc. SPIE **2808**, 414, 1996.

[54] Holland, A.D., Radiation effects in CCD X-ray detectors, Ph.D. thesis, University of Leicester, 1990.

[55] Chowanietz, E.G., Advances in CCDs for X-ray imaging and spectroscopy, Ph.D. thesis, University of Leicester, 1986.

[56] CCD Imaging III, EEV, 1987.

[57] EEV CCD 05-30 Datasheet, 1997.

[58] Hopkinson, G.R., Lumb, D.H., J. Phys. E. Sci. Inst. **15**, 1214, 1982.

[59] Kansy, R., IEEE J. Solid-State Circuits **SC-15**, 373, 1980.

[60] Yukawa, H., Proc. Phys. Math. Soc., Japan, **17**, 48, 1935.

[61] Hagiwara, K., Physical Review **D66**, 010001, 2002.

[62] Arya, A.P., Fundamentals of Nuclear Physics, Allyn and Bacon, 465, 1966.

[63] Neddermeyer, S.H., Anderson, C.D., Phys. Rev. **51**, 1005, 1937.

[64] Conversi M., Pancini E., Piccioni O., Phys. Rev. **68**, 232, 1945.

[65] Lattes, C.M.G., Occhialini, G.P.S., Powell, C.F., Nature **163**, 47, 1949.

[66] Gardner, E., Lattes, C.M.G., Science **107**, 270, 1948.

[67] Blin-Stoyle, R.J., Nuclear and Particle Physics, Chapman & Hall, 1st Ed., 69, 1991.

[68] Smith, W.H. et al, Phys. Rev. **78**, 86, 1950.

[69] Barkas, W.H., Am. J. Phys. **20**, 8, 1952.

[70] Fermi, E., Teller, E., Phys. Rev. **72**, 399, 1947.

[71] Stearns, M., DeBenedetti, S., Stearns, M., Leipuner, L., Phys. Rev. **93**, 1123, 1954.

[72] Stearns, M., Stearns, M.B., DeBenedetti, S., Leipuner, L., Phys. Rev. **95**, 1353, 1954.

[73] Shafer, R.E., Phys. Rev. **163**, 1451, 1967.

[74] Booth, P.S.L. et al, Phys. Lett. B **32**, 723, 1970.

[75] Marushenko, V.N.et al, JETP Lett. **23**, 72, 1976.

[76] Carter, A.L. et al, Phys. Rev. Lett. **37**, 1380, 1976.

[77] Lu, D.C., et al, Phys. Rev. Lett. **45**, 1066, 1980.

[78] Jeckelmann, B. et al, Nucl. Phys. **A457**, 709, 1986.

[79] Jeckelmann, B., Goudsmit, P.F.A., Leisi, H.J., Phys. Lett. **B335**, 326, 1994.

[80] Caso, C. et al, The European Physical Journal **C3**, 1998.

[81] Anagnastopoulos, D. et al, Nucl. Phys. **A626**, 375, 1997.

[82] Lenz, S. et al, Phy. Lett. **B416**, 50, 1998.

[83] Barkas, W.H., Birnbaum, W., Smith, F.M., Phys. Rev. **101**, 778, 1956.

[84] Bardon, M. et al, Phys. Rev. Lett. **14**, 449, 1965.

[85] Booth, P.S.L., Johnson, R.G., Williams, E.G.H., Wormald, J.R., Phys. Lett. **B26**, 39, 1967.

[86] Daum, M. et al, Phys. Rev. **D20**, 2692, 1979.

[87] Daum, M. et al, Phys. Lett. **B265**, 425, 1991.

[88] Assamagan, K. et al, Phys. Lett. **B335**, 231, 1994.

[89] Assamagan, K. et al, Phys. Rev. **D53**, 6065, 1996.

[90] Rosser, W.G.V., Introductory Special Relativity, Taylor & Francis, 1st Ed., 143, 1991.

[91] Jeckelmann, B. et al, Nucl. Phys. **A457**, 709, 1986.

[92] Jeckelmann, B., Goudsmit, P.F.A., Leisi, H.J., Phys. Lett. **B335**, 326, 1994.

[93] Härtwig, J. et al, J. Appl. Cryst. **26**, 539, 1993.

[94] Groom, D.E. et al, (PDG): The European Physical Journal **C15**, 1, 2000.

[95] Akylas, V.R., Vogel, P., Comp. Phys. Comm. **15**, 291, 1978.

[96] Siems, T. et al, Phys. Rev. Lett. **84,** 4573, 2000.

[97] Simons, L.M., Physica Scripta **T22**, 90, 1988.

[98] Simons, L.M., Hyperfine Interactions **81**, 253, 1993.

[99] Indelicato, P. – private communication, 2000.

[100] Hennebach, M., Internal report. 2001.

[101] Lenz, S. et al, Phys. Lett. **B416**, 50, 1998.

[102] Okada, J., J. App. Phys., **56**, 314, 1984.

[103] Eggs, J., Ulmer, K., Zeit f Phys **20**, 118, 1965.

[104] XOP2 – www.esrf.fr/computing/scientific/xop/

[105] Cembali, F., Fabbri, R., Servidori, M., Zani, A., Basile, G., Cavagnero, G., Bergamin, A. Zosi, G., J. Appl. Cryst. **25** (1992) 424.

[106] Anagnostpoulos, D.F., private communication, 2002.

[107] Basile, G. et al, Phys. Rev. Lett. **72** (1994) 3133.

[108] QED calculations for pion mass/energy.

[109] The Super-Kamiokande Collaboration, Phys. Rev. Lett. **81**, 1562, 1998.

[110] The SNO Collaboration, Phys. Rev. Lett. **87**, 071301 , 2001.